Near-Field to Far-Field Transformation and Fault Detection Using Adaptive Sampling and Machine Learning in Source Reconstruction Method

by

Rezvan Rafiee Alavi

A thesis submitted in partial fulfillment of the requirements for the degree of

Doctor of Philosophy

in

ENGINEERING MANAGEMENT

Department of Mechanical Engineering

University of Alberta

Abstract

Until not so long ago, near-field and far-field measurement techniques were the two prominent approaches to evaluating antennas. A direct far-field measurement can be conducted in outdoor or indoor environments. The measurement of small antennas can be performed in anechoic chambers. For large antennas, however, a remote open-air-test-site which consists of a large domain in a rural area is required to stay away from reflections [1]. In near-field techniques, antenna emissions are measured in the radiating near-field region. The near-field data are then projected to the far-field using well-established and trustworthy algorithms. Recently, these methods have been used widely since they allow the accurate measurement of antennas in a controlled environment [2]- [10]. The assessment of antenna design using the aforementioned techniques is expensive and time-consuming for antenna designers and wireless engineers, especially those who want to do fast-prototyping and investigate the effect of different parameters in their design.

Time-to-market and project costs are two fundamental considerations which have an indisputable effect on Printed circuit board (PCB) and antenna designers' success in developing their products. The near-field data give RF (Radio Frequency) and antenna engineers a unique insight into the main problems which cause design failure. A fast high resolution electromagnetic compatibility (EMC) and electromagnetic interference (EMI) testing enable PCB designers to detect and root out unintended emissions and get the approval for compliance tests in real-time. The purpose of this study is to increase the accuracy of

the near-field-to-far-field-transformation (NFFF) and fault detection algorithms and current-reconstruction methods while keeping the speed of the proposed technique suitable for real time applications.

The near-field measurements are performed using RFX2 that is a bench-top very-near-field measurement tool. RFX2 is a planar array of electronic probes which measure the magnetic field in two orthogonal directions. Then the data are projected into the far-field using plane wave spectrum (PWS) transformation. The developed algorithms result in better accuracy and speed for RFX2 and can be applied to other near-field measurement systems as well.

Preface

This is an original work by Rezvan Rafiee Alavi. Chapter 3 of this thesis is published as, R. Rafiee Alavi, A. Kiaee, R. Mirzavand, and P. Mousavi, "RWG MoM-via-locally corrected Nyström method in near-field to far-field transformation using very-near-field measurement," IET Microwaves, Antennas Propag., vol. 12, no. 2, pp. 145–153, 2018. Chapter 4 is under review as, Rezvan Rafiee Alavi, Rashid Mirzavand, Ali Kiaee, Ruska Patton and Pedram Mousavi, " Detection of the Defective Vias in SIW Circuits from Single/Array Probe(s) Data Using Source Reconstruction Method and Machine Learning", IEEE Trans. Microw. Theory Tech. Jan. 2019. Chapter 5 is under review as, Rezvan Rafiee Alavi, Rashid Mirzavand, Ali Kiaee and Pedram Mousavi,"Accuracy and Time Enhancement of Near-Field Antenna Measurement Considering Noise, Using an Adaptive Data Acquisition and Interpolation Technique", IEEE Trans. Antennas Propag. Nov. 2018.

Acknowledgment

Firstly, I would like to express my sincere gratitude to my advisor Prof. Pedram Mousavi for the continuous support of my Ph.D . study and related research, for his patience, motivation, knowledge and experience. His directions have assisted me throughout my Ph.D program.
Besides, I would like to thank the rest of my thesis committee: Prof. Vien Van and Prof. Robert Fedosejevs for their insightful comments, encouragement, and their invaluable questions which incented me to widen my research from various perspectives.
My sincere thank also goes to Dr. Rashid Mirzavand who provided me with great comments, suggestions, ideas, and revisions.
I thank my colleagues at IWT lab, my friends, and family for their collaborations and support.

Nomenclautures

A	The area of each triangle patch
$A_{k'_i}$	$(i = 1, 2)$ The area of each of two triangles sharing the $k'th$ interior edge
$\vec{a}_1^n, \vec{a}_2^n$	The unitary vectors of LCN method
A_x	x component of plane wave spectrum
A_y	y component of plane wave spectrum
A_z	z component of plane wave spectrum
$\vec{A}(k_x, k_y)$	plane wave spectrum
AOI	**A**utomated **O**ptical **I**nspection
AUC	**A**rea **U**nder **C**urve
AUT	**A**ntenna **U**nder **T**est
$[b]$	Unknown coefficients matrix in the RWG method
$b_{k'}^p$	The coefficient of the ramp functions in RWG method
BF	**B**asis **F**unction
c_n^j	Unknown coefficient of electric current
c_n^M	Unknown coefficient of magnetic current
CPW	**C**o**P**lanar **W**aveguide
D	The dimension of a rectangular measurement plane
DOF	**D**egree **O**f **F**reedom
dS	Infinitesimal element of surface
DUT	**D**evice **U**nder **T**est
dV	Infinitesimal element of volume
E_+	Electric field just out of source surface
E_-	Electric field on an inward-offset of the source surface
$\vec{E}(r)$	Electric field
E_{int}	the number of edges on the interior edges

E_{ext}	the number of edges on the exterior edges
$EFIE$	**E**lectric **F**ield **I**ntegral **E**quation
EMC	**E**lectromagnetic **C**ompatibility
EMI	**E**lectromagnetic **I**nterference
Err	Error of the RWG-via-LCN impedance matrix
F	the number of flat patch faces
F_n	n-th Basis function
g	Free space Green function
H_+	Magnetic field just out of source surface
H_-	Magnetic field on an inward-offset of the source surface
H^{ref}	The reference magnetic field
$H^{Numerical}$	The magnetic field which is calculated numerically
$HFSS$	HFSS stands for High Frequency Electromagnetic Field Simulation. HFSS is a finite element method solver for electromagnetic structures from Ansys.
$[I_6]$	(6×6) identity matrix
$\vec{J}$	Electric current
$\vec{k}$	Wave vector
k_0	Wave number in free space
k_x	x component of wave vector
k_y	y component of wave vector
k_{xm}	The maximum of k_x
k_{ym}	The maximum of k_y
k_z	z component of wave vector
L	The dimension of a rectangular source plane
$[L]$	The synthesized kernel using locally corrected Nyström method

$l_{k'}$	the length of k'th interior edge that is shared between two adjacent triangles
LCN	**L**ocally **C**orrected **N**yström
$\vec{M}$	Magnetic current
$MFIE$	**M**agnetic **F**ield **I**ntegral **E**quation
$MLFMM$	**M**ultilevel **F**ast **M**ultipole **M**ethod
MoM	**M**ethod of **M**oment
$\hat{n}$	The unitary vector normal to the surface
$N_{E_{int}}$	the number of interior edges in a discretization scheme
N_x	The number of sampling points in x direction (on the measurement plane)
N_y	The number of sampling points in y direction (on the measurement plane)
N_p	The number of patches
N_q	The number of quadrature points inside a triangle
NFC	**N**ear- **F**ield **C**ommunication
$NFFF$	**N**ear- **F**ield to **F**ar- **F**ield
p	p-th patch
PCB	**P**rinted **C**ircuit **B**oard
PWS	**P**lane **W**ave **S**pectrum
q	q-th quadrature point
$\vec{R}^p_{k'}$	Ramp function in RWG method
r_M	The position of the measuring probe
RF	**R**adio **F**requency
ROC	**R**eceiver **O**perating **C**haracteristic
RWG	**R**ao- **W**ilton- **G**lisson
SIW	**S**ubstrate **I**ntegrated **W**aveguide

SRM	**S**ource **R**econstruction **M**ethod
TL	**T**ransmission **L**ine
$U(r_M)$	The measuring probe output
V_{probe}	The volume that encloses the probe
$\vec{W}_{probe}$	Spatial weighting function of the probe
$x(j)$	x component of the quadrature point
$y(j)$	y component of the quadrature point
z_t	The position of the measurement plane in PWS method
$Z^{RWG}_{(i,j)}$	ij-th component of RWG impedance matrix
$Z^{RWG-via-LCN}_{(i,j)}$	ij-th component of RWG-via-LCN impedance matrix
$[Z_{LCN}]$	Impedance matrix of LCN method
$[Z_{RWG}]$	Impedance matrix of RWG method
Δx	Sample spacing in x direction
Δy	Sample spacing in y direction
λ	Wave length
∇	Gradient of a scalar value
$\nabla.$	Divergence of a vector
$\nabla\times$	Curl of a vector
$\sum_R$	Reconstruction (source) surface
$\sum_M$	Measurement surface
η_0	Intrinsic impedance of free space
ω_{qp}	Weight function of a q-point quadrature rule on path p
η, ζ	Barycentric 2-D space components
δ_{ij}	Kronecker-Delta
$\Delta_{\|}$	Surface divergence
$\|\|.\|\|$	Euclidean norm
λ_0	Free space wavelength

List of Figures

Fig1.1 Antenna field regions [24] 3

Fig1.2 Direct far-field antenna measurements [24] 4

Fig1.3 Far-field measurement setup for slant ranges [24] 5

Fig1.4 Antenna measurement using compact ranges [24] 5

Fig1.5 Representation of an antenna using equivalent sources [24] 7

Fig1.6 Measurement of near-field and output signal of the probe at discrete points [24] 8

Fig1.7 Planar near-field measurement setup with limited scan plane dimensions [24] 9

Fig1.8 The influence of probe position relative to the AUT in near-field measurement [24] 9

Fig1.9 Cylindrical near-field measurement. Probe is moving in the vertical direction (step in ϕ) [24] 10

Fig1.10 Valid angle in cylindrical near-field measurements [24] 11

Fig1.11 Spherical near field measurement [24] 11

Fig1.12 Planar near-field measurement [2] 13

Fig1.13 Computer Simulation and exact solution of y component of electric field along z axis for a uniformly circular aperture antenna. The diameter of the antenna is 10λ, and $\Delta x = \Delta y = \lambda/2$ and $N_x = N_y = 64$ [2]. 15

Fig1.14 Computer Simulation and exact solution when the sample spacing in Fig. 1.13 is reduced to $\Delta x = \Delta y = 0.491\lambda$ [2]. 16

Fig1.15 Simulated E_y along x axis with different sample spacings [2]. 16

Fig1.16 Computer Simulation and exact solution with the sample spacing of $\Delta x = \Delta y = 0.2445\lambda$ on 128×128 array [2]. 18
Fig1.17 The effect of inclusion and exclusion of the evanescent content on a parabolically tapered aperture distribution [2] 18

Fig2.1 An illustration of the main steps in LCN to RWG conversion. 28
Fig2.2 Simulation and measurement set ups (a) Simulation setup which includes planar measurement probes, and source plane, (b) RFX2, (c) A simple schematic of RFX2 measurement system, (d) A sample of measuring an antenna with RFX2. 29
Fig2.3 Point-based discretization of the source plane, (a) Uniform discretization of the source plane using triangular flat patches, (b) Ramp functions (half RWG basis functions), (c) Barycentric triangle, (d) Covariant unitary vectors on a flat triangular patch [20] 33
Fig2.4 Conversion from LCN to RWG impedance matrix. From right to left, in the top row, $[\alpha]$ converts LCN basis functions at each quadrature point to ramp functions, and $[R]^T$ translates ramp functions at all points to three main R_1, R_2, and R_3. In the second row, $[l]^T$ converts the $\nabla.R$ from LCN system to $\nabla.R_1$, $\nabla.R_2$, and $\nabla.R_3$ in RWG MoM. $[u]$ finally enforce current continuity between adjacent triangles. 40
Fig2.5 Comparison of 200×200 samples of impedance matrices which obtained from RWG-via-LCN with RWG ones (a) For magnetic, (b) Electric currents. The error corresponds to $Z_{i,j} = |Z_{i,j}^{RWG} - Z_{i,j}^{RWG-via-LCN}|/|Z_{i,j}^{RWG}|$ 42
Fig2.6 TSVD regularization method to solve the inverse problem, (a) L-curve (a log–log plot of $\|x\|_2$versus $\|Ax - b\|_2$) or regularization (dipole antenna), (b) Residual norm versus the number of the singular values, (c) The singular values and Fourier coefficients versus the number of singular values 43

Fig2.7 Far-field pattern of two antennas obtained via different methods: HFSS, RWG-via-LCN, PWS, LCN and RWG, (a) Far-field pattern of an E-plane horn antenna, (b) Fasr-field pattern of an ideal dipole antenna. 44
Fig2.8 Measurement setup and far-field pattern of Slot antenna, (a) Slot antenna on the RFX2, (b) far-field pattern of the slot antenna obtained via different methods: HFSS, RWG-via-LCN, PWS, LCN and RWG. 44

Fig3.1 Flow-chart for the comparison of results obtained by different measurement and simulation scenarios. 51
Fig3.2 An illustration of the source reconstruction method over a box which encloses the SIW structure ($\sum_R$). The tangential components of $\vec{H}$ field are measured on plane ($\sum_M$). 53
Fig3.3 A depiction of the magnetic fields on the measurement plane and the discretization scheme (a) the measured magnetic field on the measurement plane, (b) refined mesh, (c) uniform mesh. 56
Fig3.4 The effect of the (a) scanning resolution, (b) scanning area, and (c) scanning height on the condition number of the matrix A. 62
Fig3.5 The effect of the (a) scanning resolution, (b) scanning area, and (c) scanning height on the correlation coefficient. 63
Fig3.6 The aperture model of the defective vias of the SIW structure in free space, (a) the aperture model of a defective via, (b) a SIW TL with two defective vias, (c) the discretized surface of the defective vias to extract the tangential components of the fields over the area of the apertures from HFSS, and (d) the comparison of the magnitude of magnetic field at 1mm away from the SIW TL calculated using the analytical model and obtained from full wave simulation. 64

Fig3.7 The comparison of E- and H- field patterns of the SIW TL close to the ground plane with a patch antenna (a) a patch antenna that is fed with two coax connector at the location of the defective vias, (b) A SIW TL with two defective vias, (c)the magnitude of the H-field and E-field at the distance of 2mm from the SIW TL, (d) the magnitude of the H-field and E-field at the distance of 2mm from the patch, between the patch and the ground plane. . 65
Fig3.8 The comparison of the magnitude of the magnetic field at the location of the defective vias when the SIW TL is in free space and close to a finite ground plane. 66
Fig3.9 The probe used in the single probe measurement. 68
Fig3.10 Single probe measurement, (a) the schematic of the setup for the single probe measurement, (b) The xyz positioner. 68
Fig3.11 Single probe measurement, (a) the experimental setup for the single probe measurement, (b) The single probe measurement of the SIW structure, (c) the trajectory of the single probe. 69
Fig3.12 The probe array measurement setup,(a) a schematic of the probe array measurement setup, (b) The SIW filter above the probe array. 69
Fig3.13 Schematic view of SIW board movement above the probe array. 70
Fig3.14 Detection of the defective vias in a SIW dual mode filter. 72
Fig3.15 The distance from the board at which two adjacent defective vias can be resolved (at 1.84GHz), (a) a view of the magnetic field amplitude computed using HFSS full wave simulator, (b) the magnetic field amplitude calculated analytically. 73
Fig3.16 Subtraction of the radiation from the transitions and feed lines from the total near-field data. (a) The total near-field data with defective vias, (b) The total near-field data without defective vias, (c) the radiation from only the defective vias. 73
Fig3.17 Detection of the defective vias in a SIW coupler. 76

Fig3.18 Material assignment and field variation (at 1.84GHz) for the SIW filter, (a) material assignment, (b) $|H_x|$ and (c) $|H_y|$ variation. 77
Fig3.19 Classification of the reconstructed near-field samples, (a) the labels for the classification algorithm , (b) scatterplot, (c) parallel coordinates plot, (d) ROC graph, and (e) confusion matrix. 80

Fig4.1 The orientation of the magnetic probes in RFX2. At each measurement point, the probe is $X-$ or $Y-$oriented 84
Fig4.2 Photograph of the planar antenna and its return loss and. (a) Front view of the antenna. (b) Back view of the antenna. (c) $|S_{11}|$ of the antenna simulated using HFSS and CST, and measured result. 93
Fig4.3 The spectral density of flicker noise. 93
Fig4.4 Relative error of various interpolation algorithm methods versus different values of SNR(dB). 94
Fig4.5 The uniformly and adaptively sampled near-field of the AUT, and the initial samples for the adaptive algorithm, in three frequencies, 1.51GHz, 3.5GHz, and 4.75GHz. 95
Fig4.6 Single scan and total test time calculation in case of a single probe measurement [82]. 97
Fig4.7 The antenna measurement setups. (a) Near-field measurement using an RFX2. (b) Measurement setup in an anechoic chamber including the AUT and the waveguide probe. 97
Fig4.8 The far-field pattern of the antenna at three frequencies, obtained from full-wave simulation and various measurement and sampling techniques. . . . 98
Fig4.9 Relative error of various interpolation algorithms versus different values of SNR(dB). 99
Fig4.10 Schematic representation of the source reconstruction method. 101

Fig4.11 Near -field radiation of the antenna under test and different sampling algorithms. (a) Near-field radiation. (b) Uniform sampling. (c) Adaptive sampling. 104
Fig4.12 Clustering the measured near-field. (a) Elbow method to determine the optimal number of clusters. (b) Clustered data over XYZ plane. (c) Clustered data over θ and phi plane. 105
Fig4.13 Spherical near-field measurement setup and far-field pattern of antenna. (a) Measurement setup. (b) Far-field pattern of the antenna. 106

List of Tables

Table 2.1 Comparison of DOFs for RWG-via-LCN and LCN methods for three antenna 45

Table 4.1 The comparison between the uniform and adaptive sampling techniques for the near-field of the AUT at 3.5GHz 96

Contents

1 Review of Literature **1**

1.1 Introduction 1

1.2 Antenna Radiation Pattern Measurement 2

1.3 Far-Field Measurements 2

1.4 Compact Range Measurements 4

1.5 Near-Field Measurements 5

1.6 Planar Near-Field Measurements 6

1.7 Cylindrical Near-Field Measurement 8

1.8 Spherical Near-Field Measurement 10

1.9 Planar Wave Spectrum (PWS) and its drawbacks 12

1.10 RWG-via-LCN method 18

1.11 High Resolution Near-Field Measurement and Fault Detection in SIW Circuits 22

1.12 Adaptive Sampling of the Near-Field Data 24

2 RWG MoM-via-Locally Corrected Nyström Method in Near-Field to Far-Field Transformation Using Very-Near-Field Measurement **27**

2.1 Introduction 27

2.2 Theory 28

2.2.1 Locally Corrected Nyström method 30

2.2.2 RWG MoM 35

2.2.3 RWG via the first-order LCN 37

2.2.4 Degrees of freedom (DOFs) and condition number of the impedance matrices . . . 41
2.3 Measurement and numerical results . . . 45
2.4 Conclusion . . . 48

3 Detection of the Defective Vias in SIW Circuits from Single/Array Probe(s) Data Using Source Reconstruction Method and Machine Learning 49
3.1 Introduction . . . 49
3.2 The Proposed Method . . . 50
3.2.1 Source reconstruction method . . . 52
3.2.2 Field and material variation . . . 57
3.2.3 The aperture model for the defective vias in the SIW structure . . . 59
3.2.4 The patch antenna model of the interaction between the SIW structure with the ground plane of the probe array . . . 60
3.3 Measurement and Simulation . . . 67
3.4 Conclusion . . . 81

4 Accuracy and Time Enhancement of Near-Field Antenna Measurement Considering Noise, Using an Adaptive Data Acquisition and Interpolation Technique 82
4.1 Introduction . . . 82
4.2 Uniform sampling, interpolation techniques and source reconstruction method 83
4.3 Noise modeling . . . 86
4.4 Adaptive sampling algorithm in planar near-field antenna measurement . . . 89
4.4.1 Exploration . . . 90
4.4.2 Exploitation . . . 90
4.4.3 Adaptive data sampling selection . . . 92
4.4.4 Measurement and simulation results . . . 92

4.5 Adaptive data acquisition and clustering technique in spherical near-field antenna measurement . . . 100
4.5.1 Exploration . . . 100
4.5.2 Exploitation . . . 101
4.5.3 Adaptive data sampling selection . . . 102
4.5.4 Measurement and simulation results . . . 102
4.6 Conclusion . . . 107

5 Conclusion and Future Work **108**
5.1 Conclusion . . . 108
5.2 Suggestions for Future Work . . . 109

6 List of Publications **111**
6.1 Journals . . . 111
6.2 Conferences . . . 112

Chapter 1

Review of Literature

1.1 Introduction

Antenna pattern measurement on a conventional far-field range is most of the time impossible due to the very long radiating far-field distance. Thus, it is desirable to determine the far-field pattern of the antenna from the measured near-field data. Moreover, it is important to include electromagnetic compatibility (EMC) very early in the design phase of PCBs and microwave circuits, and near-field data provide detailed information about the radiation sources of the circuts. Yet for the near-field techniques, accurate near-field to far-field transformation and post-processing algorithms are essential to have valid results. Also, a technique such as adaptive sampling is required to decrease the number of samples.

In this chapter, first, the antenna radiation measurement techniques are explained including far-field, compact range, and near-field methods. Second, the three main near-field measurement configurations, namely planar, cylindrical, and spherical are discussed. Then the plane wave spectrum and the methods that help to increase the accuracy and speed of the near-field to far-field transformation are described. Thereafter, a literature review about fault detection of the circuits and PCBs is conducted. Finally, the algorithms to decrease the number of required samples and time of measurement are reviewed.

1.2 Antenna Radiation Pattern Measurement

The field of antennas is usually divided into three regions: reactive near-field, radiating near-field, and far-field region as depicted in Fig. 1.1. In the closest area around the antenna, the radiation field is mainly reactive. The expanse of this region is approximately $0 < r < \lambda_0/2\pi$, where r is the distance between the antenna and the observation point, and λ_0 is the wavelength. The field decreases faster than $1/r$. The second region, radiating near-field, is in the range of $\lambda_0/2\pi < r < 2d^2/\lambda_0$, and d is the diameter of the smallest sphere which encompasses the antenna. Since we can ignore the mutual coupling between the antenna under test (AUT) and the measuring probe in this area, this is the region for near-field measurements. When we approach the boundary of this area, the field decays as $1/r$ although the radiation pattern is still dependent on r. The third region (i.e.,$r > 2d^2/\lambda_0$) is the far-field of the antenna in which radiation pattern is independent of r. For direct far-field measurement, between the center and the edge of the AUT, a phase difference of $\pi/8$ is required. For more accurate results, a larger distance between the AUT and the probe is demanded [24].

1.3 Far-Field Measurements

Far-field techniques have been widely used to evaluate the electromagnetic properties of the AUT. The measurement probes which are placed at distances larger than $2d^2/\lambda_0$ measure the far-field directly. Since at this distance quasi plane waves illuminate the probe as shown in Fig. 1.2, there is no need for probe correction.

A remote outdoor test-site is needed for the far-field measurement of large antennas. The three main outdoor ranges include elevated, slant and reflection ranges [27]. In the areas with flat ground and a clear line-of-sight, the elevated range is appropriate. In this arrangement, both the source and test antennas are set up at the same height. The directivity and side lobes of the source antenna should be chosen such that the first null in the antenna pattern

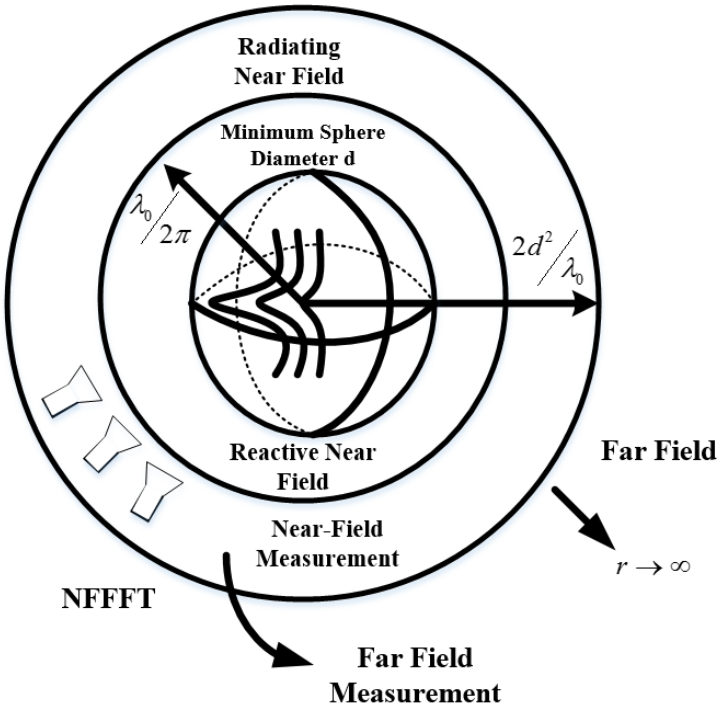

Fig. 1.1: Antenna field regions [24]

points to the base of the test antenna. The reflections of the antenna field from the ground may cause some errors. In slant ranges, which are more compact, there is not any reflection from the ground since the test antenna is mounted on a non-conducting tower, and the main beam of the source antenna is directed toward the test antenna. The source antenna is close to the ground. This configuration is depicted in Fig. 1.3. In the third approach, the reflection range, the height of the source and test antennas, and their separation distance are arranged to have constructive interference between the direct and reflected signal to provide smooth range surface. This method is used in low frequencies since it is not easy to have a smooth outdoor surface.

To have accurate results, testing the antenna in a controlled environment is desired to eliminate the effect of multipath propagation, weather conditions, electromagnetic interference, etc. The far-field measurement of the small antennas is performed easily in a controlled environment.

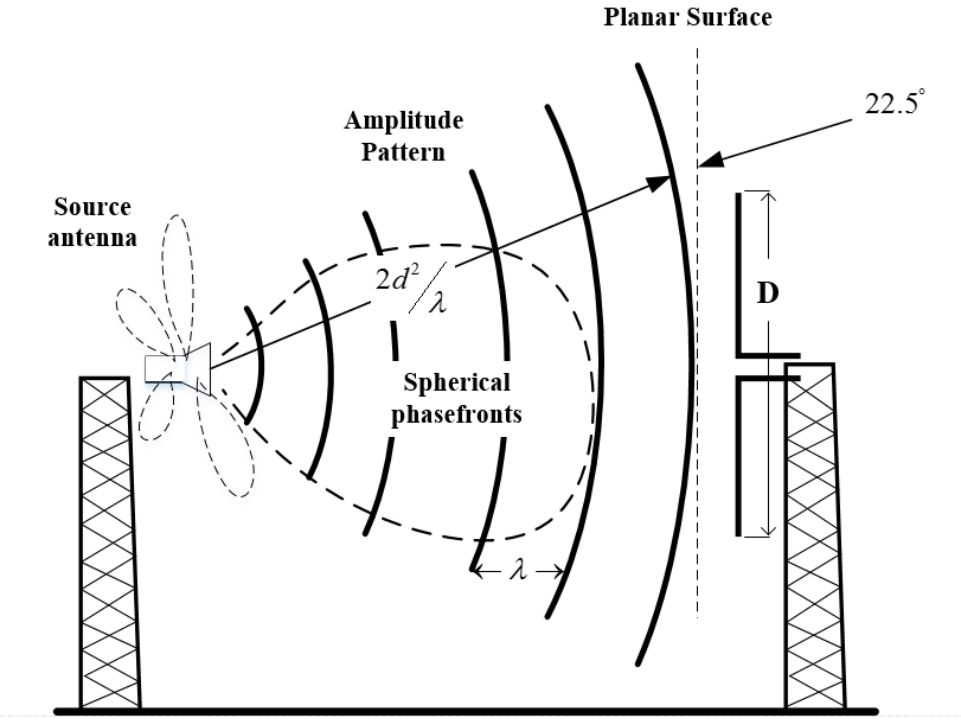

Fig. 1.2: Direct far-field antenna measurements [24]

1.4 Compact Range Measurements

To determine the AUT radiation pattern, one can use compact ranges. In this approach, the spherical wave fronts are converted to plane waves in the near-field of the antenna as shown in Fig. 1.4. The collimating lenses are used for this purpose. Higher accuracy will be achieved by testing the antenna in a controlled environment. The size and surface accuracy of the reflector specify the lower and upper operating frequency. This method is very expensive particularly if we use dual reflectors to collimate waves in two directions and compensate the cross-polar component.

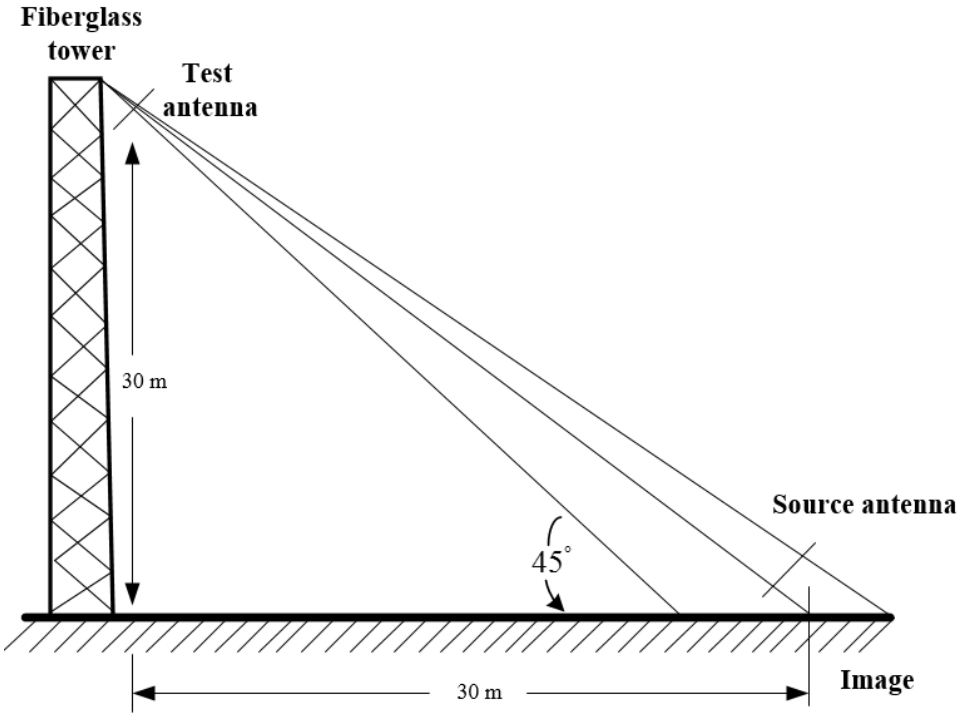

Fig. 1.3: Far-field measurement setup for slant ranges [24]

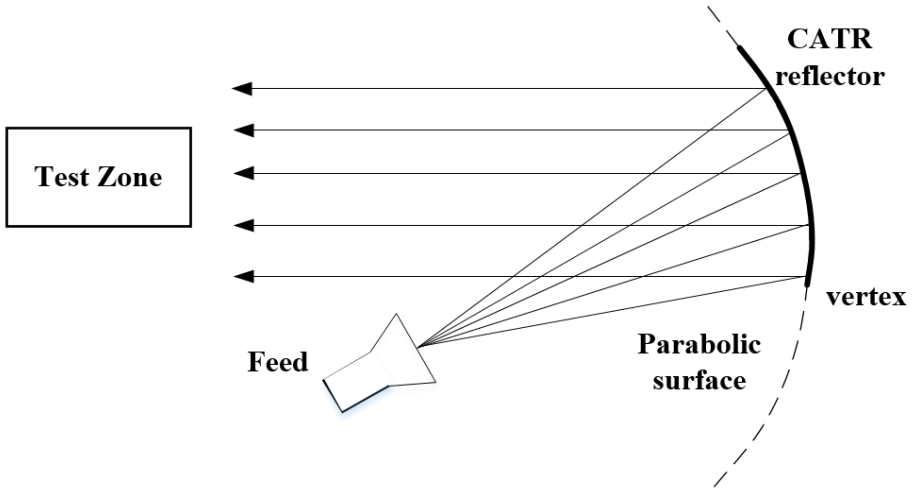

Fig. 1.4: Antenna measurement using compact ranges [24]

1.5 Near-Field Measurements

A promising alternative to far-field and compact range measurements is near-field techniques. Such approaches apply a well-developed algorithm to the measured radiating near-

field of the antenna for transforming near-field to far-field. Since all of the measurements can be done in a controlled environment, they are more accurate. The underlying theory is Huygen's theorem, stating that the knowledge of the tangential field components on a closed surface is enough to compute the fields out of that enclosed volume. In other words, the radiating object can be replaced with the equivalent sources as shown in Fig. 1.5. A variety of sources yield the same fields as the measured ones in the near-field of the AUT. The choice of a specific source determines the geometry of the near-field scanning surface that can be assumed in various forms, the most common of which are planar, cylindrical, and spherical. The measurement probe collects all of the fields close to the measurement point, r_M, and the probe output is [24] (Fig. 1.6)

$$U(r_M) = \iiint_{V_{probe}} \vec{W}_{probe}(r).\vec{E}(r)\, dV \tag{1.1}$$

$\vec{W}_{probe}$ is the spatial weighting function of the probe. We need to consider the effect of the probe in the transformation algorithm, which is termed as probe correction. The accuracy of the near-field methods relies on the precision of the measured fields and the algorithms that are used for NF-FF transformation.

1.6 Planar Near-Field Measurements

Planar near-field measurement is the most simplified method for NF-FF transformation. This method is more applicable to medium- to high-gain antennas. The measurements are usually performed on a finite plane at an appropriate distance from the AUT. Conventionally, the probe moves on the measurement plane and AUT is fixed. The probe goes one step either vertically or horizontally in one direction and then sweeps in the orthogonal direction. Ideally, the measurement plane should be infinite, but its size is confined due to such practical considerations as the size of the scanner and the anechoic chamber; consequently, the reliable region in the far-field pattern of the antenna is confined as well. The size of the scanner

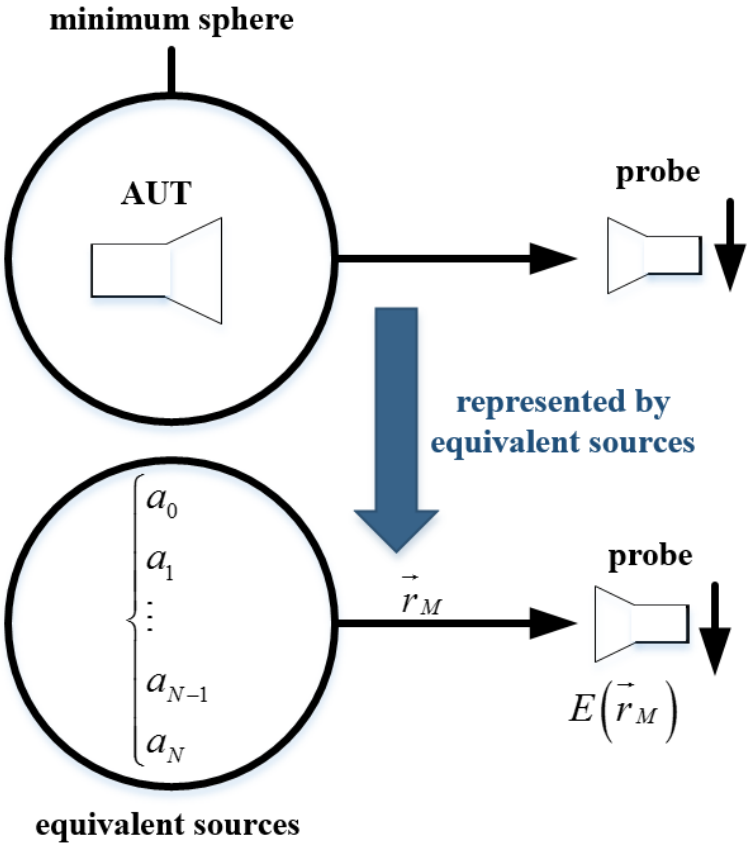

Fig. 1.5: Representation of an antenna using equivalent sources [24]

is normally selected such that at the edges we have less than -35dB pattern level [24]. It is proven analytically and experimentally that the valid far-field angular region is up to (Fig. 1.7)

$$\phi_{valid} = tan^{-1}(\frac{L_\phi - d_\phi}{2a}) \tag{1.2}$$

$$\theta_{valid} = tan^{-1}(\frac{L_\theta - d_\theta}{2a}) \tag{1.3}$$

where L_ϕ and L_θ are the length and the width of the measurement plane, respectively, a is the distance between the AUT and measurement plane, and d_θ and d_ϕ are the dimensions of the AUT. In the planar measurement, based on the position of the probe relative to the

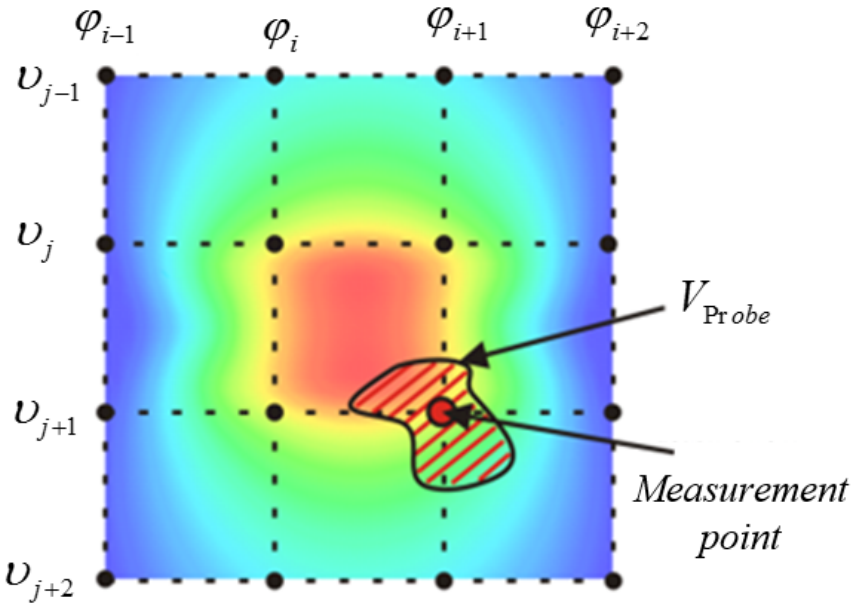

Fig. 1.6: Measurement of near-field and output signal of the probe at discrete points [24]

AUT, the main beam of AUT might be received with the main beam or side lobe of the probe as depicted in Fig. 1.8. Thus, the signal which is collected by the probe should be weighted with its pattern. In the planar NF-FF transformation, the measured near-fields on the scanning plane are used to find the unknown coefficients in the planar expansion of the radiated field.

1.7 Cylindrical Near-Field Measurement

For fan beam antennas that have a broad band beam in one plane and a narrow beam in the orthogonal plane, cylindrical near-field measurements are more appropriate [24]. The cylindrical modal expansion is used to represent the radiated fields. The probe moves on a cylindrical surface by stepping in one direction (ϕ or z) and sweeping in the orthogonal direction as shown in Fig. 1.9. Since the height of the cylinder on which scanning takes place is finite, the resultant far-field of NF-FF transformation is valid up to a certain amount of θ and ϕ

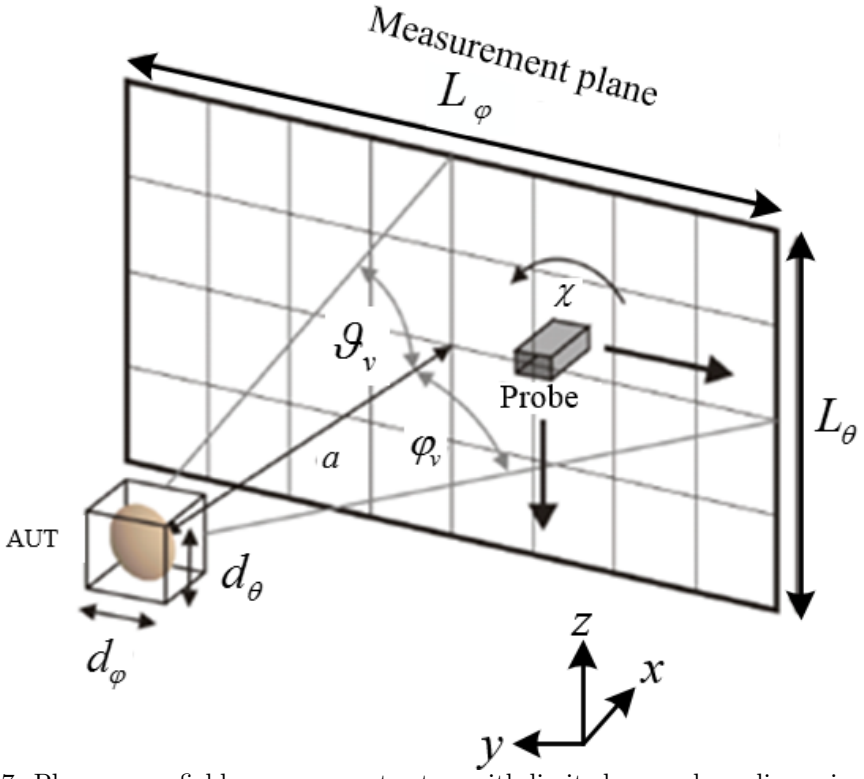

Fig. 1.7: Planar near-field measurement setup with limited scan plane dimensions [24]

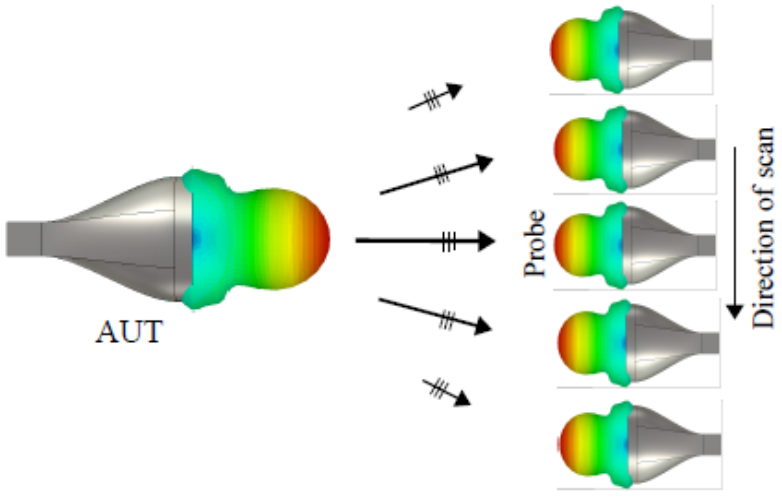

Fig. 1.8: The influence of probe position relative to the AUT in near-field measurement [24]

$$\theta_{valid} = tan^{-1}(\frac{L_\theta - d_\theta}{2a}) \tag{1.4}$$

$$\phi_{valid} = \phi_t - arcsin(\frac{\rho_0}{a}) \tag{1.5}$$

where L_θ is the length and a is the radius of cylindrical measurement surface, d_θ is the length and ρ is the radius of the smallest cylinder enclosing the AUT, and ϕ_t is the angle of near-field measurement [24]. Like the planar case, the truncation level of -35dB at the edges is adequate. When the probe gets closer to the AUT, the SNR and valid angular region increase as shown in Fig. 1.10 while more multiple reflections between the AUT and the probe occur.

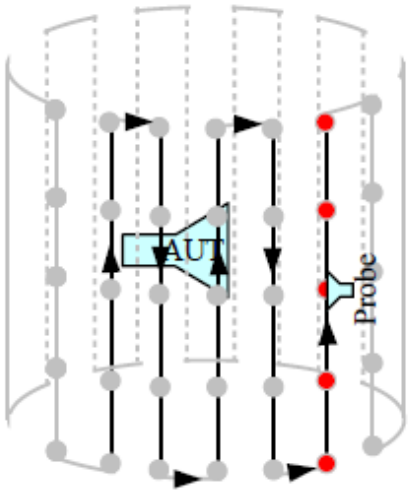

Fig. 1.9: Cylindrical near-field measurement. Probe is moving in the vertical direction (step in ϕ) [24]

1.8 Spherical Near-Field Measurement

Spherical scanning is the most general near-field measurement system, so it is suitable for all kinds of antennas and uses spherical modal expansion to represent the radiated field of the AUT [24]. Again the probe moves on a cylindrical surface by stepping in one direction (ϕ or θ) and sweeping in the orthogonal direction as shown in Fig. 1.11. When a complete scanning is not required, the valid angle is

$$\phi_{valid} = \phi_t - arcsin(\frac{a}{d_s}) \tag{1.6}$$

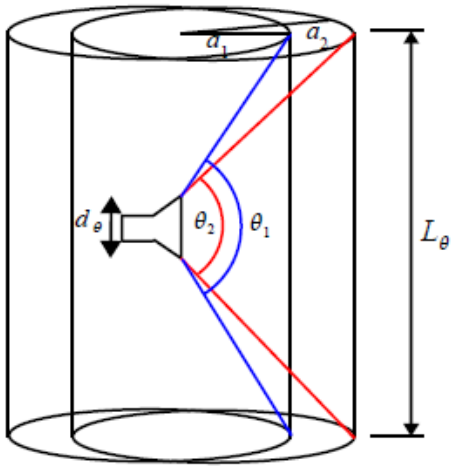

Fig. 1.10: Valid angle in cylindrical near-field measurements [24]

$$\theta_{valid} = \theta_t - arcsin(\frac{a}{d_s}) \tag{1.7}$$

where θ_t and ϕ_t are the angles of near-field measurements, a is the radius of the smallest sphere that encompasses AUT, and d_s is the radius of the smallest sphere that encompasses the measurement surface [24].

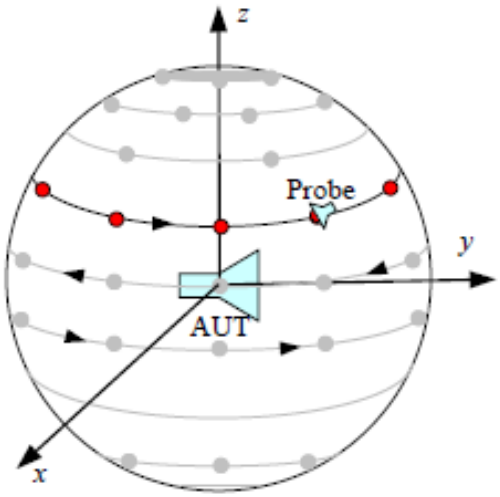

Fig. 1.11: Spherical near field measurement [24]

1.9 Planar Wave Spectrum (PWS) and its drawbacks

In a source-free free-space region such as the near-field of the antenna, the time harmonic Maxwell's equations can be transformed into the following vector wave equations [2]:

$$\nabla^2 \vec{E} + k^2 \vec{E} = 0 \tag{1.8}$$

$$\nabla^2 \vec{H} + k^2 \vec{H} = 0 \tag{1.9}$$

$$\nabla . \vec{E} = \nabla . \vec{H} = 0 \tag{1.10}$$

k is the amplitude of wave vector. If we assume that the antenna is placed in the region $z \leq 0$ (Fig. 1.12) and the measurement plane is on $z = z_t$, then it can be shown that a solution to the Maxwell's equation is [2]

$$\vec{E}(x, y, z) = \frac{1}{2\pi} \int_{-\infty}^{\infty} \int_{-\infty}^{\infty} \vec{A}(k_x, k_y) e^{-j\vec{k}.\vec{r}} dk_x dk_y \tag{1.11}$$

$$\vec{H}(x, y, z) = \frac{1}{2\pi} \int_{-\infty}^{\infty} \int_{-\infty}^{\infty} \vec{k} \times \vec{A}(k_x, k_y) e^{-j\vec{k}.\vec{r}} dk_x dk_y \tag{1.12}$$

$$k_x A_x(k_x, k_y) + k_y A_y(k_x, k_y) + k_z A_z(k_x, k_y) = 0 \tag{1.13}$$

where k_x and k_y are real values and $\vec{A}$ is the plane wave spectrum since $\vec{A}(k_x, k_y) e^{-j\vec{k}.\vec{r}}$ represents a uniform plane wave, which propagates in the direction $\vec{k}$. The radiation condition for $z \geq 0$ is

$$k_z = \begin{cases} (k^2 - k_x^2 - k_y^2)^{\frac{1}{2}}, & \text{if } k_x^2 + k_y^2 \leq k^2 \\ -j(k_x^2 + k_y^2 - k^2)^{\frac{1}{2}}, & \text{otherwise} \end{cases} \tag{1.14}$$

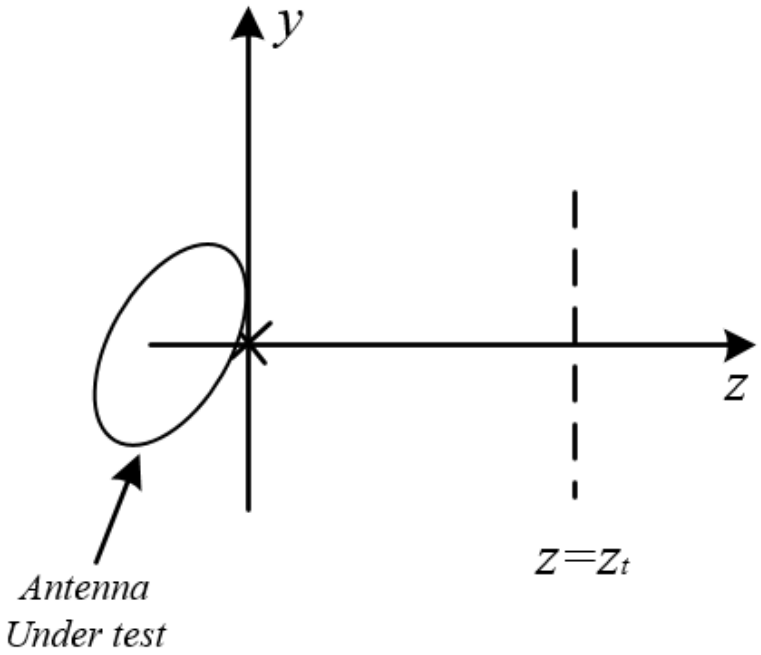

Fig. 1.12: Planar near-field measurement [2]

An imaginary k_z describes an evanescent PWS, which is rapidly attenuated away from the $z = 0$ [2]. Therefore, at $z = z_t$ the measured fields are

$$E_x(x, y, z_t) = \frac{1}{2\pi} \int_{-\infty}^{\infty} \int_{-\infty}^{\infty} A_x(k_x, k_y) e^{-jk_z z_t} e^{-j(k_x x + k_y y)} dk_x dk_y \tag{1.15}$$

$$E_y(x, y, z_t) = \frac{1}{2\pi} \int_{-\infty}^{\infty} \int_{-\infty}^{\infty} A_y(k_x, k_y) e^{-jk_z z_t} e^{-j(k_x x + k_y y)} dk_x dk_y \tag{1.16}$$

when $z = 0$,

$$E_x(x, y, 0) = \frac{1}{2\pi} \int_{-\infty}^{\infty} \int_{-\infty}^{\infty} A_x(k_x, k_y) e^{-j(k_x x + k_y y)} dk_x dk_y \tag{1.17}$$

$$E_y(x, y, 0) = \frac{1}{2\pi} \int_{-\infty}^{\infty} \int_{-\infty}^{\infty} A_y(k_x, k_y) e^{-j(k_x x + k_y y)} dk_x dk_y \tag{1.18}$$

From (1.17) and (1.18), the following transform is obtained

$$A_x(k_x, k_y) = \frac{1}{2\pi} \int_{-\infty}^{\infty} \int_{-\infty}^{\infty} E_x(k_x, k_y, 0) e^{-j(k_x x + k_y y)} dk_x dk_y \tag{1.19}$$

$$A_y(k_x, k_y) = \frac{1}{2\pi} \int_{-\infty}^{\infty} \int_{-\infty}^{\infty} E_y(k_x, k_y, 0) e^{-j(k_x x + k_y y)} dk_x dk_y \tag{1.20}$$

Therefore, there is a simple relationship between the far-field pattern and the PWS of an antenna

$$\vec{E}(x, y, z) = \frac{j e^{-jkr}}{r} k_z \vec{A}(k_x, k_y) \tag{1.21}$$

To include all the spectral and spatial energies, the samples in (x, y) and (k_x, k_y) should be enough. The aperture size and the plane wave spectrum of directive antennas are finite. If the measurement plane is placed in a region of space where evanescent waves are negligible, then the maximum k_x and k_y wavenumbers are $k_{xm} = k_{ym} = k = 2\pi/\lambda$. Therefore, the sample spacing is $\Delta x = \Delta y = \lambda/2$ [2]. N_x and N_y must be large enough to contain all the significant fields in the aperture. A sampling rate of five times of Nyquist rate is necessary when the plane wave spectrum of the AUT is completely unknown [6]. Nowadays, however, there is an extensive knowledge of the far-field pattern of various directive antennas. For a uniformly circular aperture antenna, the y component of the electric field (on the aperture $E_y = 1$) along the z axis, obtained from a computer simulation, is shown in Fig. 1.13 [2]. The diameter of the antenna, which is polarized in y direction, is 10λ. The sampling is done such that $\Delta x = \Delta y = \lambda/2$ and $N_x = N_y = 64$. A filter is used to remove the evanescent waves. There is a slight difference between the simulation and the exact solution.

Since at close distances from the AUT (i.e., $z < \lambda$) there are still evanescent modes which are not attenuated adequately, there is a small discrepancy between the exact solution and the one that is obtained from the simulation. For $z > \lambda$, the shift is because the sharp step function at the edge of the antenna is not precisely represented by the sampling space $\Delta x = \Delta y = \lambda/2$. When one takes into account the evanescent waves and increases the

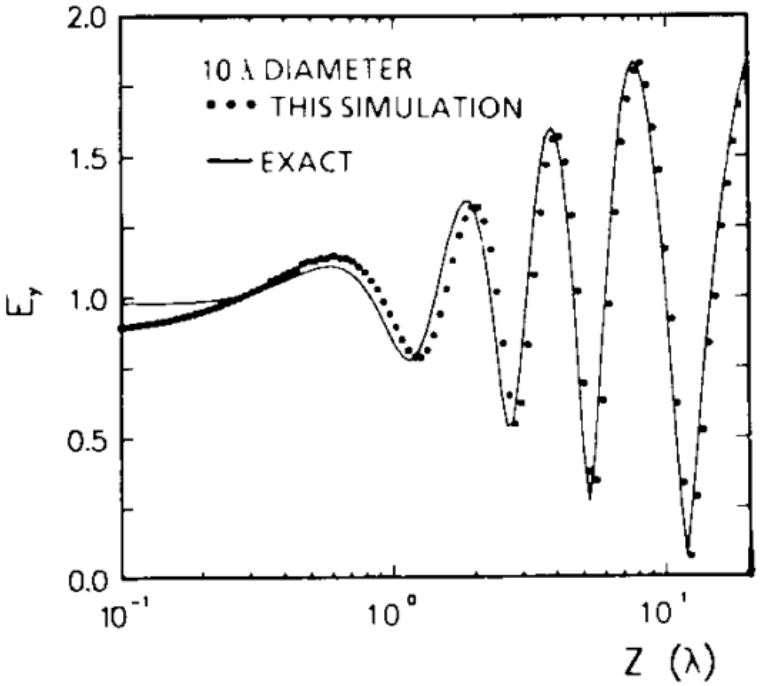

Fig. 1.13: Computer Simulation and exact solution of y component of electric field along z axis for a uniformly circular aperture antenna. The diameter of the antenna is 10λ, and $\Delta x = \Delta y = \lambda/2$ and $N_x = N_y = 64$ [2].

number of samples, the result of the simulation is in a perfect agreement with the exact solution as depicted in Fig. 1.14.

To investigate the effect of the sharp edges of the aperture distribution on the simulation results, it is assumed that the aperture tapers gradually from unity to zero based on a parabolic function by getting closer to the edges. In Fig. 1.15, E_y at $y = 0$ and $z = 100\lambda$ is plotted along the x axis. As shown in Fig. 1.15, the resulting fields are independent of the sample spacings when they are less than $\lambda/2$.

A window or filter is frequently used in signal processing of the PWS data for near-field measurement. There is no advantage in using the filter or window if space samplings are less than 0.5λ. Moreover, the window usually causes the in-band distortion which may affect its benefit. In [6], an equalizer algorithm is employed to compensate for the resultant in-band distortion of the Blackman filter. A slight decrease of the sample spacings is more efficient than the use of window to smooth the out-of-band spectra. Because small sampling is not

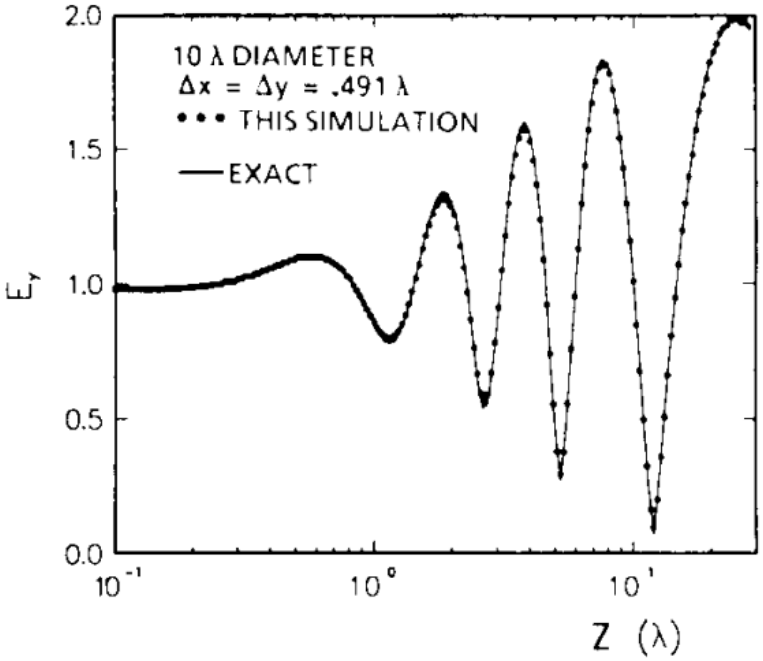

Fig. 1.14: Computer Simulation and exact solution when the sample spacing in Fig. 1.13 is reduced to $\Delta x = \Delta y = 0.491\lambda$ [2].

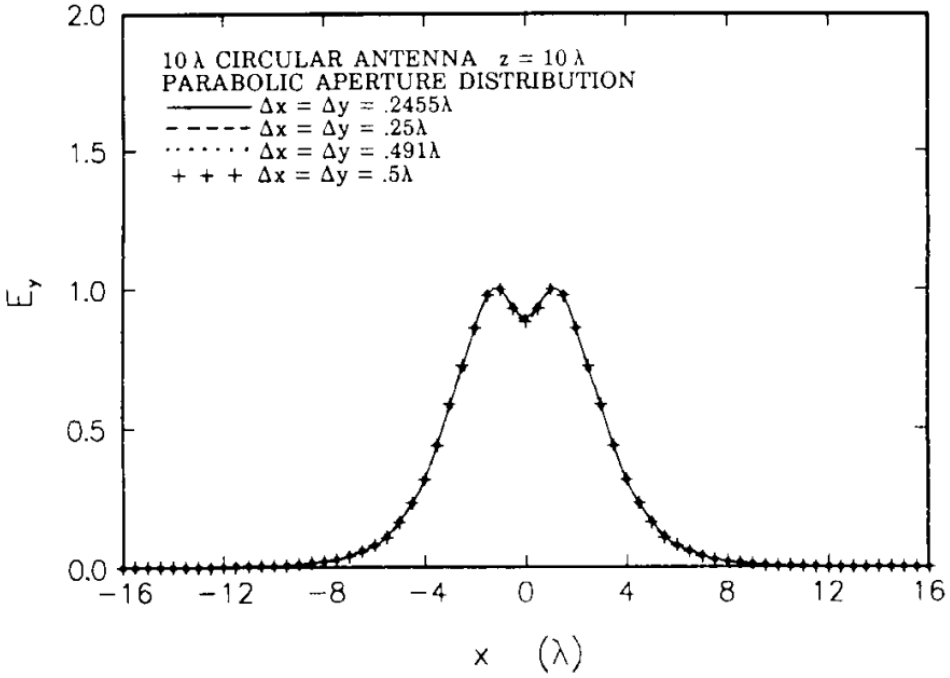

Fig. 1.15: Simulated E_y along x axis with different sample spacings [2].

always possible due to the practical limitations, one needs to use window [29]; otherwise, direct integral equation methods must be employed.

In the PWS context, an evanescent wave is denoted by an imaginary k_z which is attenuated by the term $exp(-jk_z z_t)$ as the field point moves along the z axis in the positive direction. The scanning plane is placed at $z = z_t$ that is assumed to be large enough to exclude the evanescent waves. Although the scanning plane in near-field measurements is positioned at least a few wavelengths (typically ten wavelengths) away from the AUT, the evanescent PWS for practical antennas can be simply ignored at the distances larger than one wavelength from the measurement plane; this is especially the case for large antennas due to their insignificant evanescent content. That the impact of the evanescent waves has been overemphasized can be inferred from Fig. 1.13. As mentioned previously, all of the evanescent content is filtered out in this simulation; however, there is only $0.1dB$ error at a few lengths away from the antenna and $0.9dB$ error at $z_t = 0.1\lambda$. In Fig. 1.16, the same problem is simulated with sample spacings of 0.2445λ on a 128×128 array and with all of the evanescent waves removed. This figure demonstrates that the effect of the evanescent PWS is limited to $z_t < 1\lambda$ as stated clearly in [30].

For tapered apertures, there is less reactive energy and evanescent content. The AUT in Fig. 1.17 is similar to the one in Fig. 1.13, except for its parabolically tapered aperture distribution. The resultant fields along the axis are similar when the filter is on (i.e., the evanescent mode is excluded) and off (i.e., the evanescent mode is included).

The increase of the aperture size causes the decrease of the evanescent modes. The reason, based on the Huygen's theorem, is that the contributing sources are mainly far away from the field point and more radiation energy is expected.

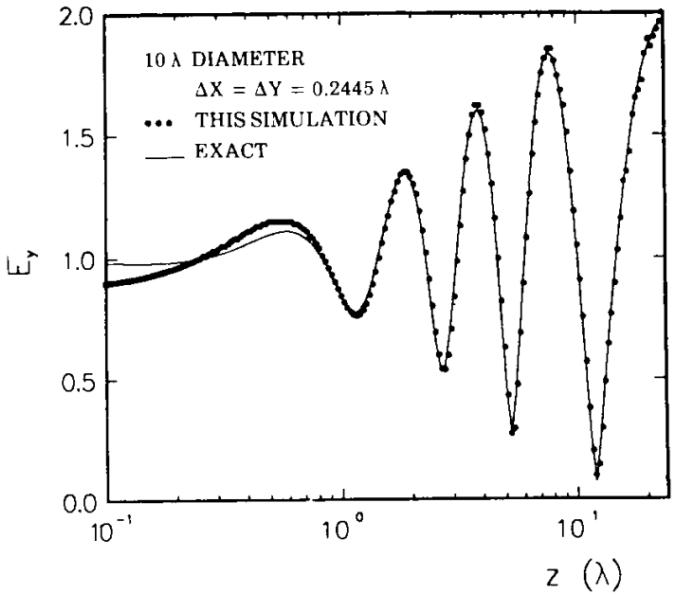

Fig. 1.16: Computer Simulation and exact solution with the sample spacing of $\Delta x = \Delta y = 0.2445\lambda$ on 128×128 array [2].

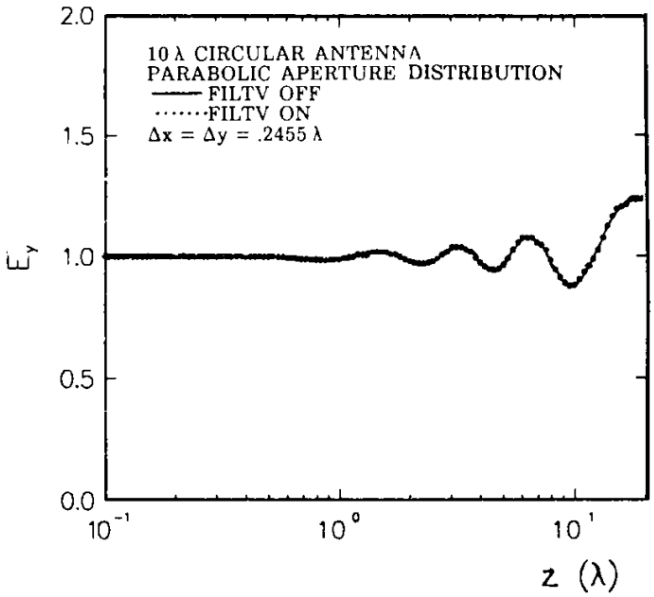

Fig. 1.17: The effect of inclusion and exclusion of the evanescent content on a parabolically tapered aperture distribution [2]

1.10 RWG-via-LCN method

In the PWS method, the radiated fields of the AUT are expanded in terms of planar wave functions. Then, the measured near-fields are used to calculate the expansion coefficients [2]-

[5]. To reconstruct the currents on the source plane, one can take the two dimensional Fourier transform of the measured fields to obtain the far-field that is converted into the equivalent sources by inverse Fourier transform. A drawback of this technique is that the fields are assumed to be zero outside of the measurement plane. This hypothesis causes a systematic error and spurious side lobes in the calculated far-field [3]. Some spatial low-pass filters have been used to force fields to become zero gradually as we get closer to the measurement plane edges and consequently relieve such side lobes [6] and [7]. However, these filters may cause some distortion. As it is mentioned in [3], if we assume the measurement plane and the source plane (the plane which contains the sources) are of dimensions $L \times L$ and $D \times D$, respectively, and the separation distance between them is d, then PWS theory remains valid up to $\theta = \tan^{-1}(\frac{L-D}{2d})$. Therefore, the accuracy of PWS method depends on the size of measurement and source plane, their distance, and the extent to which we can ignore the evanescent waves.

An alternative method is utilizing near-field data to determine equivalent current sources over a fictitious planar surface which encompasses the radiating surface of the AUT [3] and [8]- [11]. The electric field integral equation (EFIE) and magnetic field integral equation (MFIE) are used to relate the measured near-field to the equivalent currents. If someone knows the currents on the source plane, one can obtain fields at every plane, which is placed at an offset from that. When the measurement plane is infinite, the PWS method and the integral equation technique result in the same equations. The PWS and equivalent current approaches solve the integral equation in the spectral domain and space domain, respectively. In the equivalent current technique, measurement plane data are transferred to the source plane through the Green function before applying Fourier transform to the data to calculate the far-fields. The fields are not assumed to be zero outside of the measurement plane when the Green function is utilized. Therefore, the truncation error is small compared to PWS, and the results hold up to a larger azimuth angle [3].

Usually the method of moments (MoM) is employed to convert the integral equations to matrix forms. In the MoM approach, the surface currents are expanded in terms of the basis

functions (BFs) whose unknown coefficients are ascertained by the process. Not only the current BFs represent the current distribution, but also they approximate the charge distribution through continuity equation (charge distribution being calculated by divergences of current BFs). Therefore, it must be confirmed that the BFs are continuous in the normal direction of the current flow; otherwise, there is an undesired and artificial charge accumulation along the edges of the basis elements. This legitimate and important feature can be fulfilled with the use of the Rao-Wilton-Glisson (RWG) BFs [12].

A drawback of classical element or basis-based MoM discretization scheme is that it is not suitable for efficient acceleration with fast algorithms such as the multilevel fast multipole method (MLFMM); this is a limitation for real-time applications [13]- [16]. The locally corrected Nyström method (LCN), which does not use the expansion of basis functions, is a point-based alternative to the MoM to solve integral equations [17]. It utilizes the samples of solution at the nodes of a Gaussian quadrature rule. The LCN technique has been used to discretize EFIE for scattering problems, including PEC and penetrable scatterers, by applying surface and volume integral equation approaches. One of the unique potentials of LCN method is that any integration rule can be used to discretize the unknowns of integral equations. Nonetheless, the indiscriminate application of this idea to EFIE and MFIE leads to imprecise near-field and far-field results. This imprecision is due to the current discontinuity and inconsistent charge representation. Although the significance of the current continuity recedes for the higher-order discretization schemes, it has a substantial impact on lower orders such as the classical zero- and first-order MoM and LCN.

As demonstrated in [18], MoM and LCN are equivalent under certain conditions, and LCN can be considered as a specific point-based representation of MoM. In [19] and [20], this equality is extended to the case of RWG MoM and first-order LCN discretization scheme for triangular patches on the surface of a PEC scatterer. Then an exact relationship between impedance matrices, produced by these two systems, is established. This method, which is entitled as RWG-via-LCN, integrates the benefits of the two approaches. It maintains current continuity between adjacent mesh patches and is more appropriate for speeding up

by MLFMM. Also, a comparable relationship is developed in [20] between the RWG MoM and LCN to solve EFIE in the mixed-potential (MP) form termed as MP RWG-via-LCN. While the contributions of the line charge to the MP formulation are cancelled analytically, those to the vector-potential formulation of EFIE are cancelled numerically; the accuracy of the solution is remarkably higher with analytical cancellation.

In this study, the LCN discretization scheme for the first time used for the equivalent current technique in the application of near-field measurement of the antennas and PCBs to reconstruct equivalent magnetic and electric currents. The motivation is that for the real-time near-field measurement devices such as RFX2, an accurate and high-speed method is needed, and LCN is more suitable for fast algorithms. To achieve an accurate current, the same as that in [20], a relationship between LCN and RWG MoM is established. For such applications, the formulation is different since both source and observation points are on triangular patches in scattering problems. Thus, as stated in [20], one can do Galerkin's testing and choose ramp functions as the basis and test functions. This choice plays a prominent role in the analytical cancellation of the line charge contributions. In the planar near-field measurements, the observation points correspond to the array of measurement probes, so we test the field only at one point and in a scalar fashion. In scattering problems, one needs to determine the induced electric current on the surface of the scatterer, so RWG-via-LCN in [19] and MP RWG-via- LCN in [20] are developed for EFIE. In this study, LCN and RWG MoM have been linked to calculate EFIE to reconstruct electric and magnetic currents. Because the currents are reconstructed on a planar surface, the simultaneous reconstruction of magnetic and electric currents helps to extrapolate far-field toward $\theta = 90^{\circ}$ more accurately. The proposed algorithm combines the benefits of the current continuity of RWG MoM and more efficient acceleration by fast algorithms of LCN. Like [20], lower degrees of freedom (DOF) compared to LCN, increased accuracy, and better conditioning of the impedance matrix have been found in this method. The currents will be reconstructed on 3D surfaces to impose boundary conditions that increase the accuracy.

1.11 High Resolution Near-Field Measurement and Fault Detection in SIW Circuits

Near-field measurements have been widely used in circuit performance and failure analysis. The radiating sources, charge, and current distribution can be quantitatively identified by analyzing the near-field data of the circuit surface. For instance, in [31], the near-field interference between two multilayer printed circuit boards (PCBs) was estimated. In [32], a method of evaluating the current distribution on a microstrip transmission line of a multilayer PCB was introduced. An improved nonintrusive near-field probing technique for the identification of distributed effects in a high power GaN HEMT has been proposed in [33]. Also, a measurement system for on-wafer characterization of antennas operating in the high millimeter wave (MMW) to sub-MMW bands was presented in [34].

Some methods are proposed to test and inspect the PCB boards. All these techniques can be categorized into two groups: automated optical inspection (AOI) and X-ray-based approaches, [35] and [36]. AOI is a visual method in which the board is lit by several sources from different angles and scanned by one or more cameras. The recorded images are compared to what the board should look like. This method is not a proper choice when the board is highly loaded or some connections or components, such as the inner walls of the SIW (substrate integrated waveguide) vias, are hidden. Unlike AOI light sources, X-rays penetrate through the board and can give a complete image of the board. Very complex and densely loaded boards can be inspected using X-rays, but X-ray based methods are very expensive and require safety considerations. Moreover, none of these methods utilizes the electromagnetic emissions of the board to detect inner faults such as defective walls of the SIW vias.

In this study the source reconstruction method (SRM) is utilized to detect the radiated emissions of the defective vias. This work is introduced briefly in [37]. Similar idea, named matrix method, is previously used in [38] for diagnosis of phased array. Yet in [38] matrix

method is used to determine the number of elements in a dipole array. This method needs to be developed significantly to be applicable in detection of small features such as the defective vias. In this study, the source reconstruction method is utilized for detection of the defective vias in SIW circuits. The measured data are used to calculate the equivalent sources over the volume that encompasses the circuit. The surface of the box is discretized to flat triangular patches, and electric and magnetic currents are represented precisely by Rao-Wilton-Glisson (RWG) basis functions. To have the reconstructed equivalent currents consistent with Maxwell's equations and enforce Love's equivalence theorem, a boundary condition of zero tangential electric and magnetic field is applied just inside the volume. Point-matched and RWG tested fields for measured and boundary conditioned values are used, respectively to improve the accuracy. Unlike other fault detection approaches that rely on the reconstructed currents, the near-field in this method is calculated at close distance from the circuit using the equivalent sources. Because of the ill-posedness of the inverse problems, our solution results in better accuracy that is important in detecting small features such as defective vias. The main advantage of the proposed method is that the circuit is examined while it works in its operating frequency range.

To measure the unfavorable emissions of any device, two problems typically arise: detecting the radiating sources that is necessary for EMC troubleshooting and conducting the measurement that can be time-consuming. With respect to the detection of the radiating sources, the accurate reconstructed field close to the circuit surface provides enough information about the location of the defective vias. In this study, the radiation sources of the device are located by using the equivalence principle from the measured near-fields which enables the substitution of the original device by an equivalent current over a box that encompasses the device. Thereafter, the fields in the vicinity of the vias are computed from the equivalent current. Moreover, a machine learning based approach is proposed that uses field variation (x and y component of the magnetic fields) and material variation for all reconstructed points to differentiate the radiation sources. Both the amplitude and phase information of the tangential components of the magnetic fields across the measurement area are measured. Due to

the complexity and inaccuracy, near-field scanning with phase measurement is challenging. Thus, several magnitude-only measurement approaches have been proposed [39]- [45]. In [44] the measured magnitude of the fields over two planes along with an iterative approach has been used to retrieve the phase. In [45], two sets of data, the measured amplitude of the fields over the scanning surface and the interpolated data from the measured fields (mostly averaging) over the same plane, were utilized to retrieve the phase. Yet as it is stated in [46], capturing both the amplitude and phase of the fields results in more accurate reconstructed currents.

On the other side, in regards to the interpolation techniques, the simple methods such as averaging are not sufficiently accurate to characterize small features of vias. Hence, the selection of the appropriate interpolation algorithm demands thorough understanding of the potential radiating emissions of the DUT (device under test) and the mathematical behavior of the interpolation methods. For instance, the spline interpolation method has been used in many applications. However, this technique is oscillatory as it is based on polynomials [47]. Therefore, applying such interpolation technique may lead to some nonexisting radiating sources. Considering the aforementioned reasons, in this study both the magnitude and phase of the magnetic near-field are measured and for the near-field scanning, two procedures are presented; in the first one, a mechanically scanning single probe connected to a network analyzer is used whilst in the second one, a RFX2 [48]- [52] switched probe array enabling fast electronic scans is utilized.

1.12 Adaptive Sampling of the Near-Field Data

The main drawback of the near-field measurement is the required time to scan the AUT with a sufficient resolution to acquire all significant features, especially when the information at different frequencies is needed. The traditional way to measure is to uniformly sample the data on a plane-rectangular grid where the sampling space is small compared to the wavelength, i.e. λ, to capture all details. To make sure the number of the samples is enough

the near-fields are regularly measured in many more points than what is required.

A few methods are presented to avoid large sampling issues. In [69], the sampling resolution is not constant and, especially, the scanning distance increases and exceeds $\lambda/2$ by moving away from the measurement area. In [69] and [70], plane-polar and bi-polar scanning techniques are applied to reduce the burden of the near-field acquisition. In [71], the sampling starts from the center of the measurement plane and steps outward. The difference between the measured and extrapolated data over a loop, which encloses the scanned area, determines whether more sample points inside the loop are required or not. In [72], this algorithm is extended to spherical and cylindrical near-field antenna measurements. In [73] two measurement schemes, rectangular spiral and adaptive rectangular loop, are proposed. In the first algorithm, measurement starts at the center of the AUT aperture and proceeds outward, and since the required time to calculate the far-field is negligible compared to that of the data acquisition, the far-field accuracy is used as a criterion to terminate the near-field measurement. In the second algorithm, the area of the measurement is elongated in the direction of the maximum power by appending two rows or columns of data. All these methods still need a significant number of measurement samples. Utilizing the fast electronically switched probe array can remarkably decrease the time of the measurement. For instance, RFX2 [48] is a real-time antenna measurement device that measures the tangential components of AUT near-fields in two orthogonal directions using equally distanced 40×40 magnetic probes. But still there are some issues about this measurement tool. In this work, two problems are addressed.

First, each probe measures only one polarization of the field and because of physical confinement, at every point one probe can be fabricated. Thus, at the location of each probe, one component of the magnetic field is actually measured and the other one must be estimated by having the fields measured at four surrounding probes. Usually, a simple averaging technique is used to estimate the value of the field that clearly is not the best approach. In this study, more advanced interpolation methods such as linear, nearest, and natural neighbor are used to model the field for different SNR values, and the results are

compared to that of the simple averaging scheme.

Secondly, as mentioned earlier, the algorithm that is used for near-field to far-field transformation, plane wave spectrum (PWS), is not very accurate. The advantage of PWS method is that in the case of sinusoidal modes, the classical Fast Fourier transform can be simply utilized to calculate the expansion coefficients. Thus, this method is a proper choice for real-time application. An alternative technique to have a better accuracy is source reconstruction method (SRM) that uses the measured near-field data to reconstruct equivalent currents over a fictitious surface that encloses the AUT. The SRM methods are less sensitive to measurement distortions and noise compared to PWS-based techniques. On the other hand, the process time of the SRM method is more than that of the PWS technique. Thus, decreasing the number of samples, by removing the ones that are redundant from the measured data, improves the speed of the algorithm significantly. In this study, an adaptive sampling technique is developed that sequentially add more data in the regions with highly dynamic near-field behavior and skips the rest of the regions.

The spherical near-field measurement of antennas allows the full calculation of the far-field radiations. The post processing is considerably more complex than the planar and cylindrical near-field measurement, but the errors due to the truncation of the scan surface can be avoided [83]- [**?**]. Some methods are proposed to accelerate the NF data acquisition such as spiral scanning. In this method, the reduced number of needed NF data results in significant time saving as well as continuous movement. Inthis study the idea of adaptive sampling is applied to the spherical near-field measurement of antennas. This approach can be used for multi-probe measurement setup such as the system in [**?**]. Since it is important to use local values for the interpolation at a new point, the uniformly measured data is clustered by k-means clustering technique that helps to decide the new sample belongs to which cluster. The optimal number of clusters is determined using the well-known elbow method. In case of spherical sampling also, adaptive sampling reduced the number of samples significantly.

Chapter 2

RWG MoM-via-Locally Corrected Nyström Method in Near-Field to Far-Field Transformation Using Very-Near-Field Measurement

2.1 Introduction

In this chapter, RWG-via-LCN method is studied. The proposed algorithm combines the benefits of current continuity of the RWG MoM and the efficient acceleration of LCN. As in [20], lower degrees of freedom (DOF)compared to LCN that means less unknown coeffiecients for equivalent currents representation (e.g. in LCN we need more than four times of the number of DOFs compared to the RWG-via-LCN method.), increased accuracy, and better conditioning of the matrix are the advantages of this method. Thus, the proposed algorithm brings both speed and accuracy to near-field measurements. Moreover, since the RWG-via-LCN method is extended to the application of planar near-field measurement, this chapter shows how we can apply this approach to different applications where we have different kernels to be locally corrected. The main steps of the proposed approach in this chapter (Fig.2.1) are: 1. The tangential components of magnetic field are measured by RFX2 probe array. 2. The currents over a large enough plane that represents the antenna under test (AUT) are modeled using RWG MoM, LCN method and unknown coefficients. 3. Electric field integral equations

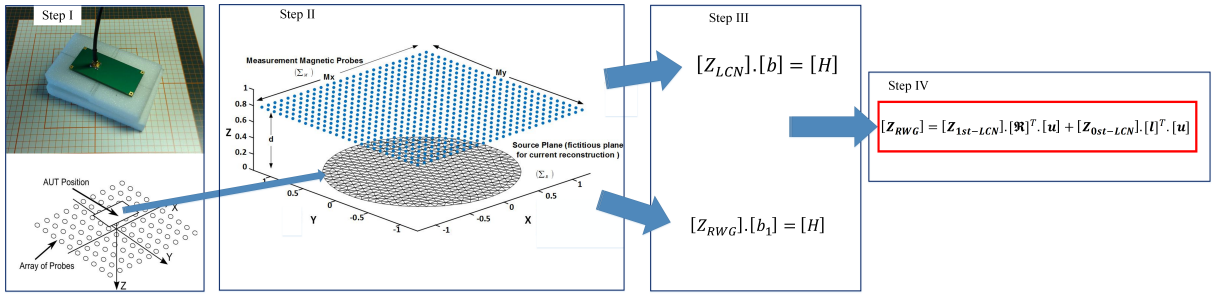

Fig. 2.1: An illustration of the main steps in LCN to RWG conversion.

(EFIE) are used to link the measured data and the equivalent currents on the source plane. The numerical calculation of these equations using the RWG MoM and LCN method results in a linear matrix relation between the measured magnetic field and the unknown coefficients of the currents. This relation is denoted as $[Z_{RWG}]$ for RWG MoM and $[Z_{LCN}]$ for LCN method. 4. A relation between $[Z_{RWG}]$ and $[Z_{LCN}]$ is developed to apply current continuity to LCN method. 5. An inverse problem is solved to find the unknown coefficients of the equivalent currents on the source plane. This chapter is organized as follows. Sections 2.1 describes the LCN and RWG MoM methods to solve EFIE in the application of planar very-near-field measurement of the antenna. The conversion from the LCN system to the RWG MoM is applied to our problem. Section 2.2 provides the simulations and measurement results that show the accuracy of the conversion. Moreover, the truncated singular value decomposition (TSVD) method is explained for solving the inverse problem.

2.2 Theory

An illustration of the current reconstruction problem is depicted in Fig.2.2. RFX2, a simple schematic of its measurement system, along with its probe array, is shown in Fig.2.2. The input data are the values of the tangential magnetic field (amplitude and phase) on the measurement plane $\sum_M$. This data might be the result of a linear operator which indicates the measurement system and sample fields interaction. The measured magnetic fields and the unknown source plane currents are linked together via EFIE [21]. The reconstruction

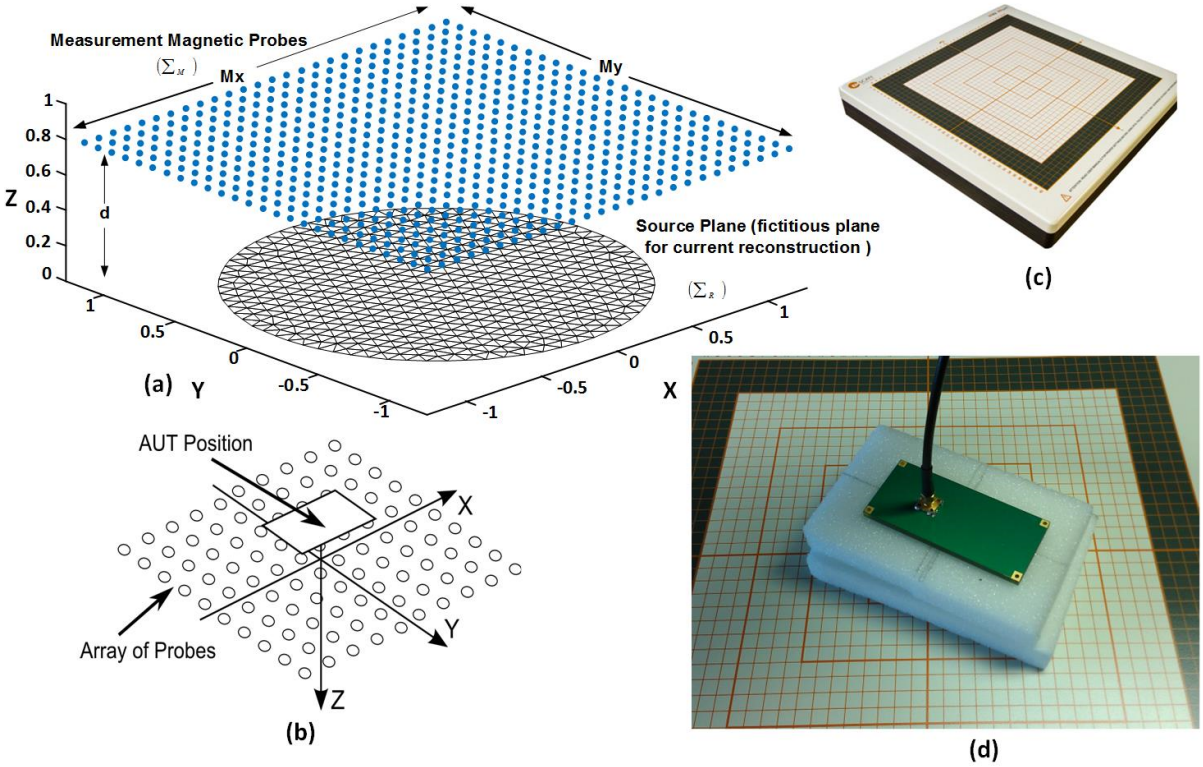

Fig. 2.2: Simulation and measurement set ups (a) Simulation setup which includes planar measurement probes, and source plane, (b) RFX2, (c) A simple schematic of RFX2 measurement system, (d) A sample of measuring an antenna with RFX2.

of both magnetic and electric currents provides a better estimation of measured fields and far-field pattern, especially towards $\theta = 90°$:

$$\vec{E}(\vec{r}) = \mathcal{K}(\vec{M};\vec{r}) - \eta_0 \mathcal{L}(\vec{J};\vec{r}) \tag{2.1}$$

where

$$\mathcal{K}(\vec{M};\vec{r}) = \int_{\sum_R} \vec{M}(\vec{r'}) \times \nabla g(\vec{r},\vec{r'}) dS'$$

$$\mathcal{L}(\vec{J};\vec{r}) = jk_0 \int_{\sum_R} [\vec{J}(\vec{r'}) + \tfrac{1}{k_0^2} \nabla\nabla'_S . \vec{J}(\vec{r'})] g(\vec{r},\vec{r'}) dS'$$

$$g(\vec{r},\vec{r'}) = \frac{e^{-jk_0|\vec{r}-\vec{r'}|}}{4\pi|\vec{r}-\vec{r'}|} \tag{2.2}$$

where $\eta_0 = \sqrt{\mu_0/\epsilon_0}$, $k_0 = \omega\sqrt{\mu_0\epsilon_0}$, ∇'_S is the surface divergence operator and $\sum_R$ is the reconstruction surface. The source plane is discretised to flat triangular patches. The same BFs and, thus, the same number of unknowns are used to represent electric and magnetic currents

$$\vec{J} = \sum_{n=1}^{N} c_n^J \vec{F}_n, \quad \vec{M} = \eta_0 \sum_{n=1}^{N} c_n^M \vec{F}_n \tag{2.3}$$

In (2.3), the coefficients are normalized to η_0 to have consistent physical dimensions and prevent bad matrix conditioning. This normalisation is done in the literature [21] for all MoM problems, which require electric and magnetic currents interaction. As a result, we have the linear system below:

$$\eta_0 \begin{bmatrix} \mathcal{K}_{MR} & -\mathcal{L}_{MR} \end{bmatrix} \begin{bmatrix} c^J \\ c^M \end{bmatrix} = \begin{bmatrix} H \end{bmatrix} \tag{2.4}$$

where $\mathcal{K}_{MR}$ and $\mathcal{L}_{MR}$ are defined between the points on the measurement plane, $\sum_M$, and the points on the source surface, $\sum_R$. To form these integral equations, MoM and LCN can be used, each of which is elaborated thoroughly in the next sections, and then the proposed method in this chapter that combines the benefits of the two aforementioned techniques is explained.

2.2.1 Locally Corrected Nyström method

The LCN formulation of our problem is developed in this section. It includes LCN formulation of EFIE for both magnetic and electric currents. The essence of Nyström method is that the intended surface (source plane in an antenna problem and surface of the scatterer in the scattering problems) is discretised to N patches, and an appropriate quadrature rule is applied to each cell to calculate the integral equation. So far, the Nyström method is always

used for scattering problems in which the integral equation

$$\phi(r) = \int_S C(r, r')J(r')dS' \tag{2.5}$$

can be employed to find current distribution on surface S where $C(r, r')$ and ϕ are known functions. To calculate (2.3) using a quadrature rule, we divide S to N_p patches and use N_q quadrature points

$$\phi(r_{qm}) = \sum_{p=1}^{N_p} \sum_{q=1}^{N_q} \omega_{qp} C(r_{qm}, r_{qp}) J(r_{qp}) \tag{2.6}$$

where r_{qm} and r_{qp} are at the abscissas of the qth quadrature point on the observation patch m and source patch p, respectively. The weights ω_{qp} are the ones directly obtained from regular quadrature rules, such as Gauss–Legendre. Such weights can be calculated analytically once and stored in a lookup table and used later. For this application instead of (2.5) and (2.6), we have

$$\int_{cell\ n} J(t')C(t_m, t')dt' = \sum_{i=1}^{q} \omega_{ni} J(t_{ni}) C(t_m, t_{ni})) \tag{2.7}$$

When the source and the observation points are in close proximity, the original idea is to synthesise a new quadrature rule. An equivalent approach is to synthesise a new smooth kernel to be sampled by the original quadrature rule for the near-field interactions. The 'locally corrected' quadrature rule is employed to better deal with either weak or strong singularities in the kernel of the integral equations and accurately discretise the integral operators. In the context of LCN, the near-field denotes situations where the local correction is required. In other words, a set of basis polynomials are used as a weight function for the singular kernel to calculate the integral to a desired precision. This is when the source and measurement points are close together and regular weights are inadequate to estimate the non-smooth kernel. When the measurement and the source points are far apart, weights are easily obtained using (2.7). Generally, the idea is to use the Nyström method when

the separation between the q_m, a measuremnt point, and q_p, a point on the reconstruction surface, is so large that the kernel is smooth (far), and to use LCN to deal with the singular behavior of the kernel for the near source and observation points (near)

$$\phi(r_{qm}) = \sum_{p \in far} \sum_{q=1}^{N_q} \omega_{qp} C(r_{qm}, r_{qp}) J(r_{qp}) + \sum_{p \in near} \sum_{q=1}^{N_q} \tilde{\omega}_{qp} C(r_{qm}, r_{qp}) J(r_{qp}) \tag{2.8}$$

where $\{near\} \cup \{far\} = \{1, \ldots, N_p\}$ and ω_{qp} and $\tilde{\omega}_q p$ are the regular and locally corrected weights. It is practicable to build the LCN matrix using only the near-field weights. Although this increases the fill time of the matrix, one does not need to discriminate between near-field and far-field regions. In LCN, the original discretisation of the integral operator (2.7) is replaced with another approximation (2.7), in which L is the new 'corrected' kernel and must be calculated at the required samples (since only locally corrected weights are used in this study, we use ω_{qp} for simplicity):

$$\int_{cell\ n} J(t') C(t_m, t') dt' = \sum_{i=1}^{q} \omega_{ni} J(t_{ni}) L(t_m, t_{ni})) \tag{2.9}$$

For this purpose, we presume a set of BFs $\{F_k(t)\}$ to model the current distribution. Then, L is obtained in a way that the near fields of this current distribution are correct at the necessary sample points:

$$\sum_{i=1}^{q} \omega_{ni} F_k(t_{ni}) L(t_m, t_{ni}) = \sum_{i=1}^{q} F_k(t_{ni}) \{\omega_{ni} L(t_m, t_{ni})\} \cong \int_{cell\ n} F_k(t') C(t_m, t') dt' \tag{2.10}$$

If there are q sample points for the quadrature rule and q BFs, this results in the square system of (2.10). Here, we use a three-point Gauss–Legendre quadrature rule to establish an equivalent relationship between RWG MoM and LCN method. By solving this equation, the numerical values of $L(t_m, t_{n1})$ through $L(t_m, t_{ni})$ are obtained for each measurement point in

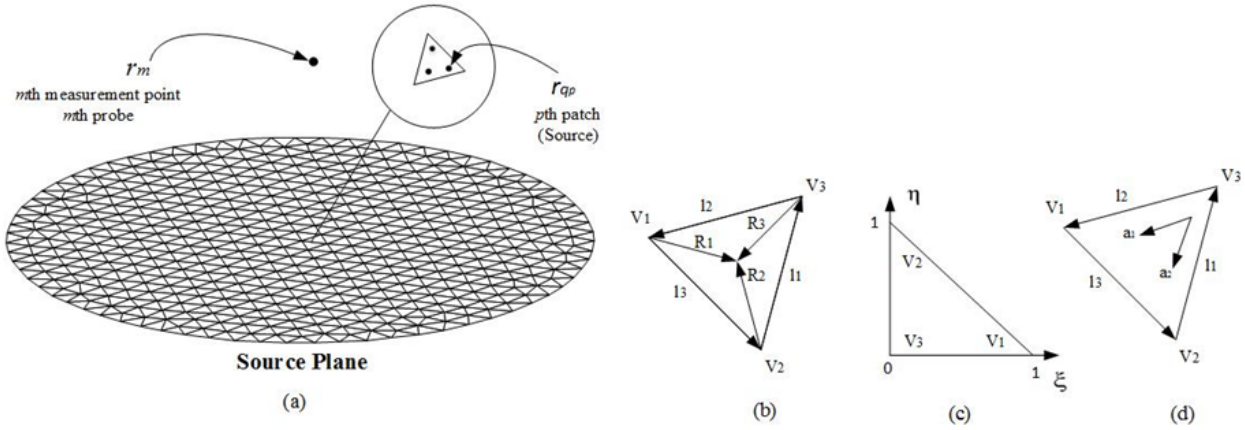

Fig. 2.3: Point-based discretization of the source plane, (a) Uniform discretization of the source plane using triangular flat patches, (b) Ramp functions (half RWG basis functions), (c) Barycentric triangle, (d) Covariant unitary vectors on a flat triangular patch [20]

the near-field of cell n. For any current density, which can be represented adequately by the BFs, applying synthesised L values should lead to the accurate near-fields:

$$\begin{pmatrix} F_1(t_{n_1}) & F_1(t_{n_2}) & \dots & F_1(t_{n_q}) \\ F_2(t_{n_1}) & F_2(t_{n_2}) & \dots & F_2(t_{n_q}) \\ \vdots & \vdots & & \vdots \\ F_q(t_{n_1}) & F_q(t_{n_2}) & \dots & F_q(t_{n_q}) \end{pmatrix} \begin{pmatrix} \omega_{n1} L(t_m, t_{n1}) \\ \omega_{n2} L(t_m, t_{n2}) \\ \vdots \\ \omega_{nq} L(t_m, t_{nq}) \end{pmatrix} = \begin{pmatrix} \int_{cell\ n} F_1(t') C(t_m, t') dt' \\ \int_{cell\ n} F_2(t') C(t_m, t') dt' \\ \vdots \\ \int_{cell\ n} F_q(t') C(t_m, t') dt' \end{pmatrix} \tag{2.11}$$

J and M over each triangular patch are defined in a 2D space η, ζ and over a_1 and a_2, which are unitary vectors tangential to the source plane as defined in [19]

$$a_1 = \frac{\partial r}{\partial \zeta}, \quad a_2 = \frac{\partial r}{\partial \eta} \tag{2.12}$$

as shown in Fig. 2.3 for each quadrature point, $(x(j), y(j))$, in a patch, η and ζ are

$$\zeta = (\frac{1}{2A}((y_3 - y_1)(x(j) - x_1) - (x_3 - x_1)(y(j) - y_1)))$$
$$\eta = \frac{1}{2A}\begin{pmatrix} -(y_2 - y_1)(x(j) - x_1) \\ +(x_2 - x_1)(y(j) - y_1) \end{pmatrix} \tag{2.13}$$

Thus, J and M are

$$J = J^1(r')a_1^p + J^2(r')a_2^p$$
$$M = M^1(r')a_1^p + M^2(r')a_2^p \tag{2.14}$$

where a_1^p and a_2^p are defined on the pth patch. In the LCN method, these currents are divided by the Jacobian, but in this study, since in the barycentric coordinate system the Jacobian is constant and is two times that of the triangle area, it is eliminated from the notation [26]. Since in the near-field measurement the source and measurement plane are very close, a fixed quadrature rule is not an accurate approximation for the integral equations. To avoid this imprecision and effectively estimate the singular integrals, the LCN method with a set of BFs is used to locally correct the q point quadrature rule. The same BFs are used for both magnetic and electric currents:

$$J_k^j(r) = F_k(r)a_j, \quad M_k^j(r) = F_k(r)a_j \tag{2.15}$$

Various BFs can be defined, but in order to establish a relationship with RWG ones, we use $F_1(r) = 1$, $F_2(r) = \zeta(r)$ and $F_3(r) = \eta(r)$, [19], and [20]. Therefore, for the LCN approach, we have

$$\sum_{q_p}^{3} \tilde{\omega}_{mq_p}^{ij} F_{k'}(r_{q_p}) = \int_{S_p} \bar{G}(r_m, r').J_{k'}^j(r')ds'$$
$$\sum_{q_p}^{3} \tilde{\omega}_{mq_p}^{ij} F_{k'}(r_{q_p}) = \int_{S_p} \bar{G}(r_m, r').M_{k'}^j(r')ds' \tag{2.16}$$

$$[L].[\tilde{\omega}^{ij}] = [\tilde{c}^j]^T \tag{2.17}$$

where G is $\nabla g(r, r')$ in (2.15), and $g(r, r')$ in (2.16), 'T' indicates transposition, and $[L]$ is a (3×3) Vandermonde matrix

$$[L] = \begin{pmatrix} 1 & 1 & 1 \\ \zeta(r_1) & \zeta(r_2) & \zeta(r_3) \\ \eta(r_1) & \eta(r_2) & \eta(r_3) \end{pmatrix} \tag{2.18}$$

and matrix $[\tilde{c}^j]$

$$[\tilde{c}^j]_{m,k'} = \int_{S_p} \bar{G}(r_m, r').J^j_{k'}(r')ds' \tag{2.19}$$

$$[\tilde{c}^j]_{m,k'} = \int_{S_p} \bar{G}(r_m, r').M^j_{k'}(r')ds' \tag{2.20}$$

The discretised EFIE is a linear system of N_m equations (the number of measurement points) and $12N_p$ unknowns, since magnetic and electric currents on each patch are represented in terms of 6 unknowns, which in matrix form is

$$[Z_{LCN}].[b] = [H] \tag{2.21}$$

where $[H]$ and $[Z_{LCN}]$ are known and $[b]$ is the vector of the unknown coefficients, and still no current continuity is applied to $[Z_{LCN}]$. Although the significance of the current continuity recedes for high-order discretisation schemes, it has a radical impact for lower orders such as the classical zeroth- and first-order MoM and LCN.

2.2.2 RWG MoM

When the surface is closed, as in [19], the current on the patch p can be expressed based on the ramp functions or 'half' RWG BFs as

$$J(r') = \sum_{k'=1}^{3} b^p_{k'} R^p_{k'}(r'), \quad r' \ in \ patch \ p \tag{2.22}$$

where R_1, R_2, and R_3 are ramp functions as shown in Fig.2.3. Afterward, unifier matrices along with coefficients $l/2A$ (where l is the length of the common edge between two adjacent triangles, and A is the area of each triangle) are used to preserve the continuity of the currents [19]. However, RWG BFs are defined based on the interior edges. Thus, when the surface is open like the source plane in our problem, (2.22) is no longer a suitable representation for current because there are some exterior edges as well. Instead, we have

$$J(r') = \sum_{k'=1}^{N_{E_i nt}} b_{k'} \begin{pmatrix} \int_{k'_1} (\frac{l_{k'}}{2A_{k'_1}}) R^n_{k'_1} C(r, r') ds' - \\ \int_{k'_2} (\frac{l_{k'}}{2A_{k'_2}}) R^n_{k'_2} C(r, r') ds' \end{pmatrix} \tag{2.23}$$

where $N_{E_{int}}$ is the number of interior edges which is equal to $1.5N_p$ for a closed network, as is explained in Section 3.1.4. $l_{k'}$ is the length of k'th interior edge which is shared between triangles 1 and 2 with areas $A_{k'_1}$ and $A_{k'_2}$. $R_{k'_1}$ and $R_{k'_2}$ are the ramp functions in triangles 1 and 2 that have a normal component to $l_{k'}$. Every integral on the right side of (2.23) can be approximated with a q-point quadrature rule ($q = 3$ in this work). Therefore, RWG MoM converts (2.5) to

$$\sum_{k'=1}^{N_{E_i nt}} b_{k'} \begin{pmatrix} \int_{k'_1} (\frac{l_{k'}}{2A_{k'_1}}) R^n_{k'_1} C(r, r') ds' - \\ \int_{k'_2} (\frac{l_{k'}}{2A_{k'_2}}) R^n_{k'_2} C(r, r') ds' \end{pmatrix} = \phi(r) \tag{2.24}$$

$C(r, r')$ is $\nabla g(r, r')$ in(2.15), and $g(r, r')$ in (2.16). In matrix form, we have

$$[Z].[b] = [V] \tag{2.25}$$

where $[V]$ and $[Z]$ are known matrices and $[b]$ denotes unknown coefficients. Current continuity is clearly enforced in this impedance matrix.

2.2.3 RWG via the first-order LCN

To enforce current continuity to the LCN method, initially we need to develop a relationship between the RWG basis function and the LCN ones. In [19], a similar relationship is developed for scattering problems. There are some differences between these two applications regarding the relationship between the RWG and LCN BFs. In this study, we are not able to use a ramp test function, and the current reconstruction surface is open. As explained in [19], ramp functions or half RWG BFs can be expressed in terms of $F_k(r)$ and a_i, as

$$\begin{aligned} R_1(r) &= \frac{l_1}{2A}[-F_1(r)a_1 + F_2(r)a_1 + F3(r)a_2] \\ R_2(r) &= \frac{l_2}{2A}[-F_1(r)a_2 + F_2(r)a_1 + F3(r)a_2] \\ R_3(r) &= \frac{l_3}{2A}[F_2(r)a_1 + F_3(r)a_2] \end{aligned} \tag{2.26}$$

and in matrix form of

$$[R_n] = [a_n].[F]^T.[\Psi_n] \tag{2.27}$$

where

$$[F] = \begin{pmatrix} [L] & [0] \\ [0] & [L] \end{pmatrix} \tag{2.28}$$

$$[\Psi_n] = \begin{pmatrix} -1 & 0 & 0 \\ 1 & 1 & 1 \\ 0 & 0 & 0 \\ 0 & -1 & 0 \\ 0 & 0 & 0 \\ 1 & 1 & 1 \end{pmatrix} \begin{pmatrix} \frac{l_1}{2A} & 0 & 0 \\ 0 & \frac{l_2}{2A} & 0 \\ 0 & 0 & \frac{l_3}{2A} \end{pmatrix} \tag{2.29}$$

so far the LCN basis functions are converted to the ramp functions, and there is no current continuity between adjacent cells.

$$[a_n] = [[a_1^n][a_2^n]], \quad [a_i^n] = \begin{pmatrix} a_i & 0 & 0 \\ 0 & a_i & 0 \\ 0 & 0 & a_i \end{pmatrix} \tag{2.30}$$

The reciprocal unitary vectors are defined as follows:

$$a^1 = a_2 \times \hat{n}, \quad a^2 = \hat{n} \times a_1, \quad a_n^i . a_j^n = \delta ij \tag{2.31}$$

where δ_{ij} is the Kronecker–Delta [19]. Now, we have $[\alpha_n]$ matrix which is defined on patch n:

$$[I_6] = [\alpha_n]^T [a_n] \tag{2.32}$$

$[I_6]$ is the (6×6) identity matrix that shows the relation between the unitary vectors and reciprocal unitary vectors.

$$[\alpha_n] = [[diag(a_n^1)][diag(a_n^2)]] \tag{2.33}$$

Therefore, $[Z_{LCN}].[\alpha_p].[R_p]^T = [Z_{LCN}].[\Re]^T$ converts the LCN impedance matrix to a new one which is based on three ramp functions inside of each triangle. Here, $[\Re]^T$ is a $(6N_p \times 3N_p)$

$$[\Re]^T = \begin{pmatrix} [\Re_1^1] & [0] & ... & [0] \\ [0] & [\Re_2^1] & ... & [0] \\ \vdots & \vdots & \ddots & \vdots \\ [0] & [0] & ... & [\Re_{N_p}^1] \\ [\Re_1^2] & [0] & ... & [0] \\ [0] & [\Re_2^2] & ... & [0] \\ \vdots & \vdots & \ddots & \vdots \\ [0] & [0] & ... & [\Re_{N_p}^2] \end{pmatrix} \tag{2.34}$$

In (2.34), every [0] is a matrix of (3×3) zeros, and every $\Re_n^i$ is a (3×3) matrix over patch n, for the ith unitary vector. Each entry is $[\Re_n^i]_{q_n,k} = a_n^i.R_k^n(r_{q_n})$. Now, to enforce current continuity between adjacent patches, a unifier matrix, $[u]$, is used, which is different from the one mentioned in [19]. The dimension of this matrix is $3N_p \times N_{E_{int}}$. In each column of this matrix, all entries except two of them are zero. These two nonzero elements are 1 and -1 to preserve current continuity along the normal component of the ramp functions in two triangular patches which share an edge. Thus, we have the conversion from LCN impedance to an RWG one in matrix form

$$[Z_{RWG}] = [Z_{LCN}].[\Re]^T.[u] \tag{2.35}$$

where $[\Re]^T$ converts LCN basis functions to ramp functions along with the $\frac{l_k}{2A_k}$, and $[u]$, the unifier matrice, applies the last step to have current continuity over the common edges. The relationship in (2.35) is for just the integrals and kernels in (2.15) and (2.16). Since the triangular patches are flat, the singularity order of the first term of the L kernel on the right-hand side of (2.2) is in the order of $O(1/R)$ and can be evaluated up to an acceptable accuracy analytically, but for the second term we use vector identity to convert it to ([19])

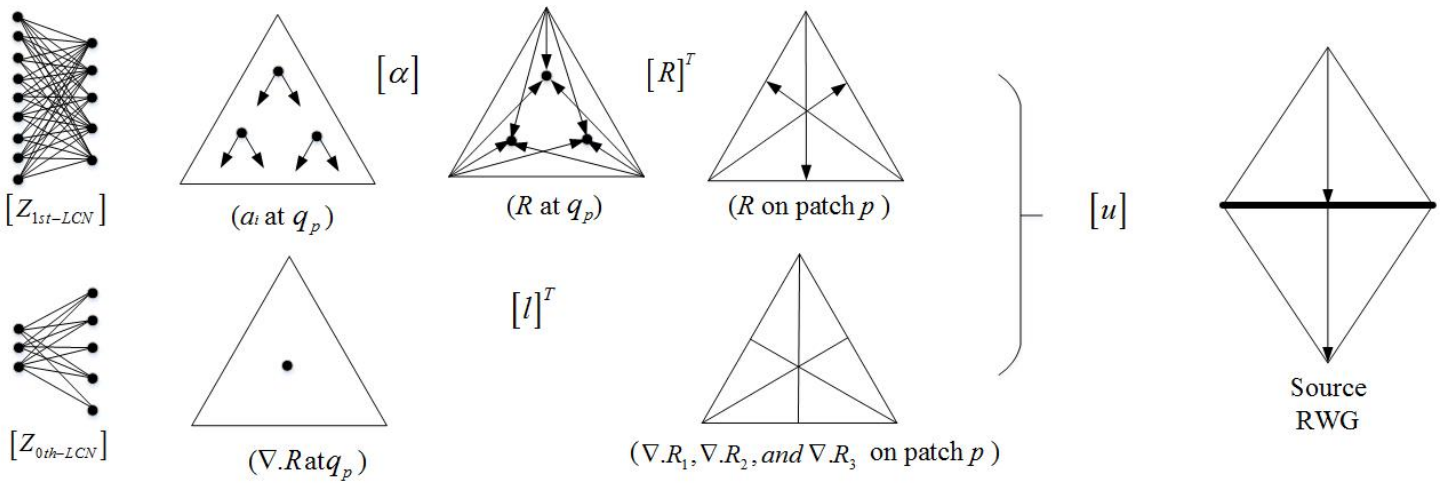

Fig. 2.4: Conversion from LCN to RWG impedance matrix. From right to left, in the top row, $[\alpha]$ converts LCN basis functions at each quadrature point to ramp functions, and $[R]^T$ translates ramp functions at all points to three main R_1, R_2, and R_3. In the second row, $[l]^T$ converts the $\nabla.R$ from LCN system to $\nabla.R_1$, $\nabla.R_2$, and $\nabla.R_3$ in RWG MoM. $[u]$ finally enforce current continuity between adjacent triangles.

$$\nabla \int_{S_p} \nabla G(r_m, r').M^j_{k'} dS' = \int_{S_p} \nabla G(r_m, r')[\nabla'_{||}.M^j_{k'}]dS' - \oint_{C_p} [\hat{e}'_p.M^j_{k'}(r')][\nabla G(r_m, r')]dl \tag{2.36}$$

S_p is the surface of one patch, C_p is the counter around S_p, and $\hat{e}^p$ is an outward unitary vector which is normal to C_p and tangential to S_p. The second term in (2.36) is numerically equal to zero for RWG MoM and RWG-via-LCN method because the current distribution is normal to $\hat{e}^p$ on two edges and for the third edge, the contribution of two adjacent triangles is equal with opposite signs. Finally, the linear integral vanishes, which in LCN needs to be calculated numerically, causing some error.

For the second term in kernel L, we have divergence of the current, so to approximate this sentence; we use a zeroth-order LCN. The divergence of Ramp functions is l/A, so the kernel we assume for this term is

$$C(r, r') = \frac{j\eta_0}{k_0 A^p} \nabla g(r, r')) \tag{2.37}$$

Therefore, eventually to convert the L kernel from LCN to RWG (Fig.2.4), we have

$$[Z_{RWG}] = [Z_{RWG-via-LCN}] = [Z_{1st-LCN}].[\Re]^T.[u] + [Z_{0th-LCN}].[l]^T.[u] \tag{2.38}$$

where $[l]$ and $[Z_{0th-LCN}]$ are $3N_p \times N_p$ and $N_m \times N_p$ matrices

$$[l]^T = \begin{pmatrix} [l_1] & [0] & ... & [0] \\ [0] & [l_2] & ... & [0] \\ \vdots & \vdots & \ddots & \vdots \\ [0] & [0] & ... & [l_{N_p}] \end{pmatrix} \tag{2.39}$$

and every [0] is a matrix of (1×3) zeros. It worth noting that unlike the equations of scattering problems, here the system of equations is not square since the number of measurement points is much less than the unknown coefficients. Moreover, as shown in [21], in scattering problems if RWG test functions are used, the second term in (2.38) will be analytically zero because of the current continuity of RWG basis functions. Yet in near-field measurement applications it is not possible to use RWG basis functions as test functions for the measured data, and the numerical calculations of the integral equations will be more difficult.

2.2.4 Degrees of freedom (DOFs) and condition number of the impedance matrices

Assuming that E_{ext} and E_{int} represent the number of edges on the exterior and interior boundary of a surface and F denotes the number of patch faces, each triangle has three edges, and every internal edge contributes to the current distribution on two adjacent triangles while an external edge is associated with only one triangle [12]. Therefore, below we have the relation between E_{ext}, E_{int} and F

$$3F = 2E_{int} + E_{ext} \tag{2.40}$$

In RWG MoM, the number of the required DOFs is equal to E_{int}, whereas in LCN it is $6F$

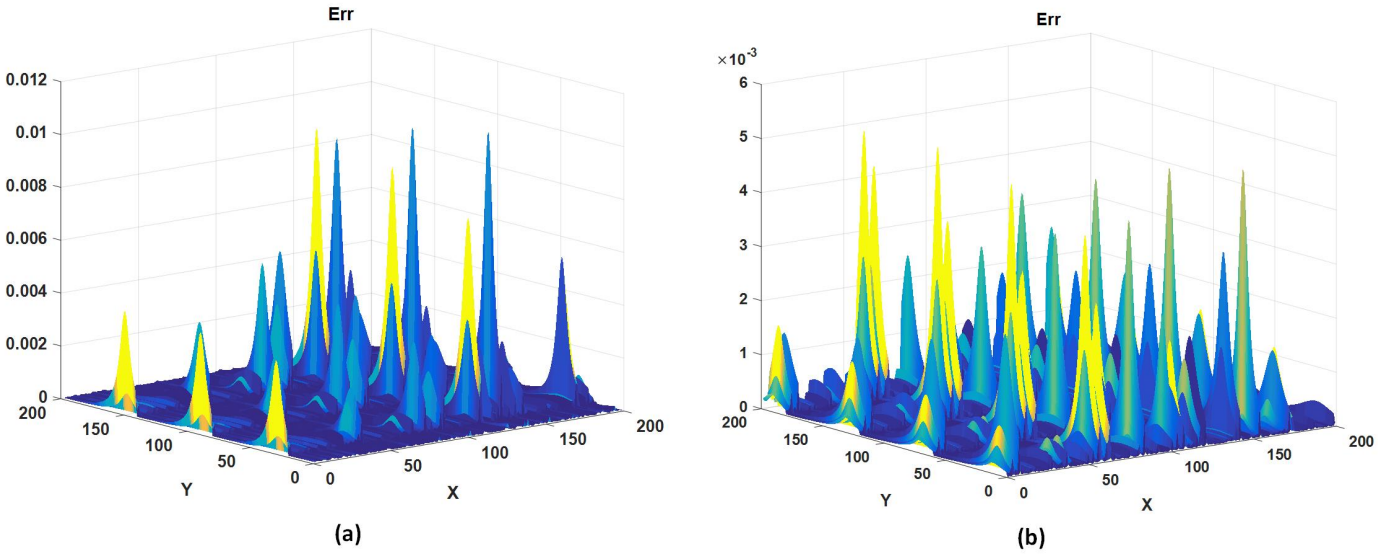

Fig. 2.5: Comparison of 200×200 samples of impedance matrices which obtained from RWG-via-LCN with RWG ones (a) For magnetic, (b) Electric currents. The error corresponds to $Z_{i,j} = |Z_{i,j}^{RWG} - Z_{i,j}^{RWG-via-LCN}|/|Z_{i,j}^{RWG}|$

.

(for each current, magnetic and electric current). Therefore, for closed surfaces ($E_{ext} = 0$) E_{int} is equal to $1.5F$, and for open ones it will be even less, which means a four times reduction in the number of DOFs, and consequently a faster solution due to problem size reduction. This also enhances the matrix condition number.

MLFMM has been widely used to accelerate numerical calculations, especially in scattering problems. In [13], it is mentioned that when this method is applied to a Galerkin-based MoM, its efficiency is limited by the size of a basis function. Generally, in MLFMM, near interactions are calculated exactly while for far interactions, multipole expansion of current distribution is used. Even if higher order BFs are utilised, the performance of MLFMM is limited by the more near interactions that need to be calculated and stored in the memory for each group.

In MLFMM, a big cube first encompasses the scatterer. This cube is then divided into eight smaller ones, and this procedure continues until the size of the smallest cube and, therefore, the size of the lowest level is several times larger than the longest mesh edge. For

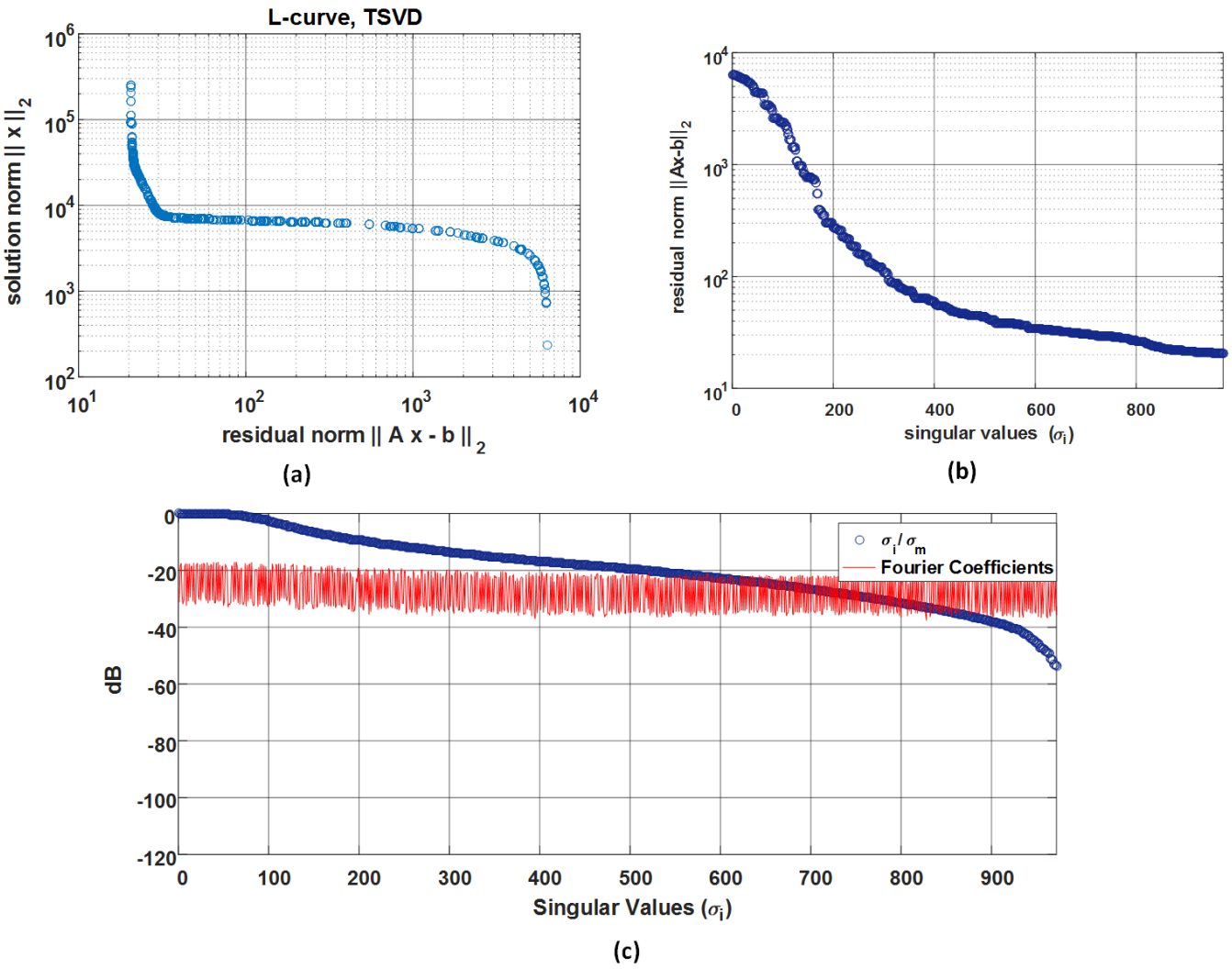

Fig. 2.6: TSVD regularization method to solve the inverse problem, (a) L-curve (a log–log plot of $\|x\|_2$versus $\|Ax-b\|_2$) or regularization (dipole antenna), (b) Residual norm versus the number of the singular values, (c) The singular values and Fourier coefficients versus the number of singular values

example, for an RWG basis function, the edge length is about 0.1λ; therefore, the smallest cube size is about a quarter of a wavelength. Also, fast multipole method (FMM) is used in near-field measurements to speed up the process [25]. As mentioned in [25], in MoM, for the finest level of FMM groups, the support of BFs is not small enough, so the BFs are subdivided into quadrature points, and the effect of quadrature points is collected. Thus, the point-based method such as LCN is more appropriate for acceleration by MLFMM than

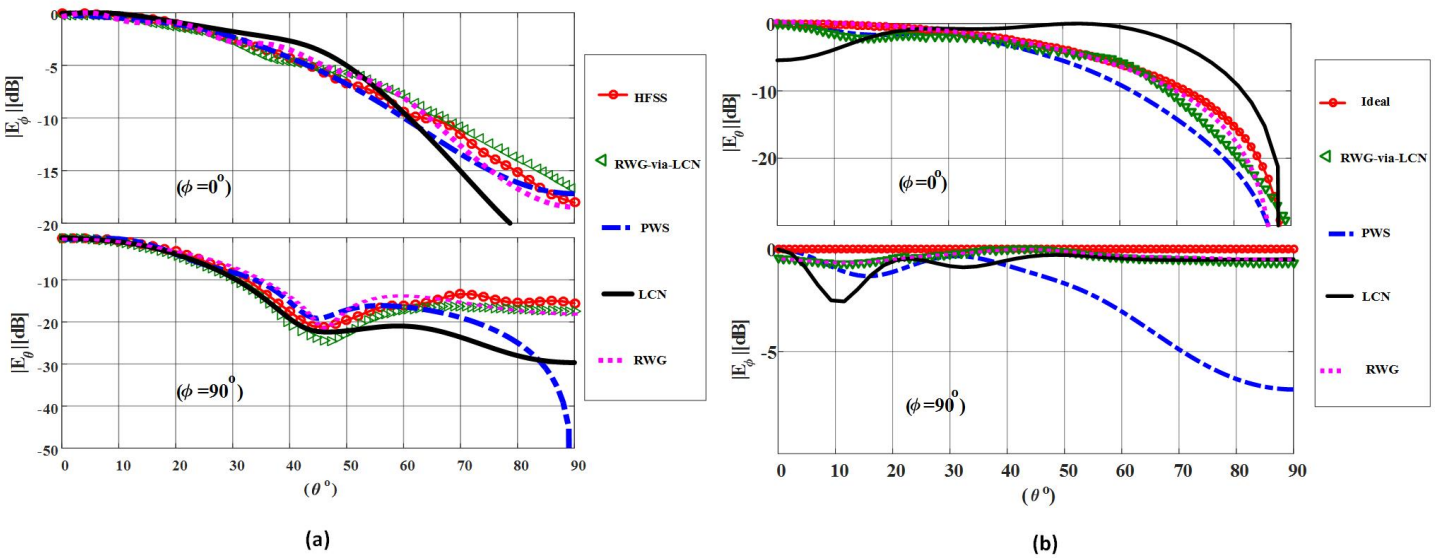

Fig. 2.7: Far-field pattern of two antennas obtained via different methods: HFSS, RWG-via-LCN, PWS, LCN and RWG, (a) Far-field pattern of an E-plane horn antenna, (b) Fasr-field pattern of an ideal dipole antenna.

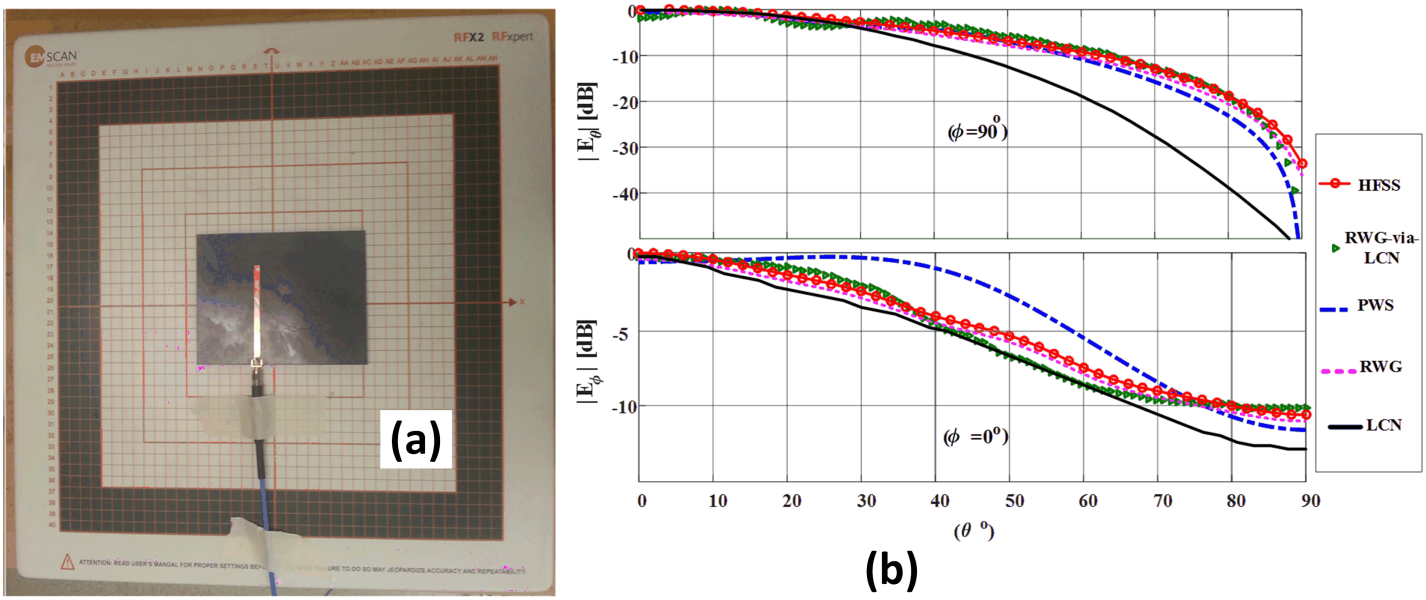

Fig. 2.8: Measurement setup and far-field pattern of Slot antenna, (a) Slot antenna on the RFX2, (b) far-field pattern of the slot antenna obtained via different methods: HFSS, RWG-via-LCN, PWS, LCN and RWG.

MoM method. The proposed method in this study combines this advantage of the LCN method with the benefit of current continuity of the RWG MoM.

Table 2.1: Comparison of DOFs for RWG-via-LCN and LCN methods for three antenna

Antenna	E-plane horn	Dipole	Slot
frequency	$1GHz$	$2.4GHz$	$2GHz$
N_p	1201	1532	1532
E_{int}	1762	2253	2253
RWG-via-LCN DOFs	1762	2253	2253
LCN DOFs	7206	9192	9192
unknown per square wavelength (RWG-via-LCN)	110	250	250
unknown per square wavelength (LCN)	450	1020	450

2.3 Measurement and numerical results

In Table 3.1, for three antennas, we compared LCN and RWG-viaLCN methods in terms of the required number of DOFs and unknowns per square wavelength to precisely model currents. Based on the presented values, in LCN we need more than four times of the number of DOFs compared to the RWG-via-LCN method and RWG MoM. Fewer DOFs result in the better conditioning of the impedance matrices. For instance, in the near-field measurement of the dipole antenna, our simulations showed that under the same parameters, the condition number of the impedance matrix is 5.1604×10^{11} and 6.8183×10^{18} in RWG-viaLCN and LCN, respectively. Therefore, in the proposed method, the condition number is reduced noticeably. To evaluate the accuracy of the proposed method, the impedance matrices obtained via this method are compared to those calculated by RWG MoM. The error is computed based on

$$Err(Z_{i,j}) = |Z_{i,j}^{RWG} - Z_{i,j}^{RWG-via-LCN}|/|Z_{i,j}^{RWG}| \tag{2.41}$$

The dimension of the matrices is 1600×1702. Since it is not possible to show all the components in the graph, only the part which includes the maximum amount of error is shown in Fig. 2.5. These impedance matrices are related to an E-plane horn antenna with 1GHz operating frequency. We have 40×40 samples on the measurement plane at the distance of 0.57λ above the surface of the antenna. The source plane which is 0.24λ above the antenna is a circle with 3λ radius. The source plane is assumed to be large enough

to contain all the significant components of the currents. Edge length is 0.1λ as it is the normal choice for RWG MoM. After the calculation of the impedance matrices using the MoM or Nyström method, we solve the inverse problem to find the current distribution. To do so, we need to solve an ill-posed problem. The SVD (singular value decomposition) of the impedance matrix is calculated, and TSVD method [26] in which the small singular values giving rise to difficulties are replaced with zero is used to regularize the problem. To determine the cutting threshold, the wellknown L-curve is used as shown in Fig. 2.6(a), for example, for the impedance matrix of the well known dipole antenna. Once we finds the residual norm at the corner of the L-curve, we can determine the corresponding singular value form Fig. 2.6(b). After the threshold as depicted in Fig. 2.6(c), the Fourier coefficients will be dominated by the inverse of small singular values and the accuracy of the results degrades. For iterative solvers such as MLFMM, it is not possible to use direct methods like TSVD. Usually, the preconditioners such as diagonal, block diagonal, and inverse LU preconditioners are employed. For most iterative linear solvers when the condition number decreases because of preconditioning, the rate of convergence increases [59]. The reconstructed currents are used to calculate fields at the measurement points. The error is computed using

$$Err = \frac{H^{ref} - H^{Numerical}}{H^{ref}} \tag{2.42}$$

H_{ref} is obtained from HFSS for the horn antenna, analytical formulas for the ideal dipole, and measurement for the slot antenna. The error for the horn antenna, ideal dipole, and the slot antenna is 0.5, 0.1 and 1%, respectively. Reconstructed currents are also used to calculate the far-field pattern of the antennas. For the dipole antenna with an operating frequency of 2.4GHz, the measurement plane is similarly 0.57λ above the antenna and consists of 40×40 measurement probes. A 2λ-radius source plane is 0.24λ above the antenna, so the distance between the source plane and the measurement plane is about 0.33λ (singularity starts in distances closer than 0.2λ). At this distance, we have reliable results for all our simulations. In Fig. 2.7, the measurement setup is shown. For the PWS method, antenna is placed exactly

on the RFX2, but for the RWG-via-LCN method, it is about 0.57λ above the probe array. In RFX2, there is 25mm between the surface of the scanner and probe array. The focus of the study is to establish a relation between RWG BFs and LCN ones to have a point-based method and at the same time current continuity between adjacent patches. Once this relation is developed, any singularity extraction or cancellation that can be applied to RWG basis function, can be applied to LCN one as well. Far-field patterns are shown in Figs. 2.7 and 2.8. While PWS and LCN are not capable of reconstructing far-field precisely, the results which are obtained using RWG MoM and LCN-via-RWG are close to HFSS and analytical solutions. This shows how much current continuity can affect accuracy when we have low-order methods such as RWG MoM, zeroth- , and first-order LCN method.

2.4 Conclusion

In this chapter source reconstruction method is used to calculate the equivalent currents on a closed surface the encloses the antenna under test by having the palanar near-field measured data. The measured data are linked to the equivalent sources through electric field integral equations. Integral equations can be discretized using point-based or basis-based methods. To accelerate calculation of these equations one can apply MLFMM algorithm for which point-based methods are more appropriate. Thus LCN method which is a point-based technique is a better candidate for the applications where providing real-time results is critical. The main deficiency of LCN is that it does not retain current continuity across element boundaries.

In this chapter, for the first time, LCN along with Gauss-Legendre quadrature weight functions are utilized to discretize integral equations, and find equivalent currents by having measured near-fields. So far, this method is used only in scattering applications to calculate the induced current on surfaces of scatterers. Furthermore, in this chapterr, a relationship between RWG MoM and LCN is developed to enforce current continuity. The relationships between RWG, zeroth and, first-order LCN is extended to the application of very-near-field measurement and current reconstruction to preserve current continuity. The results of the proposed method are more accurate compared to LCN. Moreover, the required DOFs are even less than the quarter of the amount we need in LCN, which results in faster solutions and better conditioning of the impedance matrices. This method, which is a point-based method, is more suitable for acceleration with fast algorithms such as MLFMM and, thus, realtime applications. For verification purposes, the algorithm is applied to the near-field data of a slot antenna which are acquired using RFX2 tool. Then, the results are compared to ones which are computed using ANSYS HFSS software or PWS approach. There is a good agreement between RWG MoM and RWG-via-LCN method results.

Chapter 3

Detection of the Defective Vias in SIW Circuits from Single/Array Probe(s) Data Using Source Reconstruction Method and Machine Learning

3.1 Introduction

In this chapter, source reconstruction and machine learning algorithm are used to detect and classify different radiation sources in SIW circuits. one of the objectives of this chapter is to develope a source reconstruction method to detect the defective vias in SIW structures. To the best of the author's knowledge, the defective vias have not so far been detected based on source reconstruction method or any technique that relies on the electromagnetic emissions of the board. Further, the proposed method in this chapter uses the measured near-field to calculate the equivalent currents on the surface of the volume that encloses the SIW structure. Unlike other diagnostic tests that rely on the reconstructed currents, the near-field in this method is calculated at close distance from the board using the equivalent sources. Since the problem is ill-posed, our solution results in higher accuracy that is important in detecting small features such as defective vias. A new model is also proposed for the defective vias based on the apertures. In this model, if the center to center distance of two adjacent vias is small compared to the wavelength, the current distribution over two vias

can be assumed uniform and the same. Thus, the distance at which two adjacent defective vias can be resolved is obtained analytically. This approach can be integrated into the near-field measurement software and let the user know at what distance from the board the fields should be reconstructed to be able to detect the defective vias. Another aim of this chapter is to propose a machine learning algorithm that uses field and material variation to distinguish different radiation sources. Lastly, the validity and accuracy of the methods are confirmed using full-wave simulations, single probe, and electronically switched probe array measurements. It is shown that although for antenna and some circuits the radiation from a ground plane under the probe array is a limitation that needs to be considered, it is not an issue in SIW passive circuit tests since the resonant field decreases very rapidly around the vias.

This chapter is organized as follows. In section 3.1, the approach used to estimate the current distribution on a SIW structure is described. Then the optimum parameters for the near-field measurement, including the measurement height, the scanning area, and resolution (sampling space) are discussed by introducing the correlation coefficient and the condition number of the impedance matrix and performing some parametric study for a simple SIW transmission line (TL). Also, the field and material variation calculations are explained. Then a model is proposed for the electromagnetic behavior of the defective vias in a SIW structure in free space and close to a finite ground plane based on the apertures and patch antennas. In section 3.2, the experimental setup and the measurement and simulation results are presented to validate the proposed method. Investigations on a dual-mode filter and coupler show that such a near-field approach can be used effectively to detect the defective vias in SIW structures.

3.2 The Proposed Method

All of the steps in the proposed method are depicted in Fig.3.1. The proposed method includes two main processes, namely, simulation and measurement. In the simulation process,

the DUT is modeled in a full wave simulator with and without the finite ground plane (There is a ground plane beneath the probe array in RFX2 that is explained in section 3.2.4). In the measurement process, the very near-field (VNF) data of the SIW structure are measured using a single probe and a RFX2 probe array. Thereafter, the results of the single probe measurement and those of the simulation without the ground plane can be compared. Similarly, the results of the probe array measurement and those of the simulation with the ground plane are compared as well.

In what follows, the source reconstruction method that is used to calculate the equivalent currents on the surface of the DUT is explained in part 3.2.1. In part 3.2.2, the formulation of the field and material variation is presented. Also, the electromagnetic behavior of the defective vias radiation is modeled based on apertures and patch antennas in parts 3.2.3 and 3.2.4, respectively. Finally, the experimental setup and the measurement and simulation

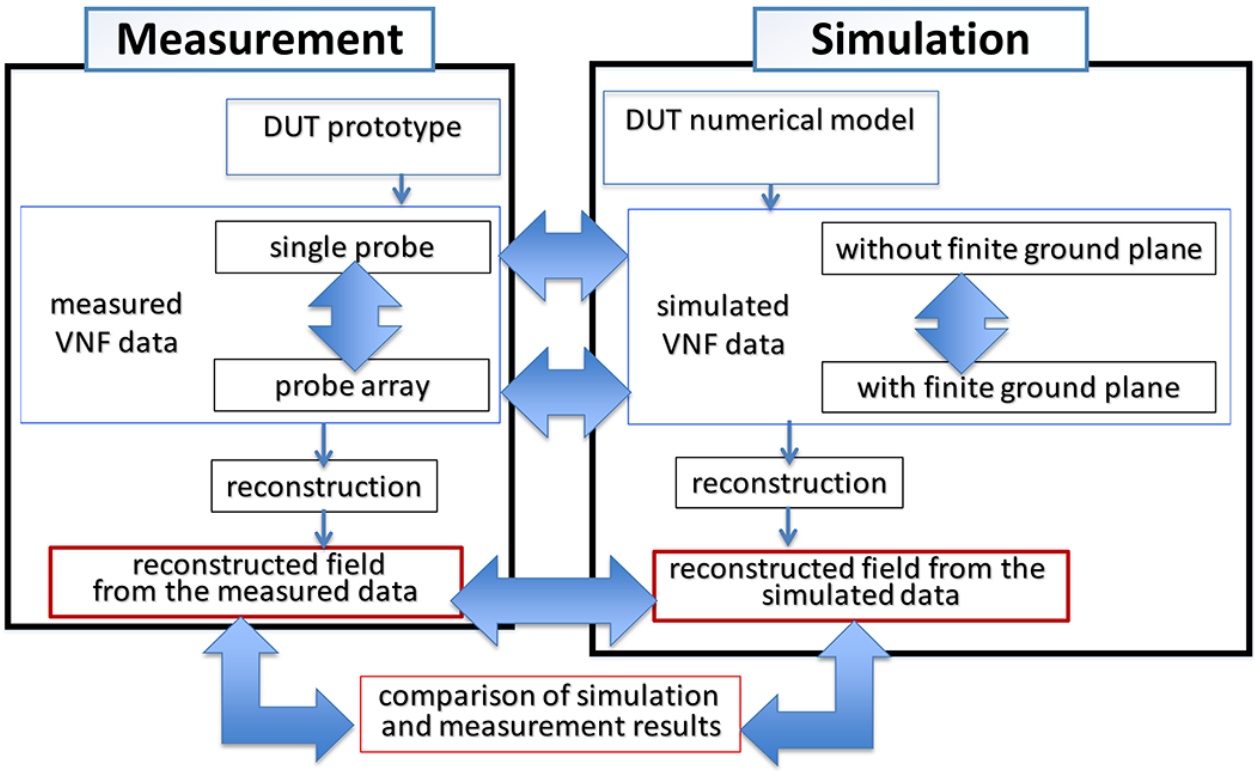

Fig. 3.1: Flow-chart for the comparison of results obtained by different measurement and simulation scenarios.

results are presented in section 3.3.

3.2.1 Source reconstruction method

The source reconstruction method is applied to reconstruct the currents on the surface of the box which encloses the SIW structure. Fig. 3.2. shows a schematic representation of the measurement system used in this study. The tangential component of the magnetic fields (amplitude and phase) parallel to the board surface are measured on the measurement plane ($\sum_M$). These measured data are linked to the equivalent electric, $\vec{J}$, and magnetic, $\vec{M}$, sources on the box surface via electric field integral equations (EFIE) [8] and [58]

$$\vec{E}(\vec{r}) = \mathcal{K}(\vec{M};\vec{r}) - \eta_0 \mathcal{L}(\vec{J};\vec{r}) \tag{3.1}$$

where

$$\mathcal{K}(\vec{M};\vec{r}) = \int_{\sum_R} \vec{M}(\vec{r'}) \times \nabla g(\vec{r},\vec{r'}) dS'$$

$$\mathcal{L}(\vec{J};\vec{r}) = jk_0 \int_{\sum_R} [\vec{J}(\vec{r'}) + \tfrac{1}{k_0^2} \nabla \nabla'_S . \vec{J}(\vec{r'})] g(\vec{r},\vec{r'}) dS'$$

$$g(\vec{r},\vec{r'}) = \frac{e^{-jk_0|\vec{r}-\vec{r'}|}}{4\pi|\vec{r}-\vec{r'}|} \tag{3.2}$$

where $\eta_0 = \sqrt{\mu_0/\epsilon_0}$, $k_0 = \omega\sqrt{\mu_0\epsilon_0}$ and ∇'_S is the surface divergence operator. In [8], it is mentioned that to have the reconstructed equivalent currents consistent with Maxwell's equations and enforce Love's equivalence theorem, a boundary condition of zero tangential electric and magnetic field is required. The equivalent boundary condition can be written as

$$\hat{n} \times [-\eta_0 \mathcal{L}(\vec{J};\vec{r}) + \mathcal{K}(\vec{M};\vec{r})] = -\frac{1}{2}\vec{M}(\vec{r}) \tag{3.3}$$

The classical jump condition can be used to avoid the inaccuracy of the second kind integral

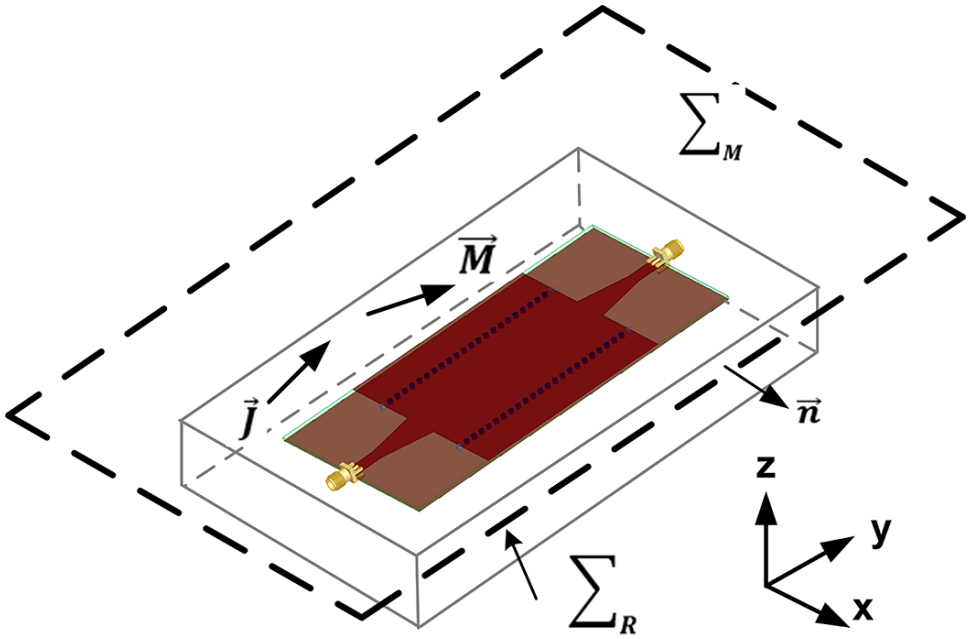

Fig. 3.2: An illustration of the source reconstruction method over a box which encloses the SIW structure ($\sum_R$). The tangential components of $\vec{H}$ field are measured on plane ($\sum_M$).

equation. Thus, the integral equation in (3.3) can be written as,

$$\lim_{r \to \sum_R^-} \hat{n} \times [-\eta_0 \mathcal{L}(\vec{J}; \vec{r}) + \mathcal{K}(\vec{M}; \vec{r})] = 0 \tag{3.4}$$

that is a first kind integral equation and means the tangential electric field should become zero by moving toward the interior of the volume enclosed by the fictitious surface. The surface of the box is discretized to flat triangular patches. Rao-Wilton-Glisson (RWG) basis functions (F_n) are utilized to represent electric and magnetic currents [48]

$$\vec{J} = \sum_{n=1}^{N} c_n^J \vec{F}_n, \quad \vec{M} = \eta_0 \sum_{n=1}^{N} c_n^M \vec{F}_n \tag{3.5}$$

where c_ns are the unknown coefficients. Equation (3.1) forces all the equivalent currents to radiate the same field as the measured ones on the measurement plane, and the test functions are not required. Yet for equation (3.4), test functions are to be used to improve accuracy. Here point-matched and RWG tested fields for measured and boundary conditioned values are

used, respectively. Hence, for each operator two discretization schemes are needed. By means of the continuity of the normal components on the shared edge for RWG basis functions, the operators $\mathcal{L}$ and $\mathcal{K}$ can be written as [58],

$$\begin{aligned}\mathcal{L}^1_{m,n} &= jk_0 \int_{S_m} dr \vec{f}_m(r). \int_{S_n} dr' g(\vec{r},\vec{r'}) \vec{f}_n(r) \\ &\quad - \frac{j}{k_0} \int_{S_m} dr \nabla . \vec{f}_m(r). \int_{S_n} dr' g(\vec{r},\vec{r'}) \nabla' \vec{f}_n(r)\end{aligned} \tag{3.6a}$$

$$\mathcal{L}^2_{m,n} = [jk_0 \int_{S_n} [\vec{J}(\vec{r'}) + \frac{1}{k_0^2} \nabla \nabla'_S . \vec{J}(\vec{r'})] g(\vec{r},\vec{r'}) dS]_{(r \to r_m)} . \hat{a_m} \tag{3.6b}$$

$$\mathcal{K}^1_{m,n} = jk_0 \int_{S_m} dr \vec{f}_m(r). \int_{S_n} dr' [\vec{f}_n(r) \times \nabla' g(\vec{r},\vec{r'})] \tag{3.6c}$$

$$\mathcal{K}^2_{m,n} = jk_0 [\int_{S_n} dr' \vec{f}_n(r) \times \nabla' g(\vec{r},\vec{r'})]_{(r \to r_m)} . \hat{a_m} \tag{3.6d}$$

where m and n denote the mth row and the nth column, respectively, in the impedance matrix, and $\hat{a}_m$ is the unit tangential vector in the measurement plane that is $\hat{a}_x$ or $\hat{a}_y$ in case of the planar measurement. S_m and S_n are the source and test triangles, respectively, and r_m is the measurement point.

In (3.6b) and (3.6c), the cross product is taken out of the inner integral to facilitate the integration process. In case of any overlap between the source and observation triangles, both the inner and outer integrals are singular [60]- [63]. The singular part of the inner integral is extracted and calculated using analytical formulas, and the non-singular part is computed by an adaptive quadrature method [58].

If an edge is shared between the inner and outer integrals, the inner integral is singular over that edge. For the $\mathcal{L}$ operator, the singularity is resolved by taking the gradient operator out of the inner integral [60], and for the $\mathcal{K}$ operator, since the singularity is a logarithmic one, it is solved simply by an adaptive quadrature method, [60] and [63]. Finally, the system of equation can be summarized as:

$$\eta_0 \begin{bmatrix} \mathcal{K}_{MR} & -\mathcal{L}_{MR} \\ \mathcal{K}_{RR^-} & -\mathcal{L}_{RR^-} \end{bmatrix} \begin{bmatrix} c^J \\ c^M \end{bmatrix} = \begin{bmatrix} H \\ 0 \end{bmatrix} \tag{3.7}$$

H indicates the tangential magnetic field components on $\sum_M$. As it is demonstrated in Fig. 3.3, close to the position of the defective vias, there are some magnetic field radiations on the measurement plane. Thus, in MoM, on the surface of the box, refined meshes are used to have more accurate representation of the currents close to the high-level radiation areas. Gmsh mesh generator is utilized for mesh refinement [64]. The equation (3.7) can be rewritten in a compact form as

$$AX = H \tag{3.8}$$

where A is the impedance matrix and X is the vector of the unknown magnetic and electric current coefficients [48]. For most source reconstruction problems, the matrix A is ill-conditioned. Here, (3.8) is solved by the Tikhonov regularization method. The cost function is defined as below

$$F = ||H - AX||^2 + \alpha^2 ||X||^2 \tag{3.9}$$

where $||.||$ indicates the Euclidean norm and α is the regularization parameter that is determined by the L-curve method.

In simulations and measurements, some parameters impact the results. These factors are mesh size, scanning area, height, and resolution. These parameters and their impact are investigated below.

As a first test case, a SIW TL with two defective vias is considered. The operating frequency is 3GHz. The magnetic field is collected across a plane at the distance of 3mm from the sample. The size of the scan plane is 1.2 times that of the board, and the scanning resolution is 1.5mm (It is worth noting that 1.5mm is the scanning or sampling resolution not the resolution of the equivalent current reconstruction).

In the absence of noise, a high resolution scanned data guarantees that there is enough information in the measured near-field. As shown in [46] and [6], the scanning resolution must satisfy (3.10)

$$\Delta x, \Delta y \leq \frac{\lambda}{2\sqrt{1+(\frac{\lambda}{h})^2}} \tag{3.10}$$

where h is the separation distance between the DUT and the probe, and λ is the wavelength. Thus, for the frequency 3GHz ($\lambda = 10cm$) and $h = 3mm$, $\Delta x = \Delta y = 1.5mm$ is reasonable. The correlation coefficient γ between the reconstructed near-field results given by equivalent source simulation and full wave simulation is defined as follows:

$$\gamma = \sum_{i=1}^{N} \frac{(H_i - \bar{H})(H_i' - \bar{H'})}{\sqrt{\sum_{i=1}^{N}(H_i - \bar{H})^2 \sum_{i=1}^{N}(H_i' - \bar{H'})^2}} \tag{3.11}$$

H is the result from the equivalent source model and H' is the result from the full wave simulation (tangential components of H and H'). N is the number of the measured samples, and $\bar{H}$ and $\bar{H'}$ are the averages of H and H' for the N samples. From Fig. 3.4 (a) it can

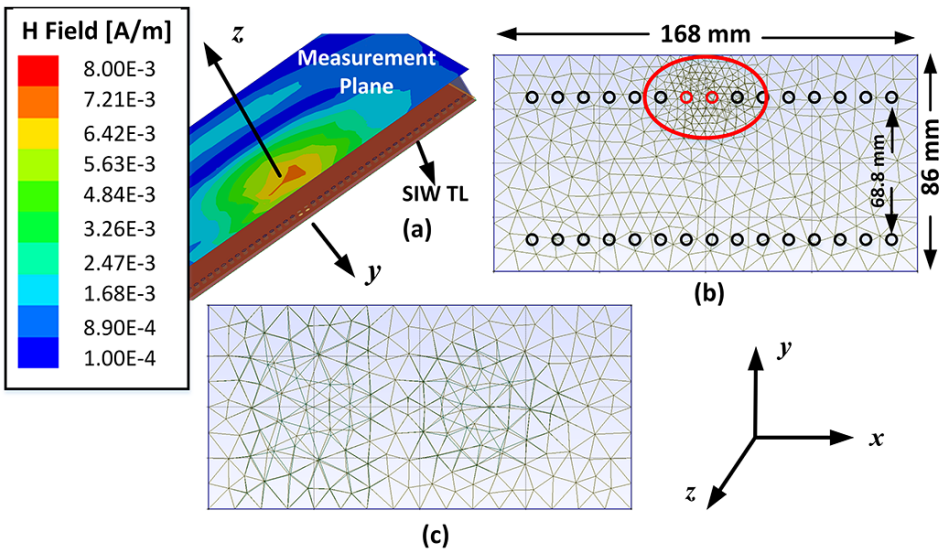

Fig. 3.3: A depiction of the magnetic fields on the measurement plane and the discretization scheme (a) the measured magnetic field on the measurement plane, (b) refined mesh, (c) uniform mesh.

be deduced that by increasing the scanning resolution the condition number of matrix A is decreased, which means more stability to the measurement errors. By increasing the scanning resolution as long as (3.10) is satisfied, the condition number and the correlation coefficients (Fig. 3.4 (a) and Fig. 3.5 (a), respectively) are close to constant values, and the accuracy is not improved any more.

With respect to the mesh size, refining the mesh size may significantly increase the condition number that leads to worse results. On the other hand, a fine mesh is required to completely model the DUT. Hence, there should be a balance between information integrity and numerical stability.

With regard to the scanning area, a scanning plane equal to or larger than the DUT perimeter is enough to reconstruct the currents precisely. By further increasing the size of the scanning area, the accuracy of the reconstructed currents is not enhanced, and again the condition number and the correlation coefficient converge to a constant as it is shown in Fig. 3.4 (b) and Fig. 3.5 (b).

Considering the scanning height, the higher it is, the lower is accuracy as can be seen in Fig. 3.4 (c) and Fig. 3.5 (c). Yet according to (3.10), a very close distance between the probe and the sample board leads to a significant increase in the scanning resolution, causing a very time-consuming measurement and post-processing for the source reconstruction method.

3.2.2 Field and material variation

To evaluate the field variation, the reconstruction surface is divided into square cells, and each data point is at the center of a square. The size of the square cells is chosen to be smaller than the smallest feature in the circuit. For each point, p_k, a set of neighboring points, $N(p_k)$, are chosen. These neighbors are located at the center of the squares that have at least a common edge or vertex with the cell of p_k. These cells are used to calculate the

gradient $\nabla|H_{(1,2)}(x,y)|$

$$\nabla|H_{(1,2)}(x,y)| = (\frac{\partial|H_{(1,2)}(x,y)|}{\partial x}, \frac{\partial|H_{(1,2)}(x,y)|}{\partial y}) \tag{3.12}$$

where 1 and 2 indicate x and y, respectively. This gradient characterizes the local linear approximation $\tilde{H}_{(1,2)}(x,y)$ at p_k, as,

$$|\tilde{H}_{(1,2)}(x,y)| = |H(x,y)| + (\nabla|H_{(1,2)}(x,y)|)_{p_k}(p - p_k) \tag{3.13}$$

Consider that $(\nabla|H_{(1,2)}(x,y)|_{p_k}) = A^{-1}b$ is calculated by fitting a hyperplane through point p_k, based on its V neighbors $\{p_{kv}\}_{v=1}^{V}$ [53], where

$$A = \begin{pmatrix} x_{k_1} - x_k & y_{k_1} - y_k \\ x_{k_2} - x_k & y_{k_2} - y_k \\ \cdots & \cdots \\ x_{k_v} - x_k & y_{k_v} - y_k \end{pmatrix} \tag{3.14}$$

$$b = [|H_{(1,2)}(p_{k_1})| \quad |H_{(1,2)}(p_{k_2})| \quad \ldots \quad |H_{(1,2)}(p_{k_v})|] \tag{3.15}$$

Once the local linear approximation of the dynamic behavior of the near-field pattern is calculated using (3.12), the estimated value of the field at p_k is compared with the true value

$$\bar{W}(p_k) = \sum_{v=1}^{V} ||\tilde{H}_{(1,2)}(p_k)| - H_{(1,2)}(p_k)| \tag{3.16}$$

A large value of $\bar{W}(p_k)$ indicates that the field is varying rapidly at this area. A normalized matrix is used to describe the dynamic variation of field near p_k relative to the field variation near the other points [54].

$$W(p_k) = \frac{\bar{W}(p_k)}{(\bar{W}(p_1) + \bar{W}(p_2) + \ldots + \bar{W}(p_k))} \tag{3.17}$$

To calculate the material variation, a number between 0 to 1 is assigned to each cell so that if the corresponding area on the surface of the board is fully covered by metal, the number is 0; but if it is not covered by metal, the number is 1. If the area is partially covered by metal, the number is between zero and one corresponding to the percentage of the area of the cell that is covered by metal.

3.2.3 The aperture model for the defective vias in the SIW structure

When there is no ground plane in the vicinity of the SIW structure, the aperture model is proposed in this study for the defective vias. According to the electromagnetic theory, if the field on the surface of an aperture is known, the fields in front of it can be calculated using the following relations [65].

$$\vec{A} = \mu \frac{e^{-j\beta r}}{4\pi r} \hat{n} \times \iint_{S_a} \vec{H}_a e^{j\beta \hat{r}.\vec{r'}} . d\vec{S'} \tag{3.18}$$

$$\vec{F} = \epsilon \frac{e^{-j\beta r}}{4\pi r} \hat{n} \times \iint_{S_a} \vec{E}_a e^{j\beta \hat{r}.\vec{r'}} . d\vec{S'} \tag{3.19}$$

$$\vec{H} = \vec{H}_A + \vec{H}_F = \frac{1}{\mu} \nabla \times \vec{A} - j\omega \vec{F} - \frac{1}{j\omega\mu\epsilon} \nabla(\nabla . \vec{F}) \tag{3.20}$$

where E_a and H_a are the fields existing over only some finite portion S_a of the plane S, as shown in Fig. 3.6 (a). To examine the proposed model, two defective vias in a SIW TL are modeled using apertures, as shown in Fig. 3.6 (b). The tangential fields over the surface of the defective vias are extracted from HFSS and utilized to calculate the fields near the SIW transmission line. The triangular discretization of the surface of the vias is used to extract the fields from HFSS as shown in Fig. 3.6 (c). Results are depicted in Fig. 3.6 (d). The dotted line represents the magnitude of H field obtained directly from full wave simulation in HFSS over a line 1mm above the vias (line 1 in Fig. 3.6 (b)). A good agreement between

the simulation result and the analytical solution confirms this idea that the defective vias can be modeled using apertures when the SIW structure is in free space.

3.2.4 The patch antenna model of the interaction between the SIW structure with the ground plane of the probe array

Since in RFX2 a finite ground plane is used to isolate the probe array from the other RF and digital circuits for EMC/EMI reasons, a study is carried on to assess the disturbing effect of the ground plane that describes how the ground plane affects the field distribution and the reconstructed currents. In addition, the measurement configuration is simulated using electromagnetic simulation software. The ground plane disturbance is evaluated by comparing the free-space simulation with the probe array simulation. The disturbance is characterized as a function of the size of the SIW structure and its distance from the scanner. Then, experimental data are presented for the measurement of near-field, and the results are compared with those from full-wave simulation. In this study, the patch antenna is utilized to model the interaction between the SIW structures and the ground plane underneath the RFX2 probe array. The SIW TL with two defective vias and its equivalent patch antenna that is fed with two coaxial cables at the position of the defective vias are depicted in Fig. 3.7 (a) and (b).

When the wavelength of the near-field wave is as the same order as the size of the electronic circuits, it may introduce resonance phenomena on the inner connections of the circuit. As it is shown in Fig. 3.7 (c), because of the effect of the ground plane on the H field, the amplitude of the magnetic field looks like two x-oriented slabs, distant by one half wavelength, resulting from the resonance of the equivalent SIW and conducting plate resonator. This seems similar to the very near-field of a patch antenna excited by dipole feeds located at the defective vias positions, as shown in Fig. 3.7 (d).

As shown in the simulation and measurement results section, the comparison of the reconstructed fields is much better than that of the measured fields since the resonance

that is visible at the measurement plane disappears close to the vias. The disappearance of the resonance patterns could be explained by the fact that the field decreases very rapidly around the vias while the field spreads out more slowly by increasing the distance from the SIW plane. Thus, when we use RFX2 probe array to measure the near-field of the SIW structures and detect the defective vias, the impact of the ground plane on the reconstructed near-field is negligible. In Fig. 3.8, it is depicted that the graphs of the magnitude of the magnetic field at the location of the defective vias are similar if that the SIW TL is in free space and close to a finite ground plane.

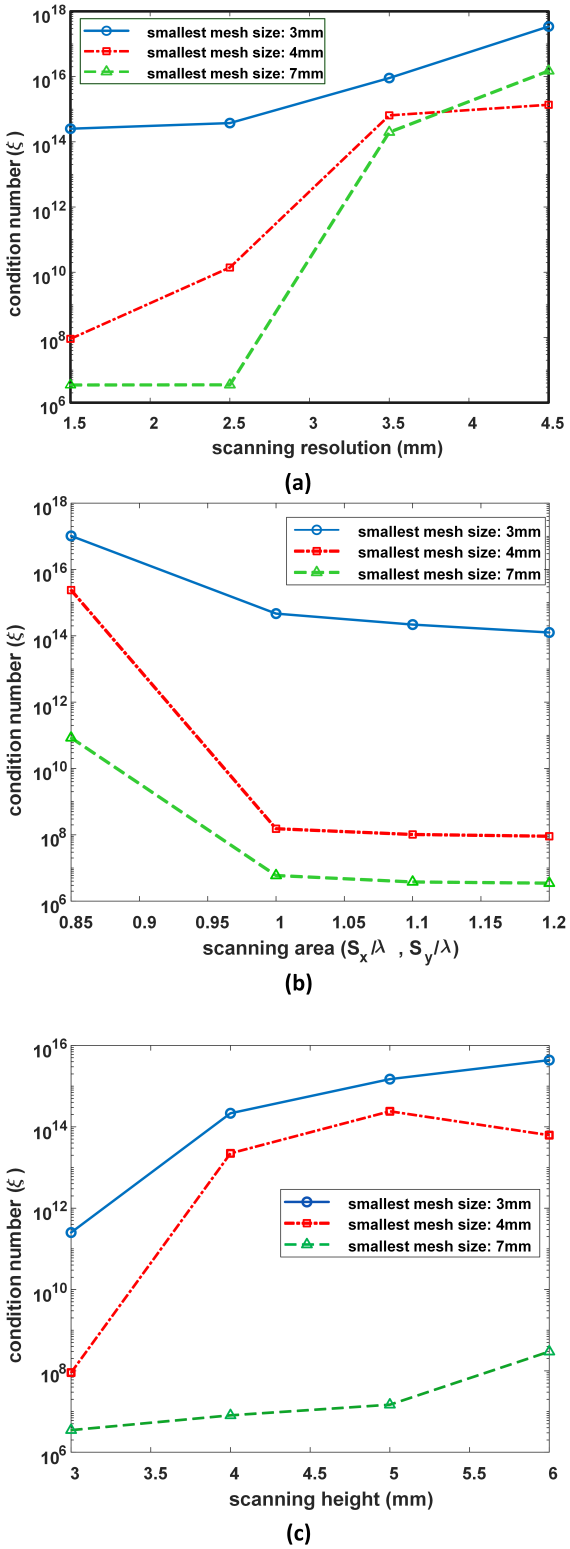

Fig. 3.4: The effect of the (a) scanning resolution, (b) scanning area, and (c) scanning height on the condition number of the matrix A.

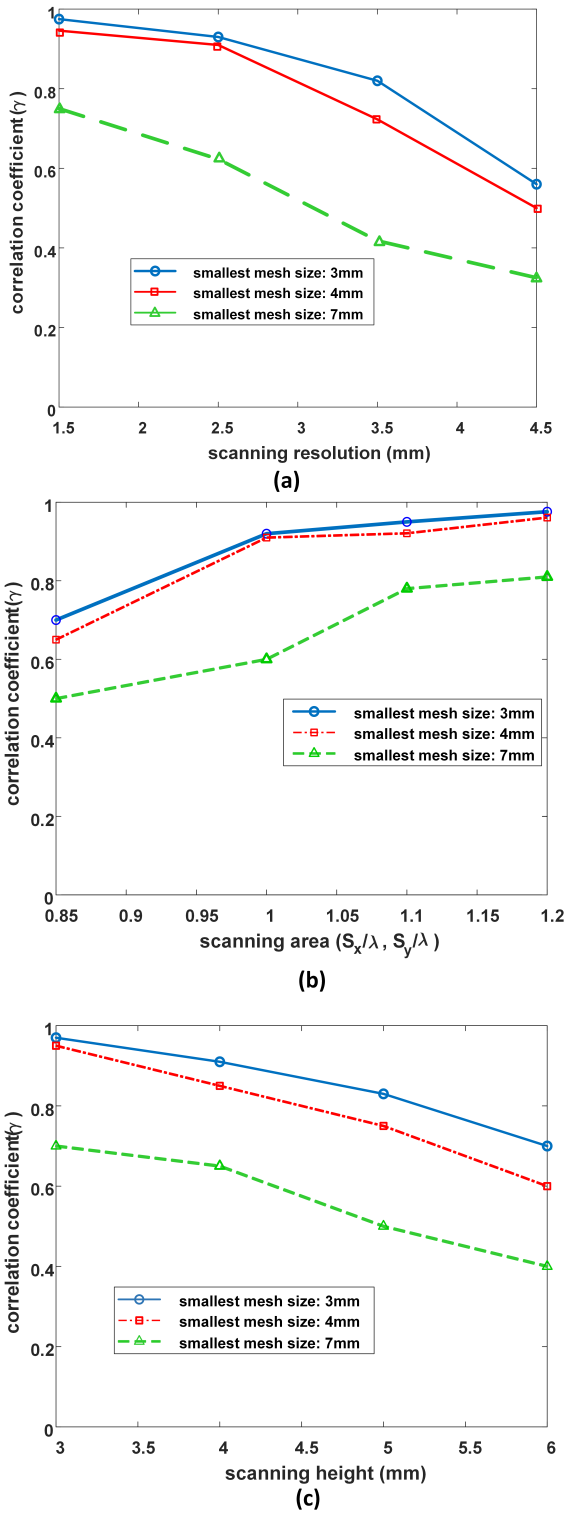

Fig. 3.5: The effect of the (a) scanning resolution, (b) scanning area, and (c) scanning height on the correlation coefficient.

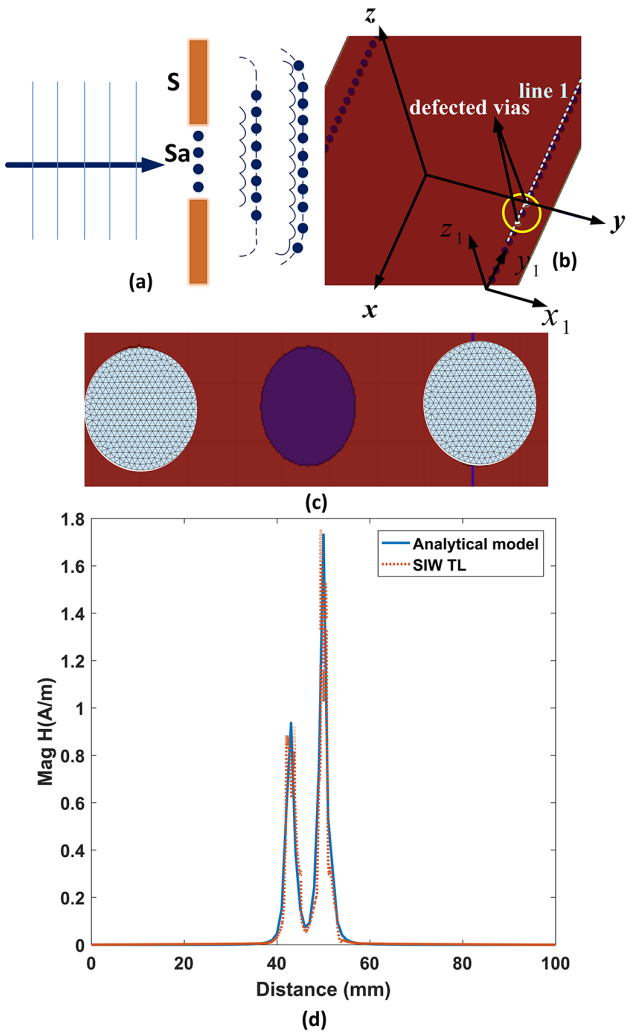

Fig. 3.6: The aperture model of the defective vias of the SIW structure in free space, (a) the aperture model of a defective via, (b) a SIW TL with two defective vias, (c) the discretized surface of the defective vias to extract the tangential components of the fields over the area of the apertures from HFSS, and (d) the comparison of the magnitude of magnetic field at 1mm away from the SIW TL calculated using the analytical model and obtained from full wave simulation.

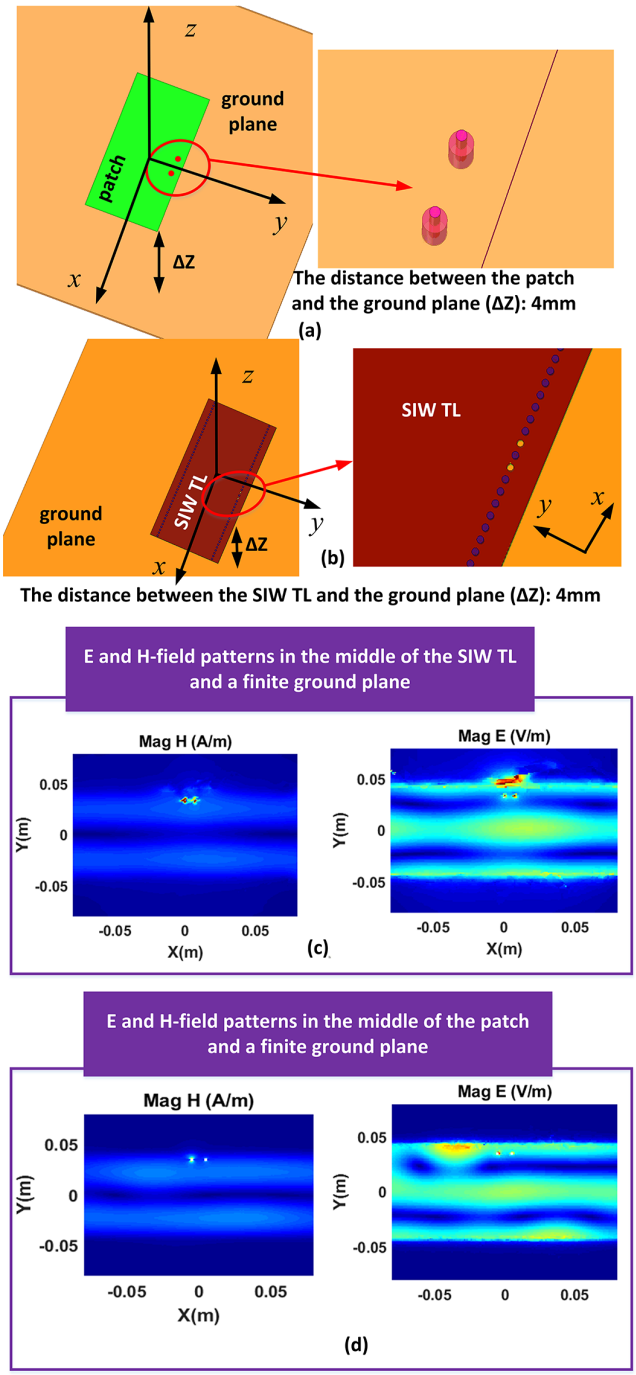

Fig. 3.7: The comparison of E- and H- field patterns of the SIW TL close to the ground plane with a patch antenna (a) a patch antenna that is fed with two coax connector at the location of the defective vias, (b) A SIW TL with two defective vias, (c)the magnitude of the H-field and E-field at the distance of 2mm from the SIW TL, (d) the magnitude of the H-field and E-field at the distance of 2mm from the patch, between the patch and the ground plane.

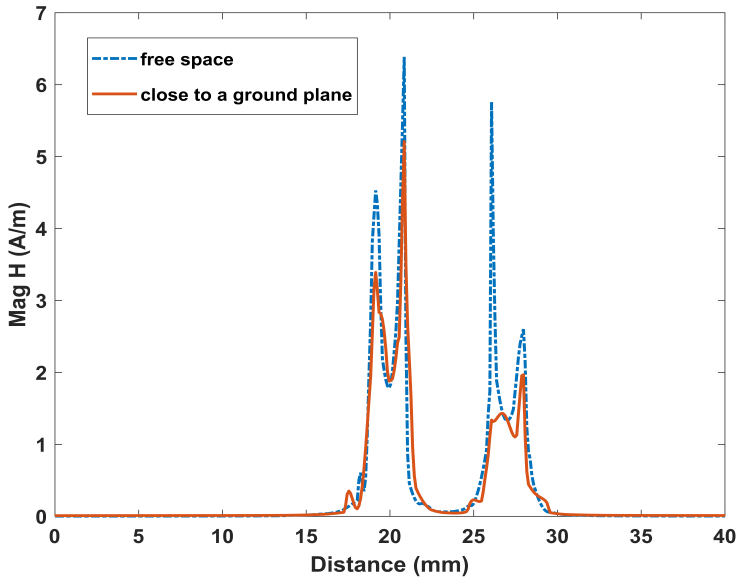

Fig. 3.8: The comparison of the magnitude of the magnetic field at the location of the defective vias when the SIW TL is in free space and close to a finite ground plane.

3.3 Measurement and Simulation

Single probe setup

Since for the single probe measurement the phase and amplitude of the tangential field components are measured and a large number of data points must be collected, substantial automation of the measurement process is required.

The measurement set up is depicted in Fig. 3.10 (a). One single probe that is similar to the probes of RFX2 is used to measure the near-field. Port 1 of the VNA is connected to the DUT and port 2 is connected to the measuring probe. At each step of the movement, the magnitude and phase of S_{21} are recorded. Although there are various types of probes for near-field measurement [55]– [57], in this study, the single probe is chosen as being the same as any of the probes that are used in RFX2 (Fig. 3.9) to compare the results obtained by different measurement and simulation scenarios. In the ideal case, the input power and the probe factor are to be known to calculate the absolute value of the measured field. For the H-field probe, the probe factor (PF) is defined as [69]

$$PF(f) \triangleq \frac{H(f)}{V_{out}(f)} \; in \; unit \; of \; \frac{\frac{A}{m}}{V} \tag{3.21}$$

On the other hand, the goal in the diagnostic tests is to find the location of the hotspots and the absolute near-field emission level is not required. Moreover, measuring the power at the position of the measuring probe is not straightforward.

By utilizing the positioner (Fig. 3.10 (b)), that is controlled by the computer as it is shown in Fig. 3.11 (a), we can move the probe in x, y, and z directions. For the measurement of the tangential components of the magnetic field parallel to the DUT surface (Fig. 3.11 (b)), the probe is tilted by 90 degrees relative to the sample surface. By rotating it around the vertical axis, various tangential field components are measured. The trajectory of the probe is shown in Fig. 3.11 (c). The black line is the path along which the probe measures the fields and the red dashed line shows the track of the probe through which only the probe

passes to reach the defined point to record the data.

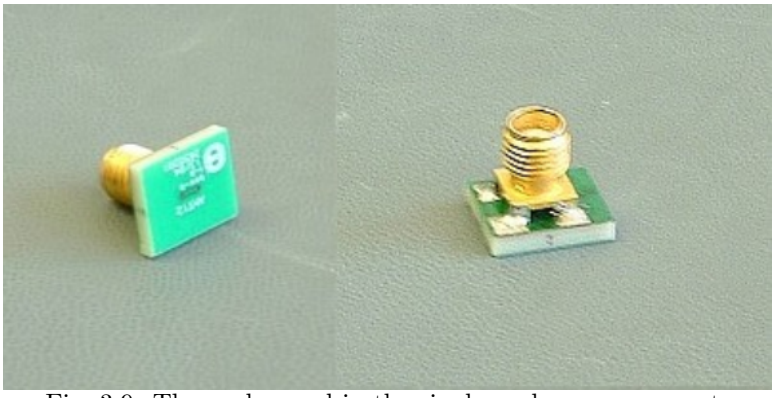

Fig. 3.9: The probe used in the single probe measurement.

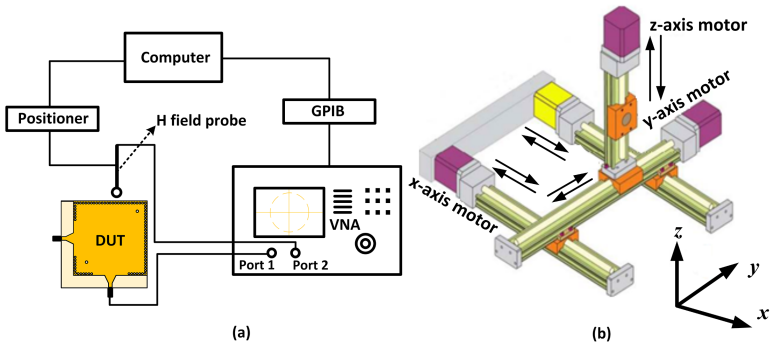

Fig. 3.10: Single probe measurement, (a) the schematic of the setup for the single probe measurement, (b) The xyz positioner.

Probe array setup

RFX2 probe array is used to measure the magnetic near-fields of the SIW structures. The measurement setup is shown in Fig.3.12. A power divider has been used to provide an external stable phase reference to the scanner to make sure all the scans are phase coherent. The distance between the device under test (DUT) and the surface of the scanner is 4mm. This value is chosen based on the parametric study, which is explained in section 3.2.1. Since the probes are 1mm below the surface of the scanner, the distance between the DUT and the measuring probes is 5mm. For example, at the frequency of 2GHz with this height, the maximum resolution can be 2.5mm according to equation(3.10). Because the distance

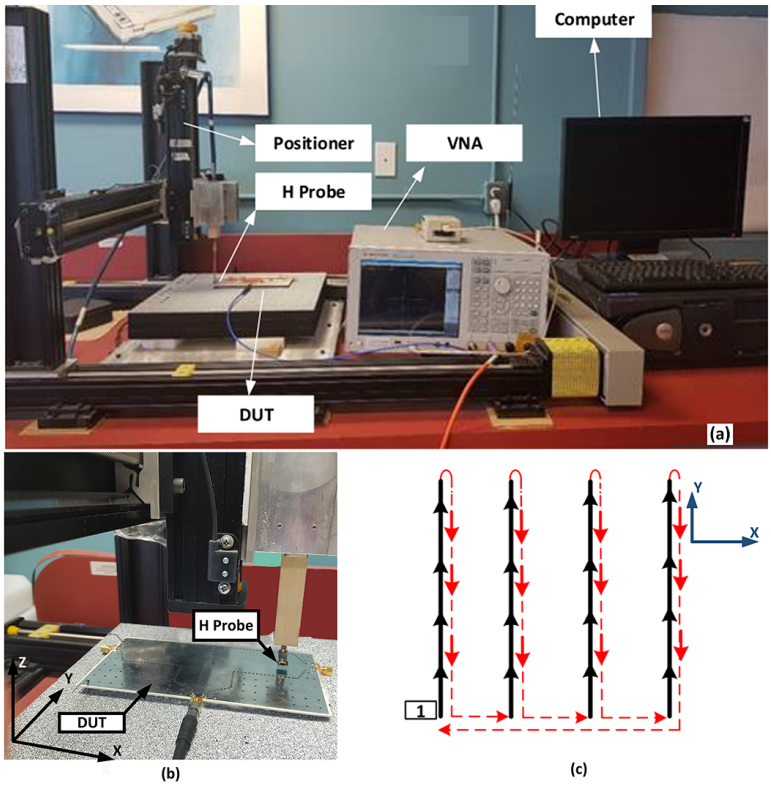

Fig. 3.11: Single probe measurement, (a) the experimental setup for the single probe measurement, (b) The single probe measurement of the SIW structure, (c) the trajectory of the single probe.

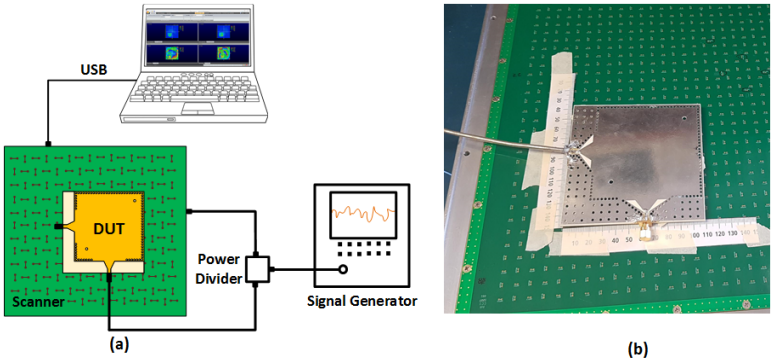

Fig. 3.12: The probe array measurement setup,(a) a schematic of the probe array measurement setup, (b) The SIW filter above the probe array.

between two adjacent probes is 10mm, to achieve the resolution of 2.5mm, the sample board is moved up a total of 8 times and sideways a total of 4 times for 32 total measurements (Fig. 3.13). For instance, the first position is (0,0). The second position is up 2.5mm. For the first 8 measurements, the board is moved up each time. Then the sample is shifted 2.5mm

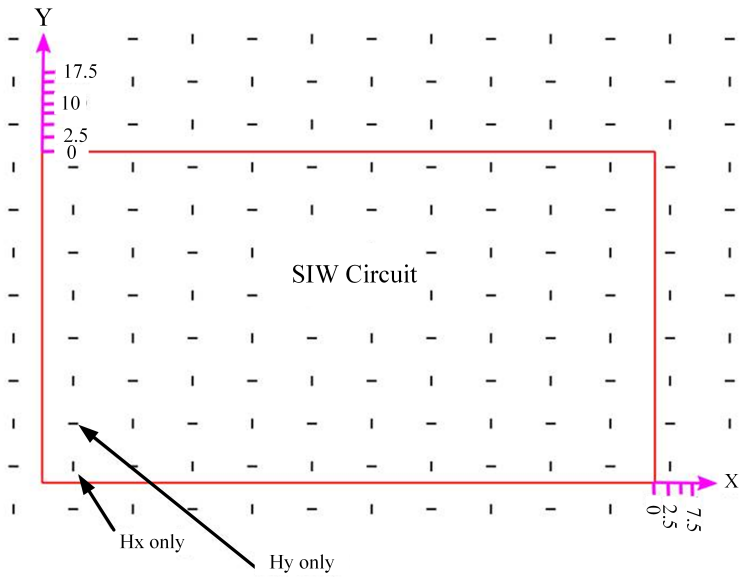

Fig. 3.13: Schematic view of SIW board movement above the probe array.

to the right and all 8 upward measurements are repeated. Eight upward measurements have to be done because the probes measure only one polarization. In the data set of the RFX2 software, the data are interpolated to fill in the missing values. Hence, the interpolated data must be discarded and then the final 4 measurements of an upward sweep are used to fill in the other polarization. To reconstruct the equivalent currents in the simulation, only the measured fields in an area that is approximately above the DUT is utilized because by using the whole probe array fields, the simulation will be very slow. Besides, using the measured fields that are far from the DUT does not increase the accuracy.

Simulation and meaurement results

As the first case, the near-field of a SIW dual mode filter is collected using a single probe and probe array. The near-field measurement is performed at a single frequency of 1.84 GHz. This frequency is chosen because based on $|S21|$ and $|S11|$, the defective device still works as a filter at this frequency (Fig. 3.14). The measured fields using the single probe and probe array setup and the scanned data in the full wave simulator are depicted in Fig. 3.14. The fields at the back side of the structures are measured since there is less radiation from

the CPW (coplanar waveguide) to SIW transition at the back side, but still some radiation at the position of the connectors can be seen. The diameter of the side vias is 2mm and the diameter of two main vias in the middle of the structure is 3mm. The pitch is 3mm as well. The reconstructed fields shown in Fig. 3.14 demonstrate that the defective vias are detectable from both the measurement and simulation data using the proposed method.

To determine at what distance the fields should be reconstructed to have proper resolution, the following procedure is recommended. The amplitude of the magnetic field over a plane that contains the cross section of two adjacent defective vias in the SIW filter is plotted as shown in Fig. 3.15 (a). It can be seen that at the distance of 1mm from the board, two defective vias can be resolved. Since the distance between these two vias is very small compared to the wavelength, one can use the aperture model formulas given in section 3.2.3 and assume that the current distribution over two apertures is the same and uniform. Then, the distance at which the two neighboring defective vias can be distinguished is calculated. The result of this approach for the defective vias of the filter is shown in Fig. 3.15 (b). Although the two apertures can be resolved at 1mm, at closer distances, such as 0.5mm that is used here, the resolution is higher. This process can be integrated in the near-field measurement software to automatically find the maximum distance at which the defective vias are precisely detectable.

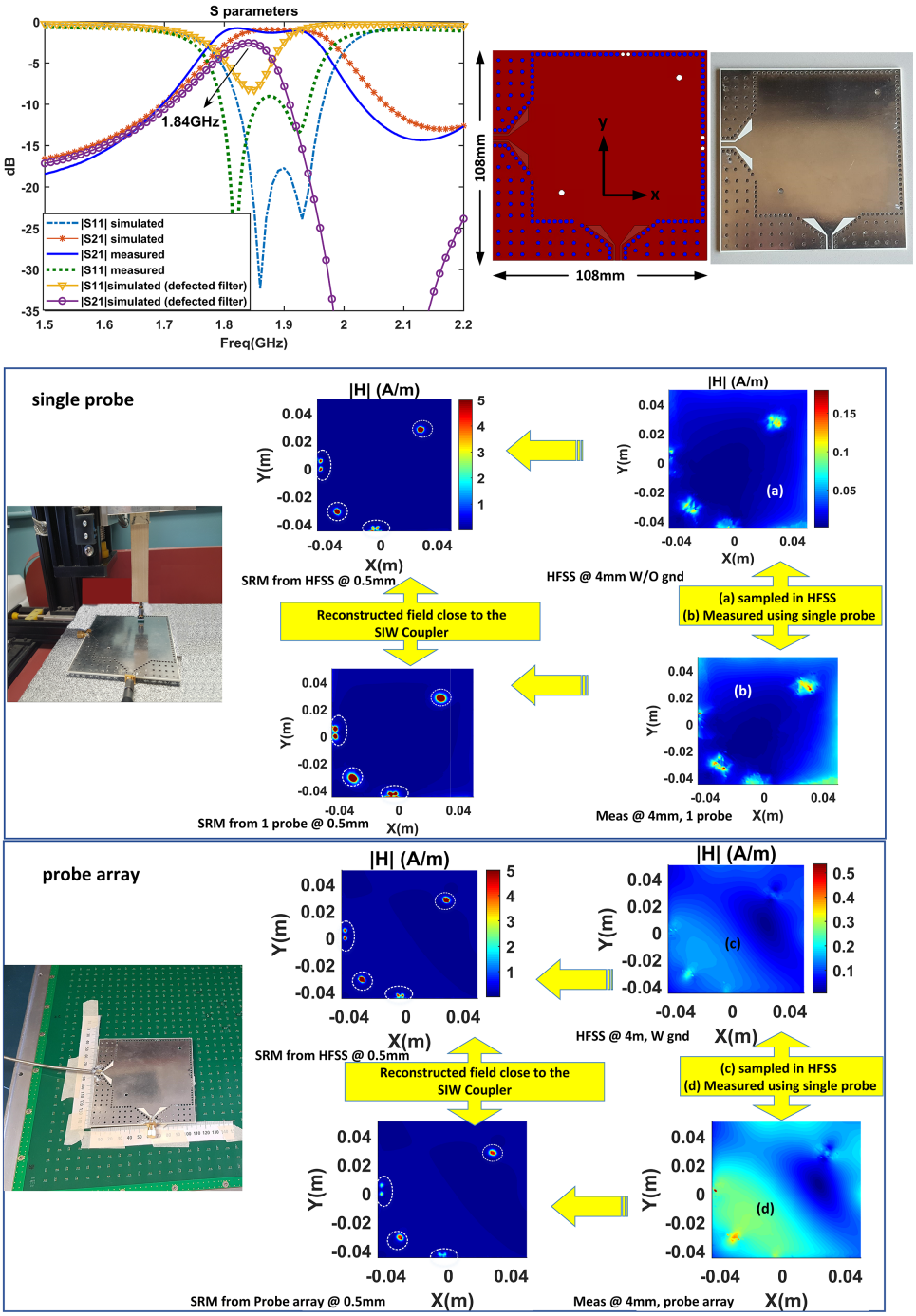

Fig. 3.14: Detection of the defective vias in a SIW dual mode filter.

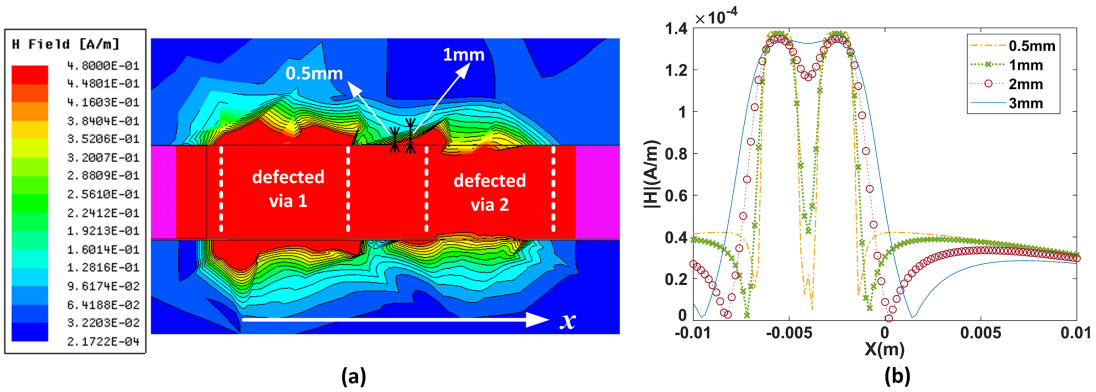

Fig. 3.15: The distance from the board at which two adjacent defective vias can be resolved (at 1.84GHz), (a) a view of the magnetic field amplitude computed using HFSS full wave simulator, (b) the magnetic field amplitude calculated analytically.

To remove the radiations due to the radiative parts of the circuit, such as the SIW to CPW transitions, the near-field of the circuit when the vias are covered with metal (for instance, copper tape) can be subtracted from the near-field data of the circuit when the vias are uncovered. The effect of the defective vias is more evident as shown in Fig. 3.16. This process can be applied to both simulation and measurement. Moreover, in the measurement, the feed lines and transitions can be covered by absorbers to decrease their radaitions in the near-field measurement data. Obviously, if the radiated fields from vias get dominated by other radiation effect in the circuit, it is very difficult to detect the defective vias.

In regard to the measurement time, the trajectroy in Fig. 3.11 (c) can be modified to have faster single probe measurement. Also, in the case of probe array measurement, the

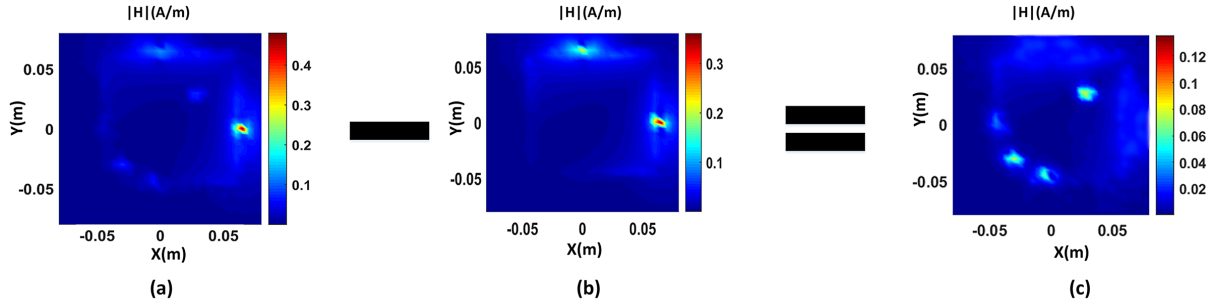

Fig. 3.16: Subtraction of the radiation from the transitions and feed lines from the total near-field data. (a) The total near-field data with defective vias, (b) The total near-field data without defective vias, (c) the radiation from only the defective vias.

sample board can be moved above the probe array mechanically rather than manually. Here a procedure is described to calculate the time difference between single probe and probe array measurements. For both set ups the required time to recored the measured data is assuemed to be the same. We presume that the required measurement resolution is x mm. The distance between two adjacent probes in the probe array is 10 mm. The probe array consists of 40×40 probes. As mentioned at each point only one polarization of the magnetic field (x or y), is measured. Thus, to actually measure both polarizations for each sample point, the sample board needs to be moved above the probe array ($\frac{10}{x} \times \frac{2\times 10}{x}$) times, and at each point 40×40 electronic switches should be switched. As a result, the probe array measurement time can be calculated as follows:

$$t_p = \frac{10}{x} \times \frac{2 \times 10}{x} \times (40 \times 40)\, t_e + \frac{2 \times 10 \times 10}{x^2}\, t_m \tag{3.22}$$

where t_p is the required time for probe array measurment, and t_e and t_m denote the switching time of an electronic switch and the required time to mechanically move the sample borad. The single probe measurement time can be calculated as:

$$t_s = \frac{(40 \times 10)(40 \times 10) \times 2}{x^2}\, t_m \tag{3.23}$$

where t_s is the required time for single probe measurment. The coefficient 2 is added because the single probe measures only one polarization of the field. Once one polariztion is measured for all the points, the probe is rotated 90^o in the horizontal plane, and the second polarization will be measured. If one assumes $t_e = 0.003\, sec$ [42], $t_m = 0.05\, sec$ (for instance utilizing 8MT295Z-340 positioner in [43]), and $x = 2$ mm, the single probe setup requires about one more hour to collect the data.

In this study, the defective vias could be detected using only one frequency. Since to detect a defective via the field configuration inside the SIW device must be such that the defective via is excited and carries some current, and at some frequencies, some vias in the structure

may be excited very little, defective vias may not radiate and be detectable. One way to overcome this problem might be to vary the frequency, which will change the excitation of the vias in different parts of the filter. Using different frequencies for diagnostic tests is the topic of our future research.

The second sample is a coupler as shown in Fig. 3.17. The frequency of measurement is 2GHz. This frequency is chosen since at higher frequencies many samples are required given the big size of the coupler. At lower frequencies, the S parameters of the coupler are not acceptable. The defective vias with different distances from each other are investigated to evaluate the resolution of the method. Although the diameter of the vias is 2mm and the pitch is 3mm, it is not easy to locate the defective vais by using the measured fields. However, by looking at the reconstructed fields at 0.5mm away from the coupler, the defective vias can be detected precisely. As shown in Fig. 3.17, there is a clear resonance between the coupler and the finite ground plane, but still the defective vias can be localized from the reconstructed fields. The magnetic near-field is measured at 2GHz from which the location of the defective vias is not detectable.

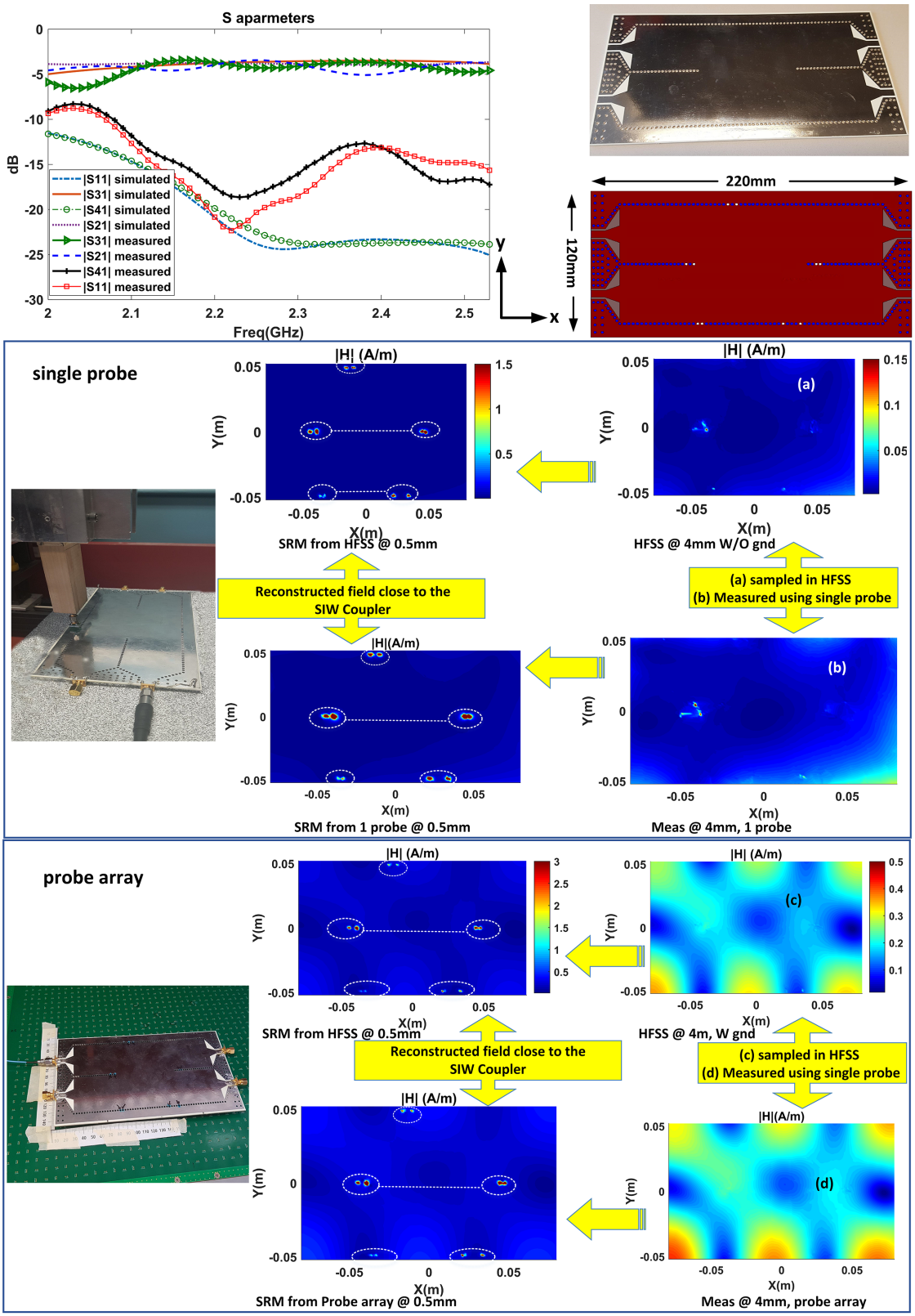

Fig. 3.17: Detection of the defective vias in a SIW coupler.

The machine learning algorithm to classify different radiation sources

Here, a machine learning algorithm is used to distinguish different radiation sources by utilizing magnetic field and material variations for the data points. The tangential components of magnetic field, H_x and H_y, are related to the surface currents. In feed lines and antenna, the surface currents have particular forms that depend on the metal parts of the circuits (for instance, in the antennas, the size of the circuit in the radiating direction is about one-quarter wavelength). Thus, the H_x and H_y and the material of the testing point and its surrounding area (whether it is metal or not) can be utilized to classify the source of different types of radiation in the circuit. For instance, the radiations come from the radiative parts, such as feed lines and transitions, or from the defective vias. Here, a machine learning algorithm is proposed that uses the field and material variation to classify the reconstructed near-field data. The material assignment process is shown in Fig. 3.18 (a). A number between zero and one is associated with each cell such that fully covered by metal means 0, fully covered by dielectric indicates 1, and partially covered by metal designates a number between 0 and 1 to the corresponding cell. H_x and H_y variations are also shown in Fig. 3.18 (b) and (c).

To classify the reconstructed near-field, the data are labeled based on the areas shown in Fig. 3.19 (a). The classes 1-6 are shown in Fig. 3.19 (a), and class 7 represents the

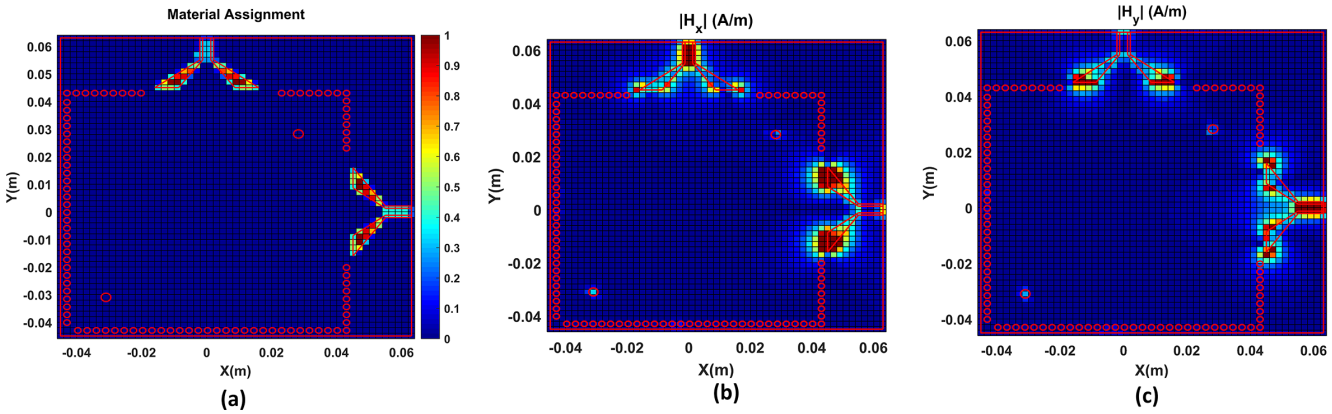

Fig. 3.18: Material assignment and field variation (at 1.84GHz) for the SIW filter, (a) material assignment, (b) $|H_x|$ and (c) $|H_y|$ variation.

remaining points. Classes 1 and 2 both represent radiations of the defective main via with diameter of 3mm. Class 2 is away from the radiations of the feedlines. Classes 3 and 4 represent the radiations of feedlines and CPW to SIW transitions, and they are distributed over two diffetrent directions (x and y). The spatial distributions of classes 6 and 5 are in two perpendicular directions of x and y, and represent the radiations from the defective side vias. The classification learner application of MATLAB 2018 is used in which the data are classified using different classification algorithms such as Support Vectro Machine (SVM) and K-nearest neighbors (KNN). About 70% of the data are used to train the algorithm, and the rest are used to test the model. In KNN, for each test data point, the K nearest training data points are considered and the test data point is assigned to the most frequent class in the area. This algorithm works based on the distances of the clusters. Thus, considering the spatial distribution of the data points, it seems KNN is the best classification method for the type of the data presented in this work. In the classification learner application of MATLAB, KNN is compared to other classification algorithms such as SVM and the best accuracy obtained from KNN (weighted KNN) algorithm that is 96.8%.

The scatterplot of the data, along with the values predicted from the model, are shown in Fig. 3.19 (b). It can be seen that the near-field radiations of the two transitions are clustered along $|H_x|$ and $|H_y|$ axes. In Fig. 3.19 (c), parallel coordinate plots are depicted. These plots are used for multivariate numerical data in which each variable has its own axis and the axes are parallel. Generally, each axis is normalized to have the same scales. Values are represented as a series of lines that are linked over the axes. Thus, the value of three parameters, $|H_x|$, $|H_y|$, and material variation for each sample can be derived from this plot. To evaluate a predictive model, ROC (Receiver Operating Characteristic) plot (Fig. 3.19 (d)) is utilized. A good model must be able to predict a negative as a negative and a positive as a positive if we assume that there are only two classes, one positive and one negative. In the ROC curve, sensitivity is the probability of predicting a real positive as a positive which is plotted versus 1-specificity that is the probability of predicting a real negative as a positive.

$$TPR/Sensitivity = \frac{TP}{TP + FN} \tag{3.24}$$

$$Specificity = \frac{TN}{TN + FP} \tag{3.25}$$

$$FPR = 1 - Specificity = \frac{FP}{TN + FP} \tag{3.26}$$

where TP, FN, FP, FPR, and TPR stand for true positive, false negative, false positive, false positive ratio, and true positive ratio, respectively.

The best decision algorithm has a high value of sensitivity and low value of 1- specificity; thus, it predicts most of the true positives as positive and few of the true negatives as positive. It means the further the curve is from the diagonal line, the better the model is at distinguishing between positives and negatives. The area under curve (AUC) for an excellent model that has good measure of separability is close to 1. If AUC for a model is 0, it means it is predicting 0s as 1s and 1s as 0s. The AUC of 0.5 for a model means that it has no separation capacity [68].

In the concept of machine learning and especially classification, a confusion matrix is a table that visualizes the performance of a classification algorithm [68]. Each row represents the true classes to which the instances belong, and each column shows the predicted classes. In the confusion matrix (Fig. 3.19 (e)) of 20 actual class 3, the classification algorithm predicted that 3 are class 4 and 17 are class 3. It can be seen that the algorithm has not distinguished class 6 from class 7 and 2 but it can differentiate the other classes quite well. In this table all correct predictions are located on the diagonal of the matrix, and the wrongly predicted values are outside the diagonal.

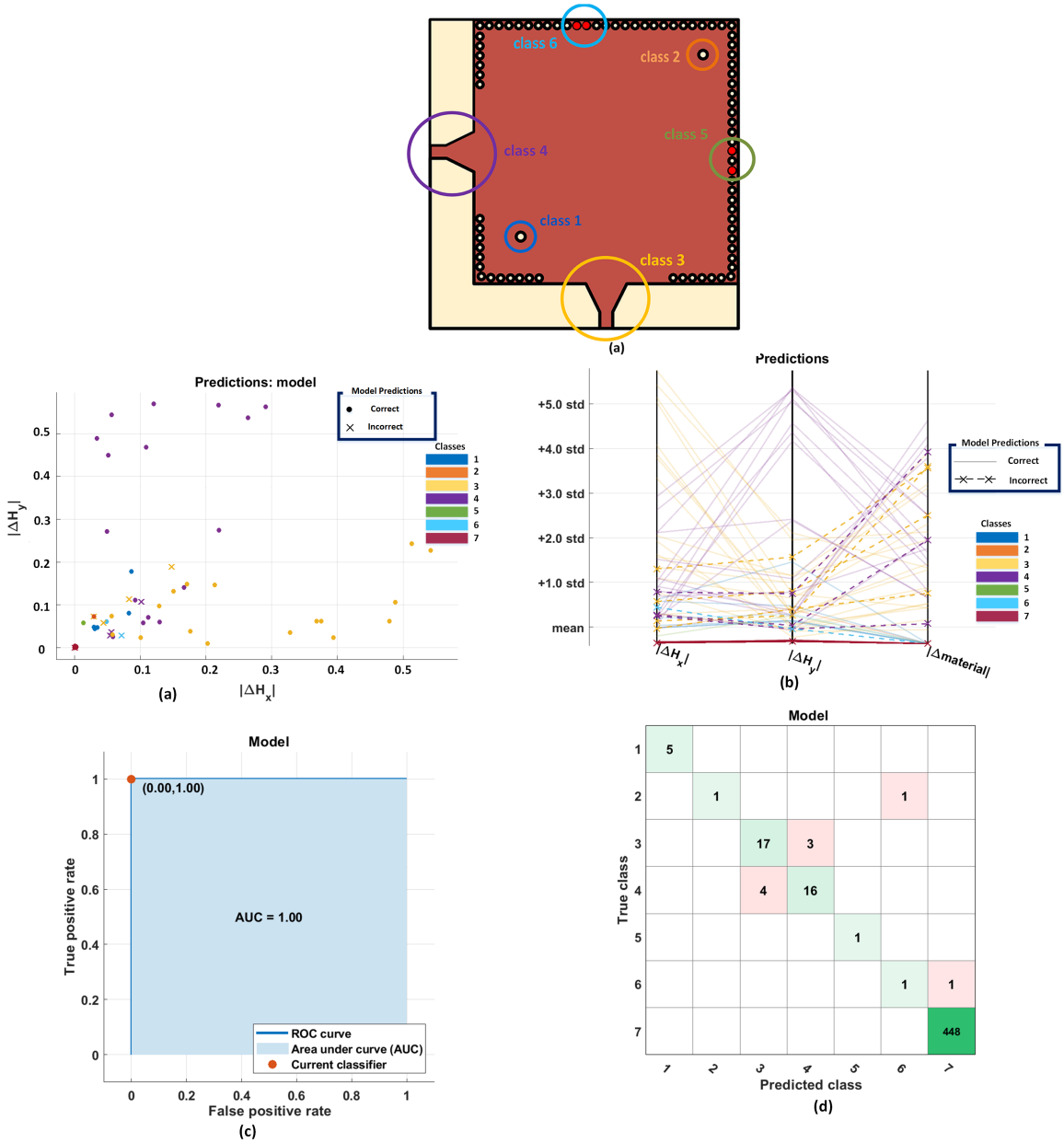

Fig. 3.19: Classification of the reconstructed near-field samples, (a) the labels for the classification algorithm , (b) scatterplot, (c) parallel coordinates plot, (d) ROC graph, and (e) confusion matrix.

3.4 Conclusion

In this chapter, a high-resolution very near-field measurement method is proposed to pinpoint the defective vias in SIW structures. Firstly, the very near-field radiation of SIW structures, such as a dual mode filter and coupler, measured using a single probe and a fast electronically switched probe array. Then the SRM method is utilized to reconstruct the currents on a closed surface, which encompasses the structure. These equivalent currents are used to calculate the magnetic fields at a close distance of the sample board.

The maximum distance from the board at which the defective vias can be resolved calculated analytically by modeling the defective vias with apertures. Moreover, to have a more accurate representation of the equivalent sources at the position of higher radiation, adaptive meshing and finer mesh are used . In the measurements using the probe array, since a finite ground plane in the RFX2 separates the probe array from the other RF and digital circuits for EMC/EMI reasons, the disturbing effect of this ground plane on the measured and reconstructed field is investigated. The results show that the field decreases very fast around the vias whilst the field spreads out at a slow speed by increasing the distance from the SIW structure. Finally, a machine learning algorithm is proposed to classify the radiations in the circuit based on the field and material variation. This algorithm helps to determine whether the radiations are because of the radiating parts of the circuit, such as feed lines and transitions, or due to the defective vias. The measurement and simulation results validate the accuracy of the proposed method.

In this chapter, a foundation is laid to automatically detect the defects using near-field measurement, source reconstruction method, and machine learning algorithm. Yet more complex circuits should be examined and the algorithm needs to be modified for various test cases such as more complicated circuits and over the air tests that are the topic of future research.

Chapter 4

Accuracy and Time Enhancement of Near-Field Antenna Measurement Considering Noise, Using an Adaptive Data Acquisition and Interpolation Technique

4.1 Introduction

The adaptive sampling algorithm is described in this chapter. For the proposed method in this chapter, the measurement is performed at 1600 points (800 points of H_x and 800 points of H_y) using an RFX2 device. Since the purpose is to feed the MoM with those measured data points that have significant information about the near field of the AUT, an adaptive algorithm is proposed to sequentially focus mainly on the strongly changing near-field regions and more samples in such areas, and to skip data points for smoothly varying locations. Thus, this algorithm in every step introduces a batch of N locations to add their near-field values. Since the newly added points are not necessarily laid on the probe locations of the RFX2, an appropriate interpolation technique is employed to estimate the value of the fields at these points. Compared to [53] and [54], in strongly varying locations every single square cell is divided into four equal cells instead of Voronoi Tesselations for two reasons: (i) The configuration of the probes in RFX2 is a uniform Cartesian grid, and (ii) with rectangular gridding, interpolating and processing the data are very simple and efficient from

analytical and computational viewpoints. If one wants to utilize the proposed algorithm for the single probe measurement approach, the scanning time might not decrease considerably because the new locations at which the fields must be measured are randomly distributed and the scanning probe must move along large distances. In such cases, a greedy algorithmic approach that simply considers the remaining locations can be employed. Based on that, the probe is moved to the closest location to the current one [10]. The main objectives of this chapter are as follows: (1) the circuit noise source of an electronically switched probe array is modeled as a stochastic signal, and the electric field integral equations (EFIE) are solved with this stochastic signal as the input, (2) the performance of various interpolation techniques is investigated to estimate the value of the near-field at an unsampled location for different values of SNR, (3) an adaptive data acquisition algorithm is proposed to sample the planar near-field of antennas by measuring the data using RFX2 and decreasing the number of the required data points, and (4) a SRM method is used to calculate the far-field of the antenna using the adaptively sampled near-fields. The chapter is organized as follows. The SRM, uniform sampling, and interpolation techniques are explained in section 4.2. The circuit noise analysis is presented in section 4.3. The adaptive data acquisition method in planar near-field antenna measurement is described in section 4.4. The daptive sampling algorithm in spherical measurement along with the clustering the data are presented in section 4.5. Finally, the chapter is concluded in section 4.6.

4.2 Uniform sampling, interpolation techniques and source reconstruction method

The near-field measurements of this chapter are performed using an RFX2 device which is an electronically switched probe array. It is an array of 40×40 magnetic probes that are distributed uniformly with the sampling resolution of 1cm. A simple schematic representation of the probes orientation for this planar near-field measurement tool is depicted in Fig. 4.1.

Because of physical limitations, at each point only one component of the magnetic field is measured in X or Y directions, as shown in Fig. 4.1 . The simple averaging technique is used to calculate the complementary components. To investigate the accuracy of the simple averaging scheme compared to other interpolation techniques, linear, nearest, and natural neighbor interpolation methods are used as well to calculate the value of missing components.

Having a set of data sets, we can utilize interpolation techniques to estimate the function values at an unsampled location between precisely known data points. For interpolation techniques, the assumption is that data points are exact and the interpolant curve or surface has to pass through all data points, which are valid only between the samples, [75] and [76]. Moreover, for an ideal interpolation technique, the interpolant and its derivative are continuous.

The nearest neighbor is not really an interpolation method, and the value of a function

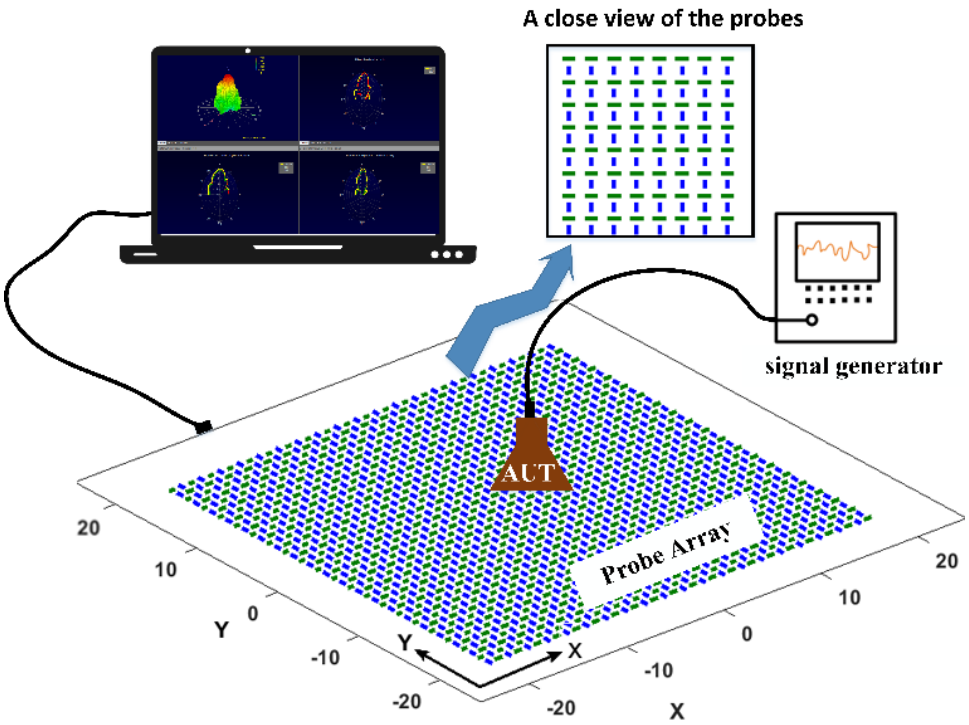

Fig. 4.1: The orientation of the magnetic probes in RFX2. At each measurement point, the probe is $X-$ or $Y-$oriented

at any location is assumed to be equal to the function of the nearest known sample. The method is local and easy to implement, but discontinuous at the boundaries [75] and [76]. The linear interpolation is based on a triangulation of the data points. The weights are the distances of the point from the vertices of the triangle. The method is local and exact, but it is not continuous at the boundaries [75] and [76].

The natural interpolation method is based on the Voronoi diagram for both selecting the data points and assigning the weights. The weights are determined by finding how much of each of the surrounding areas is shared with the other cells when a new point is inserted to the tessellation. The interpolant is local, exact, and continuous everywhere. The derivative is also continuous except at the data points [76] and [77].

Once the samples of the near-field are obtained, a source reconstruction method is applied to reconstruct the currents on the surface of the volume that encloses the AUT, that is an ellipsoide here. The tangential components of the magnetic field (amplitude and phase) that are parallel to the planar AUT are measured on the scanning plane ($\sum_M$). This measured data is linked to the equivalent electric, $\vec{J}$, and magnetic, $\vec{M}$, sources on the reconstruction surface ($\sum_R$) via EFIE, [48] and [58], as:

$$\vec{E}(\vec{r}) = \mathcal{K}(\vec{M};\vec{r}) - \eta_0 \mathcal{L}(\vec{J};\vec{r}) \tag{4.1}$$

$$\mathcal{K}(\vec{M};\vec{r}) = \int_{\sum_R} \vec{M}(\vec{r'}) \times \nabla g(\vec{r},\vec{r'}) dS'$$

$$\mathcal{L}(\vec{J};\vec{r}) = jk_0 \int_{\sum_R} [\vec{J}(\vec{r'}) + \tfrac{1}{k_0^2} \nabla\nabla'_S . \vec{J}(\vec{r'})] g(\vec{r},\vec{r'}) dS'$$

$$g(\vec{r},\vec{r'}) = \frac{e^{-jk_0|\vec{r}-\vec{r'}|}}{4\pi|\vec{r}-\vec{r'}|} \tag{4.2}$$

where $\eta_0 = \sqrt{\mu_0/\epsilon_0}$, $k_0 = \omega\sqrt{\mu_0\epsilon_0}$ and ∇'_S is the surface divergence operator. The reconstruction surface is discretized to flat triangular patches. Rao-Wilton-Glisson (RWG) basis functions (F_n) are used to represent electric and magnetic currents

$$\vec{J} = \sum_{n=1}^{N} c_n^J \vec{F}_n, \quad \vec{M} = \eta_0 \sum_{n=1}^{N} c_n^M \vec{F}_n \tag{4.3}$$

where c_ns are the unknown coefficients. Using method of moment (MoM) to solve these integral equations numerically, we have the following linear system

$$\eta_0 \begin{bmatrix} \mathcal{K}_{MR} & -\mathcal{L}_{MR} \end{bmatrix} \begin{bmatrix} c^J \\ c^M \end{bmatrix} = \begin{bmatrix} H \end{bmatrix} \tag{4.4}$$

where $\vec{H}$ indicates the tangential magnetic field components on $\sum_M$. The equation (4.3) can be rewritten in a compact form as

$$AX = H \tag{4.5}$$

where A is the impedance matric and X is the vector of the unknown magnetic and electric current coefficients [48]. For most source reconstruction problems, matrix A is ill-conditioned. Here, (4.5) is solved by Tikhonov regularization method. The cost function is defined as below

$$F = ||H - AX||^2 + \alpha^2 ||X||^2 \tag{4.6}$$

where $\|.\|$ indicates the Euclidian norm and L is the regularization parameter that is determined by L-curve method [48].

4.3 Noise modeling

Each magnetic probe is a magnetic loop which is connected to a microwave power detector. A microwave power detector is a diode utilized in its quadratic region. In this region, the output voltage is proportional to the input power [78] . In other words, the diode turns the input power, P, to a DC voltage, v_d

$$v_d = k_d P \tag{4.7}$$

$$v(t) = V_0[1 + \alpha(t)]cos[\omega_0 t + \phi(t)] \tag{4.8}$$

where $\alpha(t)$ and $\phi(t)$ are the partial amplitude and phase oscillations, respectively; in low noise condition, $(\alpha(t) \ll 1)$, the power is

$$P \approx \frac{V_0}{2R}(1 + 2\alpha(t)) = P_0 + \delta P \tag{4.9}$$

A straightforward analysis establishes the following relation between the amplitude and power fluctuations

$$\alpha(t) = \frac{\delta P}{2P_0} \tag{4.10}$$

Using eq. (4.7), the ac component of the detected voltage is $v_d = k_d \delta P$, which is related to amplitude fluctuations by

$$v_d = 2k_d P_0 \alpha(t) \tag{4.11}$$

Turning voltages into spectra, we have

$$S_v(f) = 4{k_d}^2 {P_0}^2 S_\alpha(f) \tag{4.12}$$

On the other hand, the output of the power detector is a voltage that is related to the magnetic field by a transfer function $\gamma(\omega)$. If we assume that there is an error in $\gamma(\omega)$, i.e. $\epsilon(\omega)$, and a noise of voltage, $N_v(\omega)$, we obtain an apparent magnetic field, $H^a(\omega)$, given by

$$H^a(\omega) = [\gamma(\omega) + \epsilon(\omega)][V(\omega) + N_v(\omega)] \tag{4.13}$$

If we write the voltages in terms of true equivalent fields, $V(\omega) = H(\omega)/\gamma(\omega)$ and $N(\omega) = H^N(\omega)/\gamma(\omega)$, where $H^N(\omega)$ is equivalent magnetic noise in the power detector, for probes A and B, we have

$$H_A^a(\omega) = [1 + \epsilon_A(\omega)][H(\omega) + H_A^N(\omega)] \tag{4.14}$$

$$H_B^a(\omega) = [1 + \epsilon_B(\omega)][H(\omega) + H_B^N(\omega)] \tag{4.15}$$

We have assumed that the signal at each probe is the same and the noise at each probe is independent. Since the calibration errors are unknown, the coherence function $\gamma^2(\omega)$ is used to estimate the noise [79]. In signal procesing, the coherence is a statistic that can be used to examine the relation between two signals or data sets. It is commonly used to estimate the power transfer between input and output of a linear system. For probes A and B mentioned above, $\gamma^2(\omega)$ is

$$\gamma^2(\omega) = \frac{|\langle H_A^a H_B^{a^*} \rangle|^2}{\langle H_A^a H_A^{a^*} \rangle \langle H_B^a H_B^{a^*} \rangle} \tag{4.16}$$

A and B represent two time dependent signals separated at different times. With the same assumption, that in each probe the signal is the same and the noise is independent, we have

$$\gamma^2(\omega) = \frac{\langle HH^* \rangle^2}{(\langle HH^* \rangle + \langle H_A^N H_A^{N^*} \rangle)(\langle HH^* \rangle + \langle H_B^N H_B^{N^*} \rangle)} \tag{4.17}$$

If we define $x(\omega)$ as the noise to output power ratio for each probe, we have

$$x(\omega) = \frac{\langle H_A^N H_A^{N^*} \rangle}{(\langle HH^* \rangle + \langle H_A^N H_A^{N^*} \rangle)} = \frac{\langle H_B^N H_B^{N^*} \rangle}{(\langle HH^* \rangle + \langle H_B^N H_B^{N^*} \rangle)} \tag{4.18}$$

Using (4.18), we can write

$$\langle HH^* \rangle^2 = [1 - x(\omega)]^2 (\langle HH^* \rangle + \langle H_A^N H_A^{N^*} \rangle)(\langle HH^* \rangle + \langle H_B^N H_B^{N^*} \rangle) \tag{4.19}$$

Comparing (4.17) and (4.19) results in the following relation between $\gamma(\omega)$ and $x(\omega)$

$$\gamma(\omega) = [1 - x(\omega)] \tag{4.20}$$

$$V_\omega = H^N(\omega)/\gamma(\omega) \tag{4.21}$$

Since for the microwave power detectors the relation between the input power and the output voltage is relatively independent of the frequency (for example Fig. 4 in [72]), we have

$$\gamma^2(\omega) S_{V_N}(\omega) = S_{H^N}(\omega) \tag{4.22}$$

Moreover, according to (4.6), there is a linear relation between the reconstructed currents and the measured magnetic field. Thus, using (4.22) and knowing the noise spectrum of output voltage of the microwave power detector, we can obtain the noise spectrum of the calculated currents.

4.4 Adaptive sampling algorithm in planar near-field antenna measurement

The proposed adaptive algorithm starts with a small number of initial scan points that are distributed uniformly across the measurement plane. These initial points and the sequentially added points are used to characterize the overall near-field pattern of the AUT. A balanced tradeoff between the two criteria, exploration and exploitation, is required. Exploration means searching the scanning area to locate the main regions that have not been spotted yet. The purpose of exploration is to ensure that the points spread over the measurement area evenly, while exploitation is the act of focusing on the areas that are highly dynamic and require finer sampling resolution.

The proposed method is a balanced combination of both criteria. It starts by computing a small number of initial scan points, and most of the data points are added adaptively. For the exploration criterion, the density of the samples is determined by computing a Cartesian rectangular grid of data points and calculating the area of each cell. For the exploitation, the field variation is quantified by computing the linear approximation of the fields at the data points and comparing the approximated and true values. These two criteria are combined as a metric function to rank the data points according to their dynamic variation of near-field pattern at their locations. The highly ranked points represent the areas that require additional data points. This process continues sequentially until the termination criterion is satisfied.

4.4.1 Exploration

To evaluate the density of data points, the measurement area is divided into square cells, and each data point is at the center of a square. Cells with a large area compared to other cells represent the regions that are sampled sparsely. Thus, for each sample point, p_k, the area of the corresponding cell, $V(C_k)$, is compared to the area of the other cells using the following relation [53]

$$V(p_k) = \frac{Vol(C_k)}{(Vol(C_1) + Vol(C_2) + ... + Vol(C_k))} \tag{4.23}$$

$V(p_k)$ denotes the portion of the scan area that contains point p_k.

4.4.2 Exploitation

To localize the areas with a strongly varying near-field pattern, first for each p_k, a set of neighboring points, $N(p_k)$ is chosen. These neighbors are located at the center of the rectangles that have any overlap with the cell of p_k. These neighbors are used to calculate the gradient $\nabla|H(x, y)|$

$$\nabla|H(x,y)| = (\frac{\partial|H(x,y)|}{\partial x}, \frac{\partial|H(x,y)|}{\partial y}) \tag{4.24}$$

This gradient characterizes the local linear approximation $\tilde{H}(x,y)$ at p_k, as,

$$\tilde{H}(x,y)| = |H(x,y)| + (\nabla|H(x,y)|)_{p_k}(p - p_k) \tag{4.25}$$

Consider that $(\nabla|H(x,y)|_{p_k}) = A^{-1}b$ is calculated by fitting a hyperplane through point p_k, based on its V neighbors $\{p_{kv}\}_{v=1}^{V}$,where

$$A = \begin{pmatrix} x_{k_1} - x_k & y_{k_1} - y_k \\ x_{k_2} - x_k & y_{k_2} - y_k \\ ... & ... \\ x_{k_v} - x_k & y_{k_v} - y_k \end{pmatrix}$$

$$b = [|H(p_{k_1})| \quad |H(p_{k_2})| \quad ... \quad |H(p_{k_v})|]^T$$

Once the local linear approximation of the dynamic behavior of the near-field pattern is calculated using (4.24) the estimated value of the field at p_k is compared with the true value

$$\bar{W}(p_k) = \sum_{v=1}^{V} ||\tilde{H}(p_k)| - H(p_k)| \tag{4.26}$$

A large value of $\bar{W}(p_k)$ indicates that the field is varying rapidly at this area. A normalized metric is used to describe the dynamic variation of the field near the coordinate p_k to that of the other points [53]

$$W(p_k) = \frac{\bar{W}(p_k)}{(\bar{W}(p_1) + \bar{W}(p_2) + ... + \bar{W}(p_k))} \tag{4.27}$$

4.4.3 Adaptive data sampling selection

A combination of exploration and exploitation criteria is used as a global metric, $G(p_k)$, to rank the sampled data points [54].

$$G(p_k) = (1 + V(p_k))(1 + W(p_k)) \tag{4.28}$$

High value of $G(p_k)$ indicates that the region associated to p_k is undersampled, and more data points must be added in this area.

4.4.4 Measurement and simulation results

To evaluate the proposed approach, a multi-band antenna is designed and fabricated to analyze methods in various frequencies. The fabricated AUT and its $|S_{11}|$ are shown in Fig. 4.2 . The design process of this antenna is explained in [81]. Since the frequency range of RFX2 is approximately 1∼6GHz, the near-field of the AUT is measured at 1.5GHz, 3.5GHz, and 4.75GHz to evaluate the performance of the interpolation and adaptive sampling techniques. First, as mentioned in section 5.2, since in RFX2 at every sampling point only X or Y component of the magnetic field is measured alternately and the other component is estimated numerically, the performance of the averaging, linear, nearest, and natural neighbor interpolations is evaluated for different levels of noise. It is mentioned in section 5.3 that the power stability of the detector is confined by the flicker floor; thus the input noise is assumed to be random data with the same spectral density as flicker noise (Fig. 4.3).

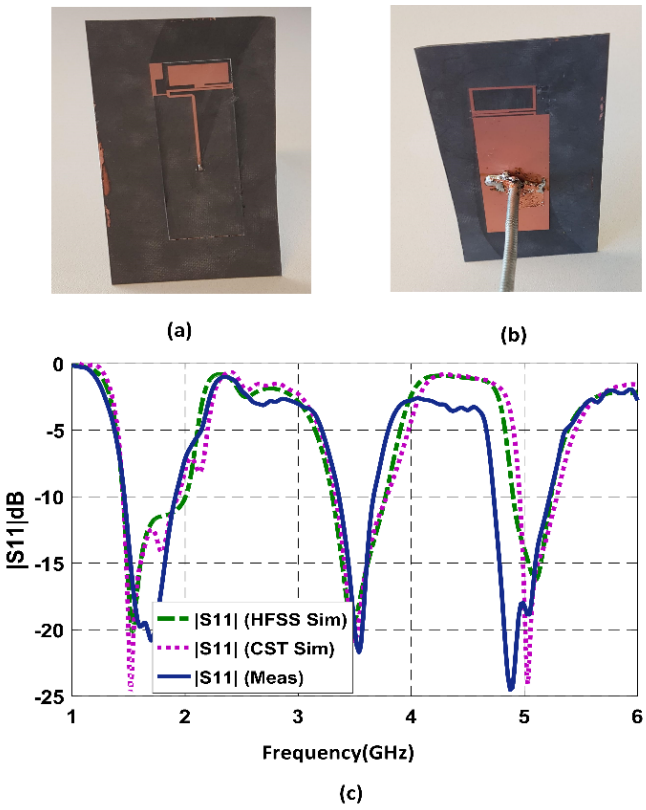

Fig. 4.2: Photograph of the planar antenna and its return loss and. (a) Front view of the antenna. (b) Back view of the antenna. (c) $|S_{11}|$ of the antenna simulated using HFSS and CST, and measured result.

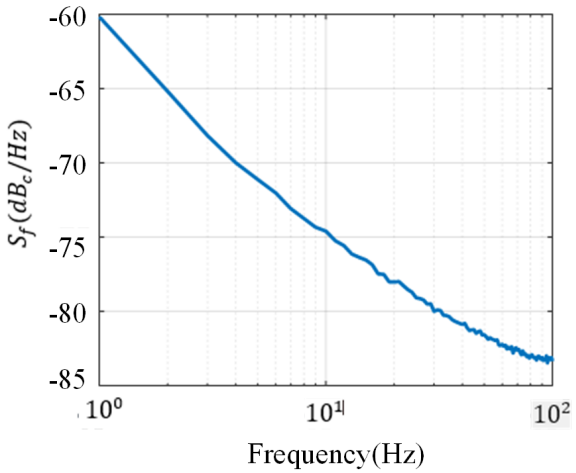

Fig. 4.3: The spectral density of flicker noise.

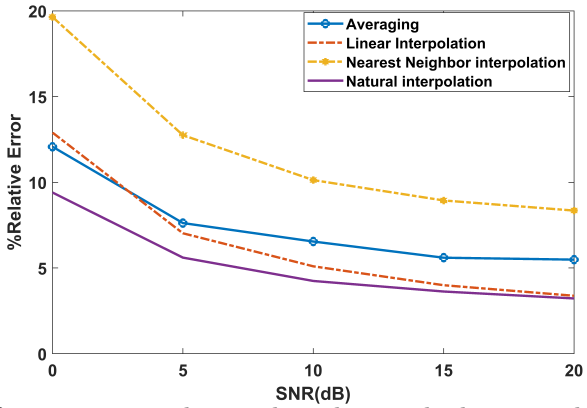

Fig. 4.4: Relative error of various interpolation algorithm methods versus different values of SNR(dB).

The sampled data are extracted from HFSS such that at every point only X or Y component of the magnetic field is available. The modeled noise is added to the data and the interpolation techniques are utilized to estimate the values of the component of magnetic field for which there is no sample. Thereafter, the estimated values are compared to the exact values that are obtained from full-wave simulation. The results are depicted in Fig. 4.4. The nearest neighbor interpolation has the worst accuracy while the natural neighbor method is a proper candidate for this purpose. As indicated in section 4.2, it can be explained according to the continuity of the interpolant and its derivative in the natural interpolation method. Second, the accuracy and validity of the adaptive sampling approach are investigated. As it is shown in Fig. 4.5, the algorithm starts from a small number of uniformly distributed samples (e.g., 25 samples). This algorithm sequentially focuses on the area with strongly varying near-field pattern and skip the regions that have smooth behavior. Clearly, by increasing the number of samples, more accurate results will be obtained. A comparison between the uniform sampling and adaptive sampling is presented in Table 4.1, in terms of the number of samples, relative error, NF-FF simulation time, and estimated single-probe measurement time.

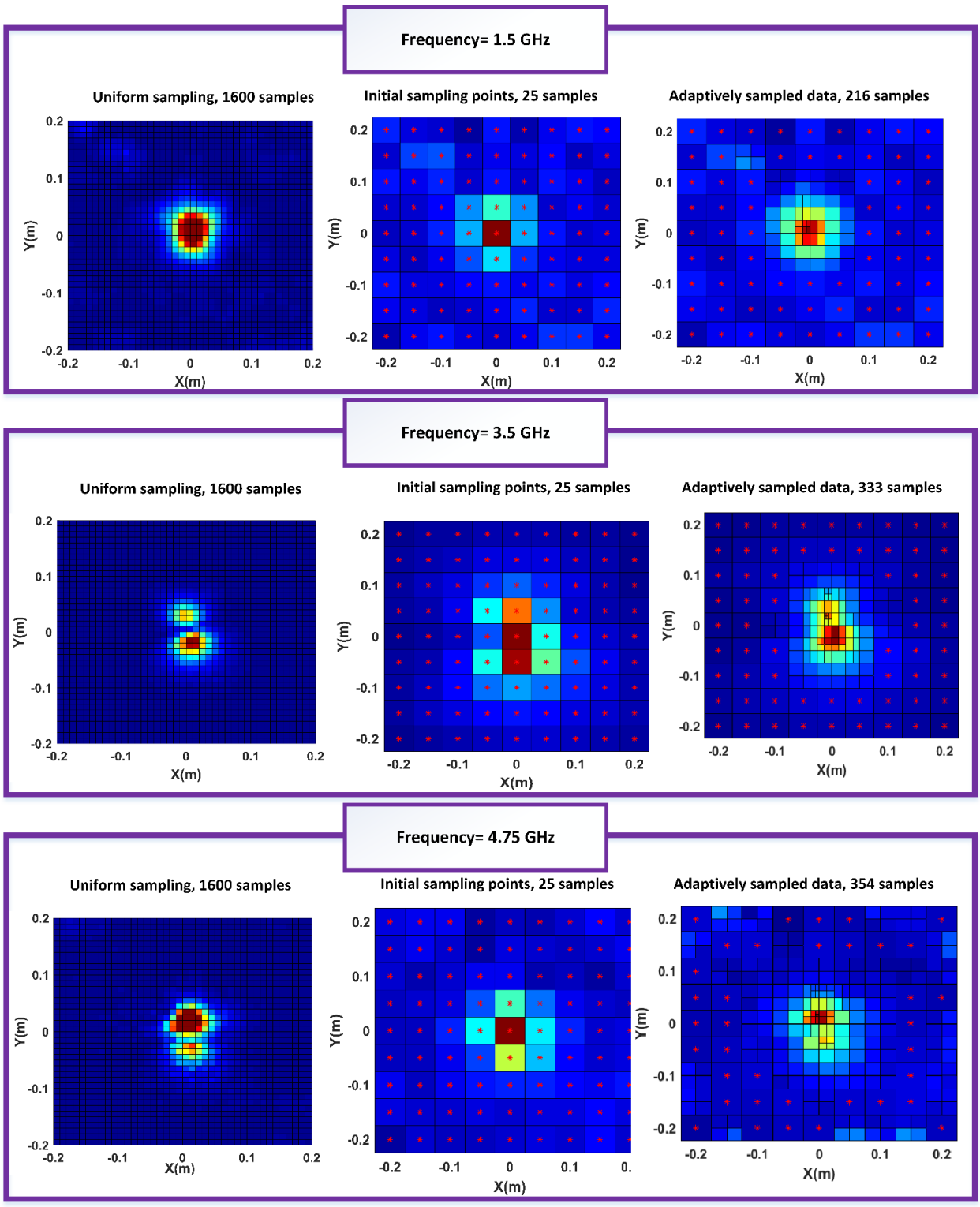

Fig. 4.5: The uniformly and adaptively sampled near-field of the AUT, and the initial samples for the adaptive algorithm, in three frequencies, 1.51GHz, 3.5GHz, and 4.75GHz.

To calculate the error, the reconstructed currents are used to calculate the magnetic fields over a plane that is 0.1λ away from the measurement plane. The reconstructed values are compared with the values extracted from the full-wave simulation. The relative error is calculated as

$$relative\ \ error = \frac{||H_{x,y}^{Full-wavesim} - H_{x,y}^{reconstructed}||}{||H_{x,y}^{Full-wavesim}||} \tag{4.29}$$

As it can be seen in Table 4.1 at 3.5GHz, the uniform sampling with 1600 sample points results in 10% error and the NF-FF transformation algorithm takes about 15 minutes to be completed while for the adaptive algorithm with 348 sample points, the error is 10% and only the NF-FF transformation takes only 1 minute. It is worth mentioning that this comparison is a single frequency measurement over one plane. If the measurements for several frequencies and planes are required, the required time increases drastically in case of uniform sampling. The estimated single probe measurement time in Table 4.1 is calculated based on the timing that is shown in Fig. 2.7. As it is depicted in Fig. 2.7, for multiple channels and frequencies the measurement time increases significantly. If we assume 15 seconds for the step axis motion plus scan setup time as mentioned in [82], for a single frequency and channel, changing the number of samples from 1600 to 348 is equal to a huge reduction of the required time from 6.6 hours to 1.4 hours for single probe measurement.

Table 4.1: The comparison between the uniform and adaptive sampling techniques for the near-field of the AUT at 3.5GHz

Sampling Technique	Number of samples	Estimated Single Probe Measurement Time	Relative Error (%)	NF-FF Simulation Time
Uniform Sampling	1600	6.6 hours	10%	15min
Adaptive Sampling	348	1.5 hours	10%	1min

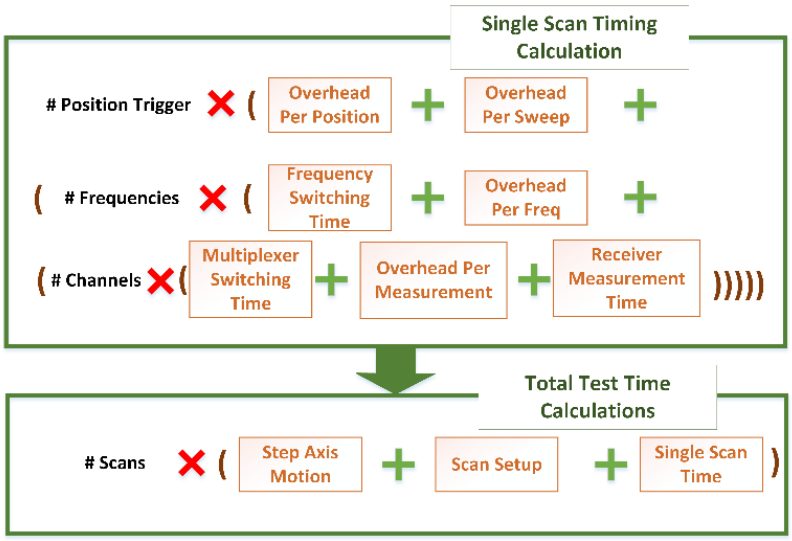

Fig. 4.6: Single scan and total test time calculation in case of a single probe measurement [82].

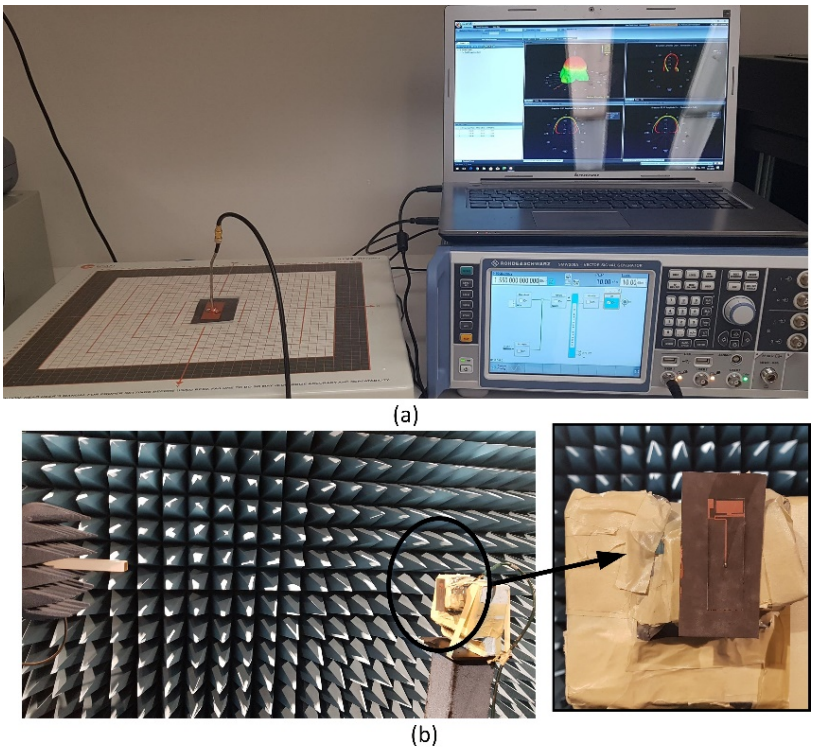

Fig. 4.7: The antenna measurement setups. (a) Near-field measurement using an RFX2. (b) Measurement setup in an anechoic chamber including the AUT and the waveguide probe.

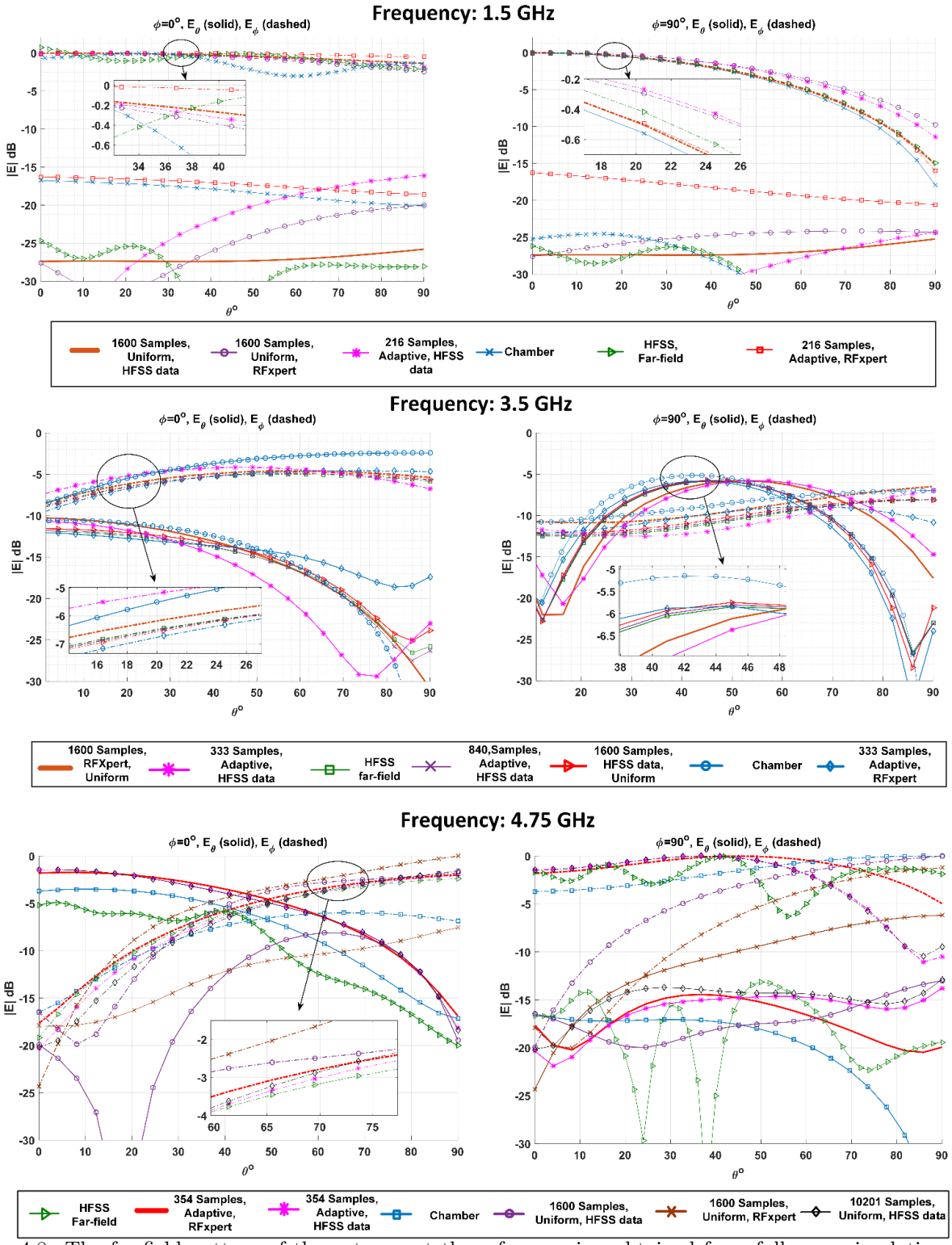

Fig. 4.8: The far-field pattern of the antenna at three frequencies, obtained from full-wave simulation and various measurement and sampling techniques.

In the next step, the sampled and measured near-fields along with the SRM are used to calculate the far-field pattern of the antenna. The measurement setups using both the RFX2 and anechoic chamber are shown in Fig. 4.7. The natural neighbor interpolation is used to interpolate the data at the newly added sample points as well as the second component of the tangential magnetic field at the location of each probe. The calculated far-field patterns are shown in Fig. 4.8. The results for 4.75GHz show that even with 1600 samples (the number of RFX2 probes) the far-field pattern is not accurate, and 10201 samples with 2mm sampling resolution are required to have an acceptable far-field pattern while for the adaptive algorithm only 354 samples are required. Finally, the performance of linear, nearest and natural neighbor interpolation techniques to calculate the value of sequentially added samples is assessed for different SNR levels, as can be seen in Fig. 4.9. Again, the natural neighbor interpolation outperforms the other methods because of the continuity of the interpolant and its derivative.

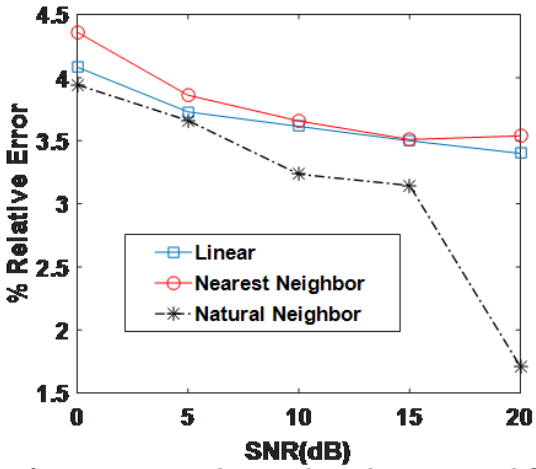

Fig. 4.9: Relative error of various interpolation algorithms versus different values of SNR(dB).

4.5 Adaptive data acquisition and clustering technique in spherical near-field antenna measurement

The proposed adaptive algorithm starts with a small number of initial scan points that are distributed uniformly over the measurement sphere. These initial points and the sequentially added points are used to characterize the overall near-field pattern of the AUT. A balanced tradeoff between the two criteria, exploration and exploitation, is required. Exploration means searching the scanning area to locate the main regions that have not spotted yet. The purpose of exploration is to ensure that the points spread over the measurement area evenly, while exploitation is the act of focusing on the areas that are highly dynamic and require finer sampling resolution. The proposed method is a balanced combination of both criteria. It starts by computing a small number of initial scan points and most of the data points are added adaptively. For the exploration criterion, the density of the samples is determined by computing a Voronoi Tessellation of data points and calculating the area of each cell. For the exploitation, the field variation is quantified by computing the variation of the field in spherical coordinate system. These two criteria are combined as a metric function to rank the data points according to their dynamic variation of near-field pattern at their locations. The highly ranked points represent the areas that require additional data points. This process continues sequentially until the termination criterion is satisfied.

4.5.1 Exploration

To evaluate the density of data points, the measurement area is divided into Voronoi Tessellatioin. and each data point is at the center of a cell. Cells with a large area compared to other cells represent the regions that are sampled sparsely. Thus, for each sample point, p_k, the area of the corresponding cell, $V(C_k)$, is compared to the area of the other cells using the following relation

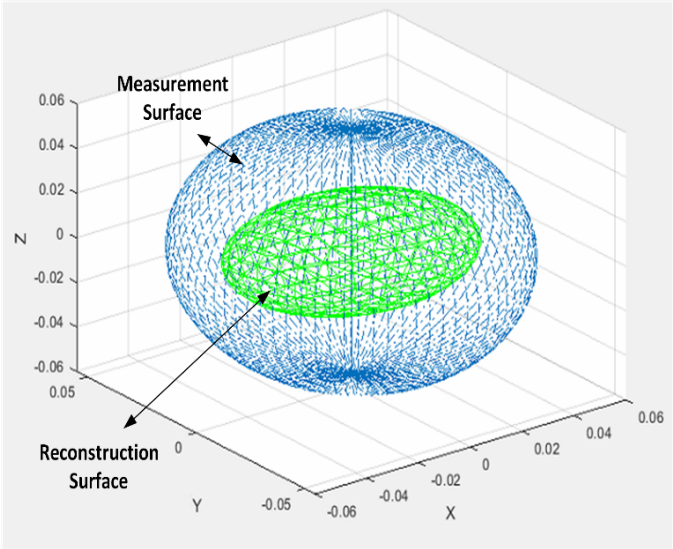

Fig. 4.10: Schematic representation of the source reconstruction method.

$$V(p_k) = \frac{Vol(C_k)}{(Vol(C_1) + Vol(C_2) + ... + Vol(C_k))} \tag{4.30}$$

$V(p_k)$ denotes the portion of the scan area that contains point p_k.

4.5.2 Exploitation

To localize the areas with a strongly varying near-field pattern, first for each p_k, a set of neighboring points, $N(p_k)$ are chosen. These neighbors are in the cells that have at least one common edge with the cell of p_k. These neighbors are used to calculate the gradient $\nabla|x_{(1,2)}|$

$$\bar{W}(p_k) = |\nabla x_{(1,2)}| = \sqrt{(\frac{\partial x_{(1,2)}}{\partial \theta})^2 + \frac{1}{sin^2\theta}(\frac{\partial x_{(1,2)}}{\partial \phi})^2} \tag{4.31}$$

where x is the θ and ϕ component of the measured field over the sphere. A large value of $\bar{W}(p_k)$ indicates that the field is varying rapidly at this area. A normalized metric is used to describe the dynamic variation of field near the p_k:

$$W(p_k) = \frac{\bar{W}(p_k)}{(\bar{W}(p_1) + ... + \bar{W}(p_k))} \tag{4.32}$$

4.5.3 Adaptive data sampling selection

A combination of exploration and exploitation criteria is used as a global metric, $G(p_k)$, to rank the sampled data points.

$$G(p_k) = (1 + V(p_k))(1 + W(p_k)) \tag{4.33}$$

High value of $G(p_k)$ indicates that the region associated to p_k is undersampled, and more data points should be added in this area.

Once the near-field data is collected the euivalent currents are reconstructed over a sphere that encloses the antenna (Fig. 4.10).

4.5.4 Measurement and simulation results

To verify the proposed algorithm, an antenna with operating frequency of 8GHz is tested. The size of the antenna is 19.5 cm $\times$ 19.5 cm. The measuring probe is placed at the distance of 108 cm from the antenna. The near-field data is measured with the resolution of $\Delta\theta = \Delta\phi = 0^o$, that means 3200 samples. The near-field radiation pattern of the antenna as well as the data points for the uniform and adaptive sampling are depicted in Fig. 4.11. Using the adaptive algorithm, the number of the required samples for the same accuracy is 426 that means the significant reduction of the needed data points. In this paper, the points derived from the adaptive algorithm are interpolated from the uniformly measured data using the cubic spline interpolation method. To determine the proper data points for interpolation at every newly added data, the uniformly measured data are clustered by k-means clustering technique which is a simple unsupervised machine learning algorithm that categorizes a dataset into a number (k) of clusters. This number is determined by the user. The algorithm clusters the data into k clusters, even if k is not the optimal number of clusters. Therefore, when using k-means clustering, users need to decide whether they are using the right number of clusters. One method to validate the number of clusters is the *elbow method* [92] as shown

in Fig. 4.12 (a). The idea of the elbow method is to perform k-means clustering on the dataset for a range of values of k (e.g., k from 1 to 9 here), and for each value of k calculate the sum of squared distances of samples to the nearest cluster center. If the plot looks like an arm, then the elbow on the arm is optimal k. As shown in Fig. 4.12 (a) the optimal number of clusters is 5 here. The clustered data are shown in Fig. 4.12 (b) and Fig. 4.12 (c) in XYZ coordinate system and θ and ϕ plane. Thus, the values of each clusters are used to estimate the value of newly added sample. The symmetry of the pattern helps us to reduce the number of data points are used for interpolation. The uniformly measured data and the adaptively selected samples are used to reconstruct the far-field pattern of the antenna. As demonstrated in Fig. 4.13 the results are very close that confirms the validity of the proposed algorithm.

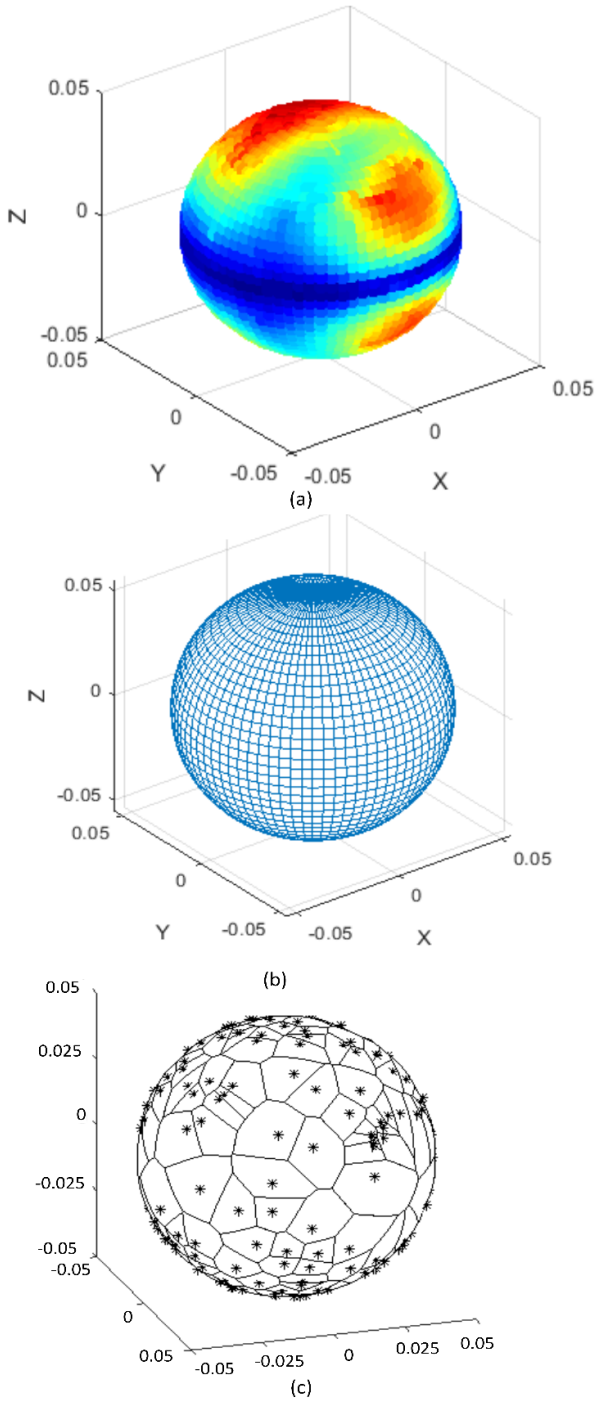

Fig. 4.11: Near -field radiation of the antenna under test and different sampling algorithms. (a) Near-field radiation. (b) Uniform sampling. (c) Adaptive sampling.

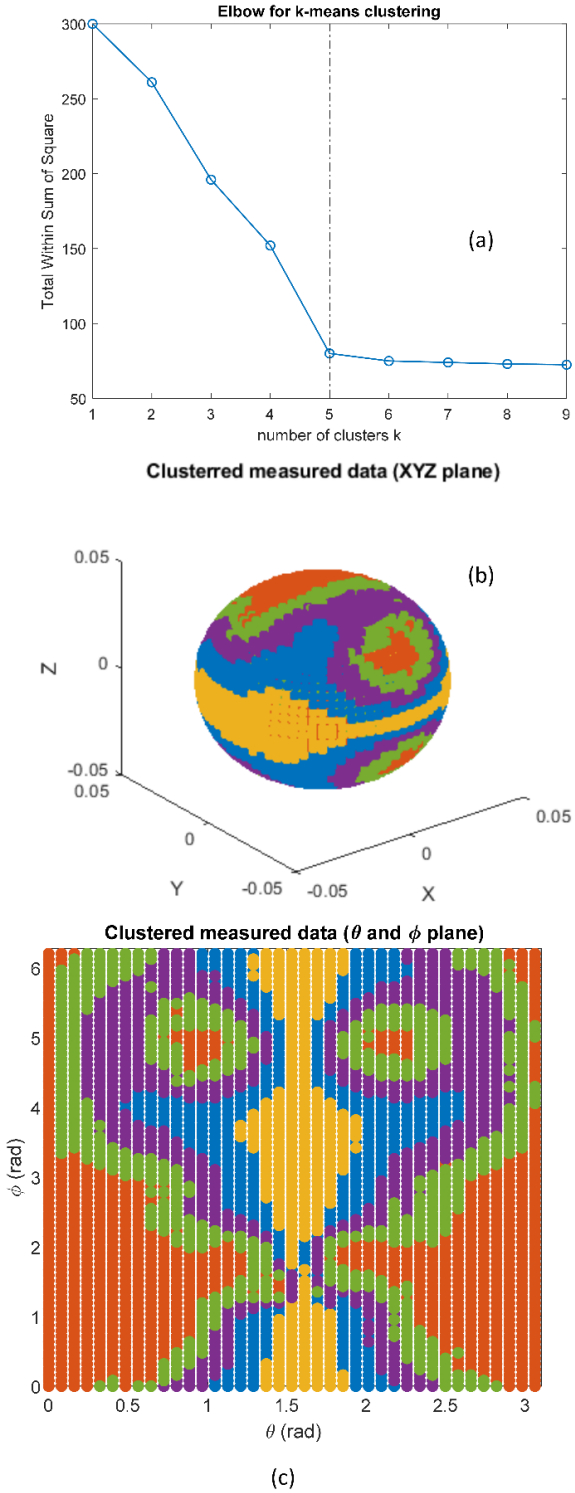

Fig. 4.12: Clustering the measured near-field. (a) Elbow method to determine the optimal number of clusters. (b) Clustered data over XYZ plane. (c) Clustered data over θ and *phi* plane.

(a)

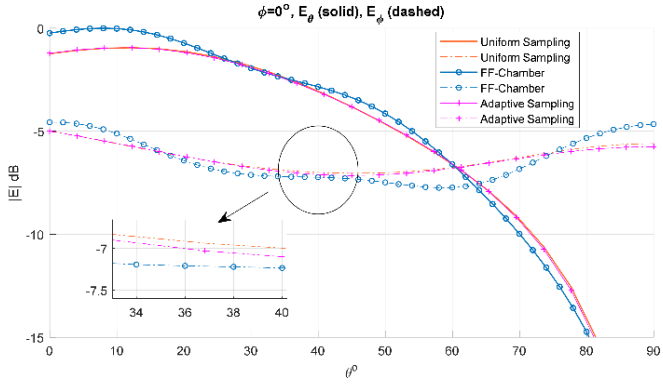

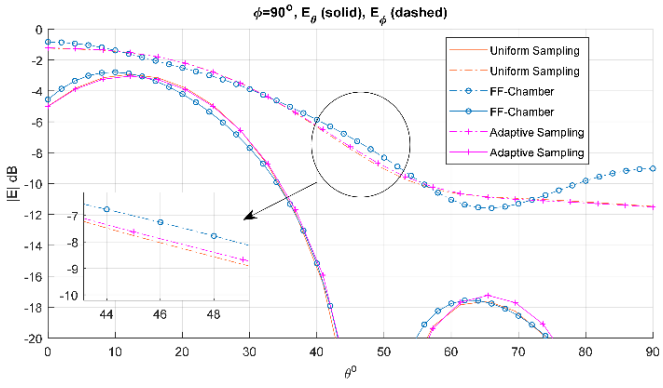

(b)

Fig. 4.13: Spherical near-field measurement setup and far-field pattern of antenna. (a) Measurement setup. (b) Far-field pattern of the antenna.

4.6 Conclusion

In this chapter, a new approach is presented to improve the accuracy and speed of the planar near-field measurement of antennas. The near-field measurements are performed using RFX2 probe array and a microwave power detector which converts the input power to an output voltage. For modeling the noise of magnetic fields in the reconstruction calculations, the relation between the noise of the input power and the output voltage has been extracted analytically. Since in the RFX2 at each probe only one component of magnetic field is measured, the accuracy of various interpolation techniques to estimate the other component has been evaluated and the natural neighbor method was found as the best candidate compared to the linear, averaging and nearest neighbor approaches. Thereafter, an adaptive sampling technique is proposed that sequentially adds more data points for the regions with high dynamic behavior. This approach results in the significant reduction of the required samples (e.g., from 1600 to 333 samples). Finally, the adaptive algorithm along with the natural neighbor interpolation and SRM are used to calculate the far-field pattern of AUT. An adaptive sampling algorithm is also extended to spherical near-field measurement of antennas. Instead of square cells, Voronoi tessellation cells are used to discretize the measurment surface. The algorithm starts with an iniitial set of randomly distributed sample points, calculates the field variation at the data points, and sequentially focuses on the areas with highly dynamic near-field radiation. Since this approach can be applied to the uniformly measured data, the value of adaptively found samples should be interpolated. To have accurate interpolated results, the uniformly measured data is clustered using k-means algorithm. The optimum number of clusters is determined using elbow method. In the spherical near-field measurement the number of samples reduced from 3200 to 426 by utilizing the adaptive algorithm. The accuracy and validity of the proposed methods are confirmed using the numerical and measurement results. The results show that for much less numbers of samples, the same accuracy can be achieved.

Chapter 5

Conclusion and Future Work

5.1 Conclusion

This thesis is focused on the methods that enhance the speed and accuracy of source reconstruction, sampling, and fault detection algoritms. The research work includes both measurment and modelling techniques.

In chapter 2, a relation is developed between the RWG and LCN method in the application of the near-field measurement of the antenna. The proposed model preserves the current continuity and, as a result, is more accurate compared to LCN and requires less DOFs leading to a faster and more robust solution. Moreover, this point-based approach is a proper candidate to be accelerated using MLFMM and utilized in real-time applications.

In chapter 3, a high-resolution near-field measurement along with the source reconstruction method is used to reconstruct the magnetic field close to the SIW structures and detect the defective vias. The distance at which the sufficient resolution to resolve two adjacent defective vias is derived analitically by modeling the defective vias with the apertures. The proposed methods are validated using single probe and probe array measurements. Finally, a machine learning algorithm is proposed that classifies the reconstructed fields based on the field and material variation, so different radiation sources can be distinguished.

In chapter 4, an adaptive sampling algorithm is proposed for the planar near-field mea-

surement that sequentially focuses on the areas with highly dynamic near-field behavior. The proposed technique significantly reduces the number of the measurement points and the time of the measurement. Also, since the interpolation algorithms should be used to calculate the field at those points, there is no measured value for them, and the accuracy of various interpolation techniques in the presence of different levels of noise is investigated.

5.2 Suggestions for Future Work

In this study, firstly, the RWG-via-LCN algorithm is developed to accelerate the back projection method using MLFMM that is widely used to accelerate MoM, especially in scattering problems. In [13] it is mentioned that when this method is applied to Galerkin-based MoM, the efficiency is limited by the size of the basis functions. Generally, in MLFMM, near interactions are calculated exactly, while for far interactions multipole expansion of current distribution is used. In this method, a big cube encompasses the scatterer. This cube is then divided into eight smaller ones, and this procedure continues until the size of the smallest cube and, therefore, the size of the lowest level is several times of the longest mesh edge. For example, for a RWG basis function, the edge length is about 0.1λ; therefore, the smallest cube size is about a quarter of a wavelength. Also, FMM is used in near-field measurements to speed up the process [25]. As mentioned in [25], in MoM, for the finest level of FMM groups, the support of basis functions is not small enough, so the basis functions are subdivided into quadrature points; then the effect of quadrature points is collected. Thus, it is clear that point-based methods such as LCN are more appropriate for acceleration by MLFMM than MoM method. The proposed method in chapter 2 combines this advantage of LCN method with the benefit of current continuity of RWG MoM. Thus, as future work, MLFMM can be applied to RWG-via-LCN.

The fault detection along with the machine learning algorithm can be developed for different types of circuit such as phased arrays, sensors [93]- [96], and corrugated structures [97]- [99] wherein other physical and electromagnetic parameters can be used for classification.

The adaptive sampling technique can be applied to cylindrical and spherical measurement with one or multiple probes in which the implementation of a greedy optimization algorithm might be required to minimize the distances the probe traces.

The NF-FF and fault detection algorithms can be implemented for mmWave device characterization. For example, a vector network analyzer (VNA) is typically used in near-field measurements because both phase and amplitude information is required for the NF-FF transformations. However, mmWave 5G devices are single-ended and do not support the use of a VNA. The high level of integration between the radio and antenna array means that characterization of only the device antenna may not be possible due to the lack of connectors. For instance, one or more antennas can be fixed to provide a reference for phase recovery while the other(s) perform a near-field scan. The relative phases measured by the two sets of antennas are then utilized in the far-field transformation.

Chapter 6

List of Publications

6.1 Journals

1. R. R. Alavi, Ali Kiaee, R. Rashid Mirzavand, and P. Mousavi , "RWG MoM-via-locally corrected Nyström method in near-field to far-field transformation using very-near-field measurement, " *IET Microwaves, Antennas and Propagation.*, vol. 12, no. 2, pp. 145–153, Sep. 2017.

2. R. R. Alavi, R. Rashid Mirzavand, Ali Kiaee and P. Mousavi , "Accuracy and Time Enhancement of Near-Field Antenna Measurement Considering Noise, Using an Adaptive Data Acquisition and Interpolation Technique, " *IEEE Trans. Antennas Propag.*, Rejected and Resubmission.

3. R. R. Alavi, R. Rashid Mirzavand, A. Kiaee, R. Patton and P. Mousavi , "Detection of the Defective Vias in SIW Circuits from Single/Array Probe(s) Data Using Source Reconstruction Method and Machine Learning, " *IEEE Trans. Microw. Theory Techn.*, Major Revision.

4. A. Kiaee, R. R. Alavi, R. Mirzavand, and P. Mousavi, "Numerical and experimental assessment of source reconstruction for very near-field measurements with an array of H-field probes," *IEEE Trans. Antennas Propag.*, vol. 12, no. 2, pp. 145–153, 2018.

5. A. Kiaee, R. Patton, R. R. Alavi, B. Alavikia R. Mirzavand, and P. Mousavi, "First Order Correction and Equivalent Source Reconstruction Assessment for Practical," *IEEE Trans. Antennas Propag.*, Major Revision.

6. R. R. Alavi, R. Mirzavand, and P. Mousavi, "An Adaptive Data Acquisition and Clustering Technique to Enhance the Speed of Spherical Near-Field Antenna Measurements," *IEEE Antenna and Wireless Propagation Letter.*, reject and resubmit.

6.2 Conferences

1. R. R. Alavi, A. Kiaee, R. Mirzavand, and P. Mousavi, "Linear-linear basis functions for source reconstruction using magnetic-field integral equations in very-near-field measurements," in *2017 IEEE International Symposium on Antennas and Propagation*, 2017, pp. 1559–1560.

2. R. R. Alavi, A. Kiaee, R. Mirzavand, R. Patton, and P. Mousavi, "A High- Resolution Approach to Extract the the Emissions from a Circuit Board Using the Magnitude-Only Near-Field Measurement," in *2018 IEEE International Symposium on Antennas and Propagation*, 2018, pp. 1387–1388.

3. R. R. Alavi, A. Kiaee, R. Mirzavand, and P. Mousavi, "Locally corrected Nyström technique and its relationship with RWG method of moment for current reconstruction using very-near-field measurements," in *2017 11th European Conference on Antennas and Propagation (EUCAP)*, 2017, pp. 319–323.

4. A. Kiaee, R. R. Alavi, M. M. Honari, R. Mirzavand, and P. Mousavi, "Ground de-embedded source reconstruction using a planar array of H-field probes," in *2017 IEEE International Symposium on Antennas and Propagation*, 2017, pp. 133–134.

5. R. R. Alavi, A. Kiaee, R. Mirzavand, and P. Mousavi, "Extraction of Via Defects from Very-Near-Field Measuremets and A Source Reconstruction Method," in *2nd URSI*

AT-RASC Gran Canaria, 2018.

6. R. R. Alavi, R. Mirzavand, R. Patton, and P. Mousavi, "Fast and Accurate Near-Field to Far-Field Transformation Using an Adaptive Sampling Algorithm and Machine Learning," in *2019 IEEE International Symposium on Antennas and Propagation*, 2019,*Honorable Mention*.

Bibliography

[1] R. C. Johnson, H. A. Ecker, and J. S. Hollis, "Determination of far-field antenna patterns from near-field measurements," Proc. IEEE, vol. 61, no. 12, pp. 1668–1694, Dec. 1973.

[2] J. J. H. Wang, "An examination of the theory and practices of planar near-field measurement," *IEEE Trans. Antennas Propag.*, vol. 36, no. 6, pp. 746–753, 1988.

[3] P. Petre and T. K. Sarkar, "Differences between modal expansion and integral equation methods for planar near-field to far-field transformation (Summary)," *J. Electromagn. Waves Appl.*, vol. 10, no. 2, pp. 269–271, 1996.

[4] D. Baudry et al., "Plane wave spectrum theory applied to nearfield measurements for electromagnetic compatibility investigations," *IET Sci. Meas. Technol.*, vol. 3, no. 1, pp. 72–83, 2009.

[5] C. H. Schmidt, M. M. Leibfritz, and T. F. Eibert, "Fully Probe-Corrected Near-Field Far-Field Transformation Employing Plane Wave Expansion and Diagonal Translation Operators," IEEE Trans. Antennas Propag., vol. 56, no. 3, pp. 737–746, 2008.

[6] E. Joy and D. Paris, "Spatial sampling and filtering in near-field measurements," *IEEE Trans. Antennas Propag.*, vol. 20, no. 3, pp. 253–261, 1972.

[7] P. Petre and T. K. Sarkar, "Planar near-field to far-field transformation using an equivalent magnetic current approach," *IEEE Trans. Antennas Propag.*, vol. 40, no. 11, pp. 1348–1356, 1992.

[8] Y. A. Lopez, F. L.-H. Andres, M. R. Pino, and T. K. Sarkar, "An Improved Super-Resolution Source Reconstruction Method," *IEEE Trans. Instrum. Meas.*, vol. 58, no. 11, pp. 3855–3866, 2009.

[9] Schmidt, C.H., Eibert, T.F.: "Near-field to far-field transformation utilising multilevel plane wave representation for planar and quasi-planar measurement contours", IET Microw. Antennas Propag., 2010, 4, (11), pp. 1829–1837

[10] Y. Alvarez, F. Las-Heras, and M. R. Pino, "Reconstruction of Equivalent Currents Distribution Over Arbitrary Three-Dimensional Surfaces Based on Integral Equation Algorithms," *IEEE Trans. Antennas Propag.*, vol. 55, no. 12, pp. 3460–3468, 2007.

[11] L. J. Foged, L. Scialacqua, F. Saccardi, J. L. A. Quijano, G. Vecchi, and M. Sabbadini, "Practical Application of the Equivalent Source Method as an Antenna Diagnostics Tool [AMTA Corner]," *IEEE Antennas Propag. Mag.*, vol. 54, no. 5, pp. 243–249, 2012.

[12] L. Gürel, K. Sertel, and İ. K. Şendur, "On the choice of basis functions to model surface electric current densities in computational electromagnetics," *Radio Sci.*, vol. 34, no. 6, pp. 1373–1387, 1999.

[13] K. C. Donepudi, J. Song, J.-. Jin, G. Kang, and W. C. Chew, "A novel implementation of multilevel fast multipole algorithm for higher order Galerkin's method," *IEEE Trans. Antennas Propag.*, vol. 48, no. 8, pp. 1192–1197, 2000.

[14] M. Vikram, H. Huang, B. Shanker, and T. Van,"A Novel Wideband FMM for Fast Integral Equation Solution of Multiscale Problems in Electromagnetics,"*IEEE Trans. Antennas Propag.*, vol. 57, no. 7, pp. 2094–2104, 2009.

[15] M. Al-Qedra, P. Saleh, F. Ling, and V. Okhmatovski, "Barnes-Hut Accelerated Capacitance Extraction Via Locally Corrected Nyström Discretization," *2006 IEEE Electrical Performane of Electronic Packaging*, 2006, pp. 107–110.

[16] R. Coifman, V. Rokhlin, and S. Wandzura, "The fast multipole method for the wave equation: a pedestrian prescription," *IEEE Antennas Propag. Mag.*, vol. 35, no. 3, pp. 7–12, 1993.

[17] Andrew F. Peterson and Malcolm m. Bibby. An Introduction to the Locally Corrected Nyström Method.(2009, November 8). Networks. (2nd ed.) [Online].

[18] S. D. Gedney, "On deriving a locally corrected Nyström scheme from a quadrature sampled moment method," IEEE Trans. Antennas Propag., vol. 51, no. 9, pp. 2402–2412, Sep. 2003.

[19] M. Shafieipour, I. Jeffrey, J. Aronsson, and V. I. Okhmatovski, "On the Equivalence of RWG Method of Moments and the Locally Corrected Nyström Method for Solving the Electric Field Integral Equation," *IEEE Trans. Antennas Propag.*, vol. 62, no. 2, pp. 772–782, 2014.

[20] M. Shafieipour, J. Aronsson, I. Jeffrey, and V. I. Okhmatovski, "Exact Relationship Between the Locally Corrected Nyström Scheme and RWG Moment Method for the Mixed-Potential Integral Equation," *IEEE Trans. Antennas Propag.*, vol. 63, no. 11, pp. 4932–4943, 2015.

[21] J. L. A. Quijano and G. Vecchi, "Improved-Accuracy Source Reconstruction on Arbitrary 3-D Surfaces," *IEEE Antennas Wirel. Propag. Lett.*, vol. 8, pp. 1046–1049, 2009.

[22] L. F. Canino, J. J. Ottusch, M. A. Stalzer, J. L. Visher, and S. M. Wandzura, "Numerical solution of the helmholtz equation in 2D and 3D using a high-order Nyström discretization," J. Comp. Phys., vol.146, no. 2, pp. 627–663, 1998.

[23] A. Kiaee, R. R. Alavi, M. M. Honari, R. Mirzavand, and P. Mousavi, "Ground de-embedded source reconstruction using a planar array of H-field probes," *IEEE International Symposium on Antennas and Propagation* 2017, pp. 133–134.

[24] M. A. Qureshi, C. H. Schmidt, and T. F. Eibert "Near-field error analysis and efficient sampling technique for the fast irregular antenna field transformation algorithm," *Progress In Electromagnetics Research B*, vol. 48, pp.197-220, 2013.

[25] T.F. Eibert, Ismatullah , E. Kaliyaperumal and C. H. Smith," Inverse equivalent surface current method with hierarchical higher order basis functions, full probe correction and multilevel fast multipole acceleration," *Progress In Electromagnetics Research, PIER.*, vol. 106, pp. 377-394, 2010.

[26] P. Hansen, "Rank-Deficient and Discrete Ill-Posed Problems", online.

[27] J. A. Fordham, "An Introduction to Antenna Test Ranges, Measurements and Instrumentation," Antenna System and Technology, Vol. 2, 1999.

[28] H. J. Weaver, Applications of Discrete and Continuous Fourier Analysis. New York: Wiley, 1983.

[29] R. L. Lewis and A. C. Newell, " An efficient and accurate method for calculating and representing power density in the near-zone of microwave antennas," NBS Rep. NBSIR85-3036, Dec. 1985.

[30] A. Yaghjian, "An overview of near-field antenna measurements," *IEEE Trans. Antennas Propag.*, vol. 34, no. 1, pp. 30–45, 1986.

[31] X. Li and Z. Du, "Near-Field Interference Estimation Between Multilayer PCBs Using a Reciprocity-Based Filamentary-Element Coupling Model," *IEEE Trans. Electromagn. Compat.*, vol. 60, no. 3, pp. 685–695, 2018.

[32] Q. Chen, S. Kato, and K. Sawaya, "Estimation of Current Distribution on Multilayer Printed Circuit Board by Near-Field Measurement," *IEEE Trans. Electromagn. Compat.*, vol. 50, no. 2, pp. 399–405, 2008.

[33] R. Hou, M. Lorenzini, M. Spirito, T. Roedle, F. van Rijs, and L. C. N. de Vreede, "Nonintrusive Near-Field Characterization of Spatially Distributed Effects in Large-Periphery High-Power GaN HEMTs," *IEEE Trans. Microw. Theory Tech.*, vol. 64, no. 11, pp. 4048–4062, 2016.

[34] A. Jam and K. Sarabandi, "A Submillimeter-Wave Near-Field Measurement Setup for On-Wafer Pattern and Gain Characterization of Antennas and Arrays," *IEEE Trans. Instrum. Meas.*, vol. 66, no. 4, pp. 802–811, 2017.

[35] P. Kowsalya, K. Kavinaya, and B. Krithika "Printed circuit board fault detection ," *International Journal of Advance Engineering and Research.*, vol. 5, no. 4, pp. 5–10, April. 2018.

[36] R. Runyon, "Changing the Paradigm For Optical and X-Ray Inspection of Backplanes and Large PCB Assemblies ," *IPC APEX EXPO Conference Proceedings.*, 2013.

[37] R. R. Alavi, A. Kiaee, R. Mirzavand, and P. Mousavi, "Extraction of via defects from very-near-field measurement and a source reconstruction method," 2nd URSI AT-RASC, Gran Canaria, 28 May-1 Jun. 2018.

[38] L. Gattoufi, D. Picard, A. Rekiouak, and J. C. Bolomey, "Matrix method for near-field diagnostic techniques of phased arrays," in Proceedings of International Symposium on Phased Array Systems and Technology, 1996, pp. 52–57.

[39] M. Johansson, H. Lui, J. Bolomey, and M. Persson "Source modeling using phaseless low-frequency near-field measurements," *IEEE Trans. Electromagn. Compat.*, vol. 54, no. 3, pp. 613–624, Jun. 2012.

[40] J.Ch.Bolomey "Review of Phaseless Near-Fild Techniques,"Proc. Int. Conf. Elelectromag. Near-Field Characterization and Imaging Conference (ICONIC 2009), Taipei, Taiwan, June 2009.

[41] W. Zhao, B. Wang, E. Liu, H. Byeong Park, H. Ho Park, E. Song, and E. Li, "An effective and efficient approach for radiated emission prediction based on amplitude-only near-field measurements," *IEEE Trans. Electromagn. Compat.*, vol. 54, no. 5, pp. 1186–1189, Oct. 2012.

[42] V. Semiconductors, "Vishay semiconductors 1 form a solid-state relay (normally open)," pp. 1–10, 2018.

[43] http://www.standa.lt/products.

[44] J. Zhang, and J. Fan, "Source reconstruction for IC radiated emissions based on magnitude-only near-field scanning ," *IEEE Trans. Electromagn. Compat.*, vol. 59, no. 2, pp. 557–566, April. 2017.

[45] Y. Shu, X. Wei, R. Yang, and E. Liu, "An iterative approach for EMI source reconstruction based on phaseless and single-plane near-field scanning," *IEEE Trans. Electromagn. Compat.*, vol. 60, no. 4, pp. 937–944, Aug. 2018.

[46] X. Tong, "Simplified equivalent modeling of electromagnetic emissions from printed circuit boards,"PhD. Dissertation, Univ, Nottingham, U.K., May 2010.

[47] H. Akima, "A New Method of Interpolation and Smooth Curve Fitting based on Local Procedures", based on Local Procedures,"Journal of the ACM (JACM), 17(4):589-602, , 17(4):589-602, Oct. 1970.

[48] R. R. Alavi, Ali Kiaee, R. Rashid Mirzavand, and P. Mousavi , "RWG MoM-via-locally corrected Nyström method in near-field to far-field transformation using very-near-field measurement, " *IET Microwaves, Antennas & Propagation.*, vol. 12, no. 2, pp. 145–153, Sep. 2017.

[49] A. Kiaee, R. R. Alavi, M. M. Honari, R. Mirzavand, and P. Mousavi, "Ground de-embedded source reconstruction using a planar array of H-field probes," *IEEE International Symposium on Antennas and Propagation* 2017, pp. 133–134.

[50] R. R. Alavi, Ali Kiaee, R. Rashid Mirzavand, R. Patton, and P. Mousavi , "A High-Resolution Approach to Extract the the Emissions from a Circuit Board Using the Magnitude-Only Near-Field Measurement, " *2018 IEEE International Symposium on Antennas and Propagation.*, pp. 1387-1388, 2018.

[51] R. R. Alavi, Ali Kiaee, R. Rashid Mirzavand, and P. Mousavi , "Linear-linear basis functions for source reconstruction using magnetic-field integral equations in very-near-field measurements, " *2017 IEEE International Symposium on Antennas and Propagation.*, pp. 1559-1560, 2017.

[52] R. R. Alavi, Ali Kiaee, R. Rashid Mirzavand, and P. Mousavi , "Locally corrected Nyström technique and its relationship with RWG method of moment for current reconstruction using very-near-field measurements, " *2017 11th European Conference on Antennas and Propagation (EUCAP).*, pp. 319-323, 2017.

[53] D. Deschrijver, F. Vanhee, D. Pissoort, and T. Dhaene, , "Automated Near-Field Scanning Algorithm for the EMC Analysis of Electronic Devices, " *IEEE Trans. Electromagn. Compat.*, vol. 54, no. 3, pp. 502–510, 2012.

[54] D. Deschrijver, K. Crombecq, H. M. Nguyen, and T. Dhaene, "Adaptive Sampling Algorithm for Macromodeling of Parameterized S-Parameter Responses," *IEEE Trans. Microw. Theory Techn.*, vol. 59, no. 1, pp. 39–45, Nov. 2011.

[55] G. Li, K. Itou, Y. Katou, N. Mukai, D. Pommerenke, and J. Fan, "A resonant E-field for RFI measurements," *IEEE Trans. Electromagn. Compat.*, vol. 56, no. 6, pp. 1719–1722, Dec. 2014.

[56] K. Jomaa, N. Sivaraman, F.Ndagijimana, H. Ayad, M. Fadlallah, and J.Jomaah, "Development of a 3D scanning system for magnetic near-field characterization," 2017 IEEE International symposium on electromagnetic compatibility and signal/power integrity (EMCSI). 1719–1722, Dec. 2014.

[57] G. Li, D. Pommerenke, and J. Min, "A low frequency electric field probe for near-field measurement in EMC applications," 2017 IEEE International symposium on electromagnetic compatibility and signal/power integrity (EMCSI).

[58] A. Kiaee, R. R. Alavi, R. Mirzavand, and P. Mousavi, "Numerical and experimental assessment of source reconstruction for very near-field measurements with an array of H-field probes," *IEEE Trans. Antennas Propag.*, vol. 12, no. 2, pp. 145–153, 2018.

[59] R. Carter, "The Method of Moments in Electromagnetics, by W.C. Gibson," *Contemp. Phys.*, vol. 51, no. 2, pp. 183–184, 2010.

[60] O. Ergul and L. Gure, "The Multilevel Fast Multipole Algorithm (MLFMA) for Solving Large-Scale Computational Electromagnetics Problems," *Piscataway, NJ, USA: IEEE Press*, 2014.

[61] R. D. Graglia, "On the numerical integration of the linear shape functions times the 3-D Green's function or its gradient on a plane triangle," *IEEE Trans. Antennas Propag.*, vol. 41, no. 10, pp. 1445–1455, Oct. 1993.

[62] L. Gurel and O. Ergul, "Singularity of the magnetic-field integral equation and its extraction," *IEEE Antennas Wireless Propag. Lett.*, vol. 4, no. 1, pp. 229–232, Aug. 2005.

[63] P. Yla-Oijala and M. Taskinen, "Calculation of CFIE impedance matrix elements with RWG and n $\times$ RWG functions," *IEEE Trans. Antennas Propag.*, vol. 51, no. 8, pp. 1837–1846, Aug. 2003.

[64] http://gmsh.info/

[65] Constantine A. Balanis, "Antenna theory analysis and design," Wiley, 2005.

[66] J. Zhang, K. W. Kam, J. Min, V. V. Khilkevich, D. Pommerenke, and J. Fan, "An efficient method of probe calibration in phase-resolved near-field scanning for EMI application" *IEEE Trans. Instrum. Meas.*, vol. 62, no. 3, pp. 648-658, March. 2013.

[67] E. Achtert, H.-P. Kriegel, E. Schubert, and A. Zimek, "Interactive data mining with 3D-parallel-coordinate-trees," *Proc. 2013 Int. Conf. Manag. data - SIGMOD '13*, vol. 1, no. 1, pp. 1009, 2013.

[68] Fawcett, Tom, "An Intorduction to ROC Analysis," *Pattern Recognition Journal.*, pp. 861-874, 2006.

[69] F. D'agostino, F. Ferrara, C. Gennarelli, R. Guerriero, and G. Riccio, "An Effective Technique for Reducing the Truncation Error in the Near-Field-Far-Field Transformation With Plane-Polar Scanning," *Prog. Electromagn. Res. PIER*, vol. 73, pp. 213–238, 2007.

[70] F. D'Agostino, F. Ferrara, C. Gennarelli, R. Guerriero, and M. Migliozzi, "Nonredundant NF-FF transformation with bi-polar scanning: Experimental testing," *AMTA 2016 Proceedings*, 2016, pp. 1–6.

[71] M. A. Qureshi, C. H. Schmidt, and T. F. Eibert, "Adaptive rectangular spiral acquisition technique for planar near-field antenna measurements," in 2013 7th European Conference on Antennas and Propagation (EuCAP), 2013, pp. 2926–2929.

[72] M. A. Qureshi, C. H. Schmidt, and T. F. Eibert, "Adaptive Sampling in Spherical and Cylindrical Near-Field Antenna Measurements," *IEEE Antennas Propag. Mag.*, vol. 55, no. 1, pp. 243–249, 2013.

[73] D. Janse Van Rensburg,"Adaptive Acquisition Techniques for Planar Near-Field Antenna Measurements-Part2," CA, USA, 2012.

[74] T. Dorné et al., "Optimized sequential sampling algorithm for EMI near-field scanning," *International Symposium on Electromagnetic Compatibility*, 2013, pp. 385–388.

[75] H. Ledoux and C. Gold, "Spatial Interpolation: From Two to Three Dimensions."

[76] H. Ledoux and C. M. Gold, "Modelling Three-dimensional Geoscientific Fields with the Voronoi Diagram and Its Dual," *Int. J. Geogr. Inf. Sci.*, vol. 22, no. 5, pp. 547–574, Jan. 2008.

[77] H. Ledoux and C. Gold, "An Efficient Natural Neighbour Interpolation Algorithm for Geoscientific Modelling," Dev.Spat. Data Handl., no. May, pp. 97–108, 2014.

[78] S. Grop and E. Rubiola, "Flicker noise of microwave power detectors," *IEEE International Frequency Control Symposium Joint with the 22nd European Frequency and Time forum*, 2009, pp. 40–43.

[79] E. A. Nichols, H. F. Morrison, and J. Clarke, "Signals and Noise in Measurements of Low-Frequency Geomagnetic Fields," *J. Geophys. Res. Solid Earth*, vol. 93, no. B11, pp. 13743–13754, 2008.

[80] Y. Zhou and M. Y. Chia, "A Low-Power Ultra-Wideband CMOS True RMS Power Detector," *IEEE Trans. Microw. Theory Tech.*, vol. 56, no. 5, pp. 1052–1058, 2008.

[81] R. Li, B. Pan, J. Laskar, and M. M. Tentzeris, "A Novel Low-Profile Broadband Dual-Frequency Planar Antenna for Wireless Handsets," *IEEE Trans. Antennas Propag.*, vol. 56, no. 4, pp. 1155–1162, 2008.

[82] S. Nichols, "Advanced Antenna Measurement System Architectures," *AMTA 33th Annual Meeting and Symposium*, 2011.

[83] P. F. Wacker, "Non-planar near-field measurements: Spherical scanning,"Boulder, CO, USA, NBSIR 75-809, 1975.

[84] F. H. Larsen, "Probe correction of spherical near-field measurements,"*Electron. Lett.*, vol. 13, pp. 393–395, Jul. 1977

[85] A. D. Yaghjian and R. C. Wittmann, "The receiving antenna as a linear differential operator: Application to spherical near-field measurements," *IEEE Trans. Antennas Propag.*, vol. AP-33, no. 11, pp. 1175–1185, Nov. 1985.

[86] J. Hald, J. E. Hansen, F. Jensen, and F. H. Larsen, "Spherical Near-Field Antenna Measurements," ser. IET Electromagnetic Waves, J. E. Hansen, Ed. London, U.K.: Peregrinus, 1998.

[87] O. M. Bucci, C. Gennarelli, G. Riccio, and C. Savarese, "Data reduction in the NF-FF transformation technique with spherical scanning," *J. Electron. Waves Appl.*, vol. 15, pp. 755–775, 2001.

[88] T. B. Hansen, "Higher-order probes in spherical near-field scanning," *IEEE Trans. Antennas Propag.*, vol. 59, no. 11, pp. 4049–4059, Nov. 2011.

[89] F. D'Agostino, F. Ferrara, C. Gennarelli, R. Guerriero, and M. Migliozzi, "Effective antenna modellings for NF-FF transformations with spherical scanning using the minimum number of data," *Int. J. Antennas Propag.*, vol. 2011, p. 936781, 2011.

[90] F. D'Agostino, F. Ferrara, C. Gennarelli, R. Guerriero, M. Migliozzi, and G. Riccio, "A nonredundant near-field to far-field transformation with spherical spiral scanning for nonspherical antennas," *Open Elect. Electron. Eng. J.*, vol. 3, pp. 4–11, 2009.

[91] C. Hu, L. Guo, and P. Guo, "Amplitude and phase errors analysis on spherical multi-probe antenna near-field measurement," in 2017 *IEEE Conference on Antenna Measurements and Applications (CAMA)*, 2017, pp. 12–14.

[92] B. Purnima and K. Arvind, "EBK-Means: A Clustering Technique based on Elbow Method and K-Means in WSN," *Int. J. Comput. Appl.*, vol. 105, no. 9, pp. 17–24, 2014.

[93] H. Saghlatoon, M. Honari, M. Mirzavand, and P. Mousavi, "Substrate integrated waveguide groove sensor antenna for permittivity measurements," in 2018 *12th European Conference on Antennas and Propagation (EuCAP)*, 2018, pp. 1–3.

[94] M. Honari, H. Saghlatoon, M. Mirzavand, and P. Mousavi, "An RFID Sensor for Early Expiry Detection of Packaged Foods," in 2018 *8th International Symposium on Antenna Technology and Applied Electromagnetics (ANTEM)*, 2018, pp. 1–2.

[95] H. Saghlatoon, , M. Mirzavand, M. Honari, and P. Mousavi, "Sensor Antenna Transmitter System for Material Detection in Wireless-Sensor-Node Applications," *IEEE Sensors Journal.*, vol. 18, no. 21, pp. 8812-8819, 2018.

[96] H. Saghlatoon, , M. Mirzavand, M. Honari, and P. Mousavi, "Investigation on Passive Booster for Improving Magnetic Coupling of Metal Mounted Proximity Range HF RFIDs," *IEEE Sensors Journal.*, vol. 65, no. 9, pp. 3401-3408, 2017.

[97] M. Honari, M. Mirzavand, H. Saghlatoon, and P. Mousavi, "A New Aperture Antenna Using Substrate Integrated Waveguide Corrugated Structures for 5G Applications," *EEE Antennas and Wireless Propagation Letters.*, vol. 16, pp. 254-257, 2017.

[98] M. Honari, M. Mirzavand, H. Saghlatoon, and P. Mousavi, "A Dual-Band Low-Profile Aperture Antenna With Substrate-Integrated Waveguide Grooves," *IEEE Transactions on Antennas and Propagation.*, vol. 64, no. 4, pp. 1561-1566, 2016.

[99] M. Honari, M. Mirzavand, and P. Mousavi, "A High-Gain Planar Surface Plasmon Wave Antenna Based on Substrate Integrated Waveguide Technology With Size Reduction," *IEEE Transactions on Antennas and Propagation.*, vol. 66, no. 5, pp. 2605-2609, 2018.